Title
High Contrast Grating VCSELs: Properties and Implementation on InP-based VCSELs

Author
Chase, Christopher

Publication Date
2011

Peer reviewed|Thesis/dissertation

High Contrast Grating VCSELs:
Properties and Implementation on InP-based VCSELs

by

Christopher Civilian Louis Chase II

A dissertation submitted in partial satisfaction of the

requirements for the degree of

Doctor of Philosophy

in

Engineering – Electrical Engineering and Computer Sciences

and the Designated Emphasis

in

Nanoscale Science & Engineering

in the

Graduate Division

of the

University of California, Berkeley

Committee in charge:

Professor Constance J. Chang-Hasnain, Chair
Professor Ming C. Wu
Professor Xiang Zhang

Spring 2011

High Contrast Grating VCSELs:
Properties and Implementation on InP-based VCSELs

by Christopher Civilian Louis Chase II

Abstract

High Contrast Grating VCSELs:
Properties and Implementation on InP-based VCSELs

by

Christopher Civilian Louis Chase II

Doctor of Philosophy in Engineering – Electrical Engineering and Computer Sciences and the Designated Emphasis in Nanoscale Science & Engineering

University of California, Berkeley

Professor Constance J. Chang-Hasnain, Chair

Vertical cavity surface emitting lasers (VCSELs) have become of large commercial importance over the last two decades. They have become the dominant low cost, low power coherent sources in many applications such as optical sensing and short distance data communication.

Despite their great success, there remain opportunities for improvement. Almost all commercially produced VCSELs are fabricated on structures based on a GaAs substrate. This restricts their wavelength range to between 650 and 1300 nm. Many potential applications exist at wavelengths outside of this range, so much work has gone into realizing VCSELs on other substrates. Though they have been realized, this has typically come with complexity that increases cost of producing such VCSELs. Of particular interest are InP-based VCSELs, which allow for emission at the wavelengths of 1320 nm and 1550 nm, two regions of high importance for optical communications applications.

Another area of much research has been improving the modal characteristics of VCSELs. Typical VCSELs will lase in two polarization-degenerate optical modes. In addition, due to their structure, lateral optical modes also appear when a typical VCSEL's aperture becomes more than a few microns in size, limiting their output power. For high performance optical communications and sensing, a single mode laser is essential, so solving these mode problems is important.

Next generation optical communication systems also require sources with an array of lasers of multiple output wavelengths or a tunable wavelength source that can be quickly tuned over a wide range of wavelengths. Schemes for both approaches have been implemented on VCSELs though various limitations of the current approaches have prevented them of being of large commercial importance to date. Tunable VCSELs have been limited in wavelength tuning speed by the thickness of their movable mirror. A commercially viable approach for an array of VCSELs of multiple wavelengths has also been difficult to achieve – most approaches shown to

date require complex growth methods and the have not been able to achieve controllable wavelength spacing.

High contrast gratings (HCGs) have emerged as an exciting new tool for achieving optical features such as broadband mirrors, planar lenses, and high quality factor resonators. Of particular use for VCSELs is a broadband mirror. These high contrast gratings in addition to acting as a mirror have features that can be exploited for many applications such as polarization differentiation and definable phase among others. HCGs are an exciting new tool for many optical applications.

In this dissertation, we show how a high contrast grating can potentially solve several of the issues facing VCSELs and open new application spaces for VCSELs. First, we introduce the state of the art in VCSEL research and give a detailed overview of major areas of interest in VCSEL research. Next, we introduce high contrast gratings, discuss their implementation onto VCSELs, and demonstrate how they can be used to achieve more ideal modal qualities in the VCSEL, a single polarization mode as well as a larger area single transverse mode device. Then we show how the high contrast grating can be used in a tunable VCSEL to achieve ultra high speed tuning. Following that discussion, we shift our focus to implementing high performance, low cost VCSELs on InP with an HCG, showing two different approaches: a deposited Si HCG sitting on SiO_2 and a monolithically-grown InP HCG. We conclude with a discussion of two approaches to achieve controllable arrays of VCSELs emitting at multiple wavelengths. The high contrast grating may be an important tool to achieving higher performance VCSELs, and VCSELs with features that enable new applications.

TABLE OF CONTENTS

LIST OF FIGURES

ACKNOWLEDGEMENT

First, I would like to thank my advisor, Professor Connie Chang-Hasnain for her mentorship and guidance the past six years. Her support has been crucial for the work in this dissertation. I am very thankful for all of the opportunities I have been presented while working in her group as well. I would also like to thank Professor Ming Wu, Professor Xiang Zhang, and Professor Al Pisano for their review of this dissertation and serving on my qualifying exam committee.

I would especially like to thank my current and former lab mates for their help and discussions. Without the support of the rest of the team in the Chang-Hasnain group, much of this work would not have been possible. Especially, I would like to thank Frank Rao, Mervin Zhao, Werner Hofmann, Vadim Karagodsky, and Mike Huang, who were a big part of the work in this dissertation.

I would also like to thank Professor Markus Amann and his students, Michael Mueller and Tobias Grundl for their collaboration. Professor Ming Wu and his students have also provided me much help and discussion as well. Finally, I would like to thank the Berkeley Microlab staff for their help and support in fabricating the devices in this work.

I am also thankful for the funding support from various sources through the course of my dissertation research, especially the NSF Graduate Research Fellowship and IGERT Fellowship. Funding support for much of the InP-based VCSEL work was provided by the CIAN NSF ERC under grant #EEC-0812072.

Finally, I would like to thank Susan, my parents, and rest of my family for their love, encouragement, and support through the course of my studies.

Chapter 1 VCSELs: State of the Art and Challenges

1.1 Historical Evolution of the VCSEL

Vertical-cavity surface-emitting lasers (VCSELs) were first proposed over 30 years ago by Iga and colleagues at the Tokyo Institute of Technology [1] and have been a topic of a large amount of research since. Compared to edge emitting semiconductor lasers, they have some obvious advantages. Since they emit vertically, they can be fabricated in denser arrays and tested on chip before any packaging costs are incurred, thus they can be fabricated at a much lower cost. Additionally, they can be simply made into devices with a single longitudinal and transverse optical mode, which has a symmetric mode profile. For many applications of lasers such as sensing and optical communications of over a few hundred meters, a single output mode is critical. Edge emitting semiconductor lasers typically require a fabricated grating for distributed feedback [2] or some external element to achieve a single mode device, adding complexity and cost to fabrication. VCSELs are also superior in terms of energy efficiency as they have lower laser threshold currents than edge emitters.

Additionally for optical fiber communications applications, a circular mode profile of the laser output is desirable for high efficiency coupling from the laser into the fiber. The output profile of edge emitting lasers is elliptical, requiring optical elements in line with the laser to correct the mode shape, again making fabrication and packaging more complex than for a VCSEL, which has a circular mode pattern if properly designed.

Despite these advantages, some time passed between when VCSELS were first proposed and when they reached commercial success. The first VCSELs were demonstrated at 77 K under pulsed excitation soon after they were proposed [3]. It was not until 10 years later though that the first room temperature continuous wave devices were demonstrated [4]. A further major advance in VCSEL performance occurred in 1994 with the demonstration of the aluminum oxide aperture in GaAs-based VCSELs [5], which resulted in drastic drops in VCSEL drive voltages and threshold currents and significantly higher wall plug efficiencies [6]. From that point,

commercial production of GaAs-based VCSELs took off, with 850 nm VCSELs becoming the dominant source in short reach optical communications applications and in optical sensing applications such as in laser computer mice. Modern commercial VCSEL production has reached extremely low costs with high yield and reliability [7-9].

Over the last decade, research has continued on VCSELs. Five areas of a large amount of continuing research are wavelength tunable VCSELs, VCSEL structures on substrates other than GaAs, particularly InP-based VCSELs, polarization and modal stability, VCSEL arrays, and high modulation speed.

1.2 Typical VCSEL Structure

A schematic of a basic VCSEL structure is shown in Figure 1.1. Typical VCSELs consist of from the substrate side, a bottom mirror, an active cavity with an optical thickness of 1 to several lambdas of length with a multiple quantum well region in the middle, a layer for forming a current aperture, and a top mirror. Typically VCSELs emit from the top of the wafer, so a ring contact is formed around the edge of the emission region and a current aperture is used within the structure to force the current through the active region in an area not covered by metal on the top side. The current aperture can be formed through several different techniques including proton implantation [10], lateral oxidation [5], or a buried tunnel junction [11]. The top and bottom mirrors are typically made of epitaxially grown distributed Bragg gratings or dielectric deposited dielectric DBRs.

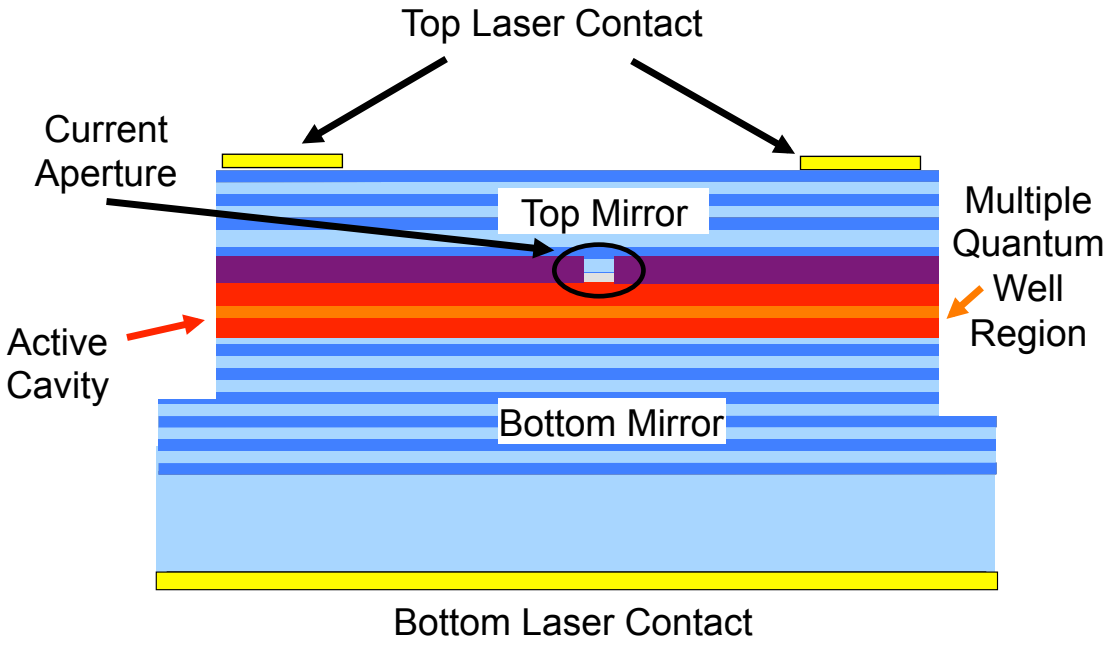

Figure 1.1 Basic VCSEL schematic. The active region is between two mirrors with some type of current aperture to funnel current through the middle of the structure. Emission is through the top of the structure.

1.3 Non-GaAs-based VCSELs

GaAs-based VCSELs were the first VCSELs to be developed because of the relative maturity of materials growth on GaAs. Active regions suitable for VCSELs can be grown on GaAs from ~640 nm [12] up to ~1280 nm [13], [14]. Recently, some success has even been achieved in pushing the active region out to 1.53 μm [15] using GaInNAsSb [16] in the laboratory. Achieving high performance VCSELs on other substrates is still a topic of much study. In particular, the challenges of creating many pairs of DBRs and good optical/electrical confinement are challenging on other material systems and have been a topic of very active research during the past decade.

1.3.1 InP-based VCSELs

The system of most interest has been InP, which is also a well-developed material system due to the ability to achieve high quality 1.3 μm and 1.55 μm active regions on it [17]. These wavelengths are of enormous interest for telecommunications applications as they have much lower loss in optical fiber than the near-IR region where GaAs VCSELs typically operate. Despite the large potential market for VCSELs on InP, room temperature continuous wave operation on the substrate was only achieved around the year 2000 [18], [19]. That said, comparable performance of InP-based VCSELs to GaAs-based VCSELs in terms of power output, threshold, and modulation speed has been achieved in the last few years [20-22].

The two main challenges in implementing VCSELs on InP are forming a current aperture and finding suitable high reflectivity mirrors. The InP system is challenging to form a current aperture in because there is no easy-to-oxidize material in the system, unlike GaAs in which an aluminum oxide current aperture can be easily formed [5]. Most commonly, this problem has been overcome by forming a buried tunnel junction in the VCSEL structure [18], which provides a high degree of electrical confinement and also allows optically lossy *p*-layers in the structure to be replaced with *n*-layers. Other approaches to solving the problem of a current aperture on InP include using an aluminum oxide aperture formed after pseudomorphic growth of GaAs-based materials above the active region [23], by etching away layers in the middle of the VCSEL structure [24], or by selectively bonding two structures together only in the area of the aperture [25]. These aperture approaches are technologically challenging and add complexity and expense to the mass manufacture of long wavelength VCSELs.

In addition to the challenge of forming a current aperture, the *p*-side mirror on the VCSEL also poses problems. InP is a poor material upon which to grow a *p*-doped DBR since free carrier absorption is very significant at telecommunications (1.3~1.6 um) wavelengths, making the top mirror extremely lossy if formed of *p*-material. The index contrast available in the GaAlInAs/InGaAsP/InP material system is substantially smaller than other VCSEL material systems. This small index contrast means greater than 40 pairs of epitaxial DBR are required on both bottom and top of the VCSEL structure, an extremely challenging technological proposition from the standpoint of epitaxial growth.

This makes incorporating *p*-doped epitaxial DBRs with their large electrical and optical losses extremely difficult to realize. Furthermore, DBRs made with ternary and quaternary alloys have an order of magnitude worse thermal conductivity than the GaAs-Al(Ga)As DBR stacks for the short-wavelength devices. With all of these difficulties, performance is poor in VCSELs realized with a *p*-doped DBR.

This necessitates an alternative approach to the *p*-side mirror of the VCSEL structure. Typically a short current spreading *p*-region followed by a tunnel junction with *n*-region and intra-cavity contacts is employed [18]. The top mirror is then formed by either evaporating a dielectric mirror [26], wafer fusing an epitaxially-grown DBR grown on another material system [27], using an Sb-based DBR [24], or a metamorphically grown GaAs/AlGaAs top DBR [23]. These options are technologically challenging from a growth and fabrication standpoint and relatively costly compared to using a monolithic structure already including a *p*-GaAs/AlGaAs DBR as is typically used in a short wavelength VCSEL

Very recently, an approach using a high contrast grating and an ion implant current aperture has been demonstrated [28], which has the potential to be fabricated with a nearly as simple and low cost process as on GaAs. Further discussion of this VCSEL structure is provided in Chapter 5.

1.3.2 Other Substrates

Other substrates have also seen development. In the blue to ultraviolet (UV) range, GaN-based VCSELs have been a topic of study as of late with continuous wave performance being shown at 462 nm [29] and optically pumped CW performance at 343 nm [30]. In addition, in the UV range, the first VCSEL on ZnO has recently been demonstrated at 385 nm [31] under optical pumping.

On the long wavelength side, there is also much interest in VCSELs, as there are many potential gas-sensing applications requiring low cost laser sources. InP VCSELs have been demonstrated at as long as 2.3 μm [32]. Beyond that wavelength, GaSb-based VCSELs are the leading candidate. These devices have been demonstrated under room temperature continuous wave operation at 2.3 μm [33] and more recently at 2.6 μm [34], [35].

1.4 Tunable VCSELs

Wavelength tunable vertical-cavity surface-emitting lasers (VCSELs) were first proposed and implemented in the mid-1990s [36], [37]. They have generated a large amount of interest because of a wide variety of potential applications in areas such as telecommunications [38] and spectroscopy [39]. The low cost nature of a VCSEL makes them desirable over other higher cost approaches to tunable lasers such as sampled gratings [40] or external cavities [41] in many applications. Control of tunable VCSELs is also straight forward requiring a single additional contact to control the tuning in comparison to other approaches such as sampled gratings that require 2 contacts and control signals to achieve their full range. Additionally, tunable VCSELs use low power MEMS approaches for tuning, drawing a few nanowatts of power compared to sampled gratings, which use plasma effects to achieve tuning, requiring tens of milliwatts of current.

Tunable VCSELs were initially implemented on GaAs substrates at 980 nm [36], [37] and since have been implemented at many other wavelengths of interest such as 850 nm [42], 1550 nm [23], and 760 nm [43]. All of these approaches utilized a similar approach to tuning – a VCSEL with a bottom DBR, active region, followed by an air gap and a suspended DBR. Tuning is achieved by actuating the suspended DBR towards the cavity, reducing the size of the air gap and therefore total cavity length, shifting the emission wavelength. The tuning of the mirror can be achieved by several different actuation methods including electrostatic [36], thermal [44], and piezoelectric [45].

1.4.1 Tuning Range

From an applications perspective, the two main metrics of interest for tunable VCSELs are tuning range and tuning speed. The required tuning range depends on the application. For spectroscopy applications, often the laser needs to tune only across a single gas line, so less than a nm is required. If multiple gas lines are to be detected though, the laser needs to be able to cover the full range of wavelengths between the lines. For telecommunications applications, a full band is desirable (C band, 32 nm at 1550 for example). Even more preferable would be two bands (~60 nm).

The tuning range of tunable VCSELs can be limited by several different factors. First, the reflectivity bandwidth of the top and bottom mirrors must be wide enough to cover the entire desired tuning range. Epitaxial DBR mirrors especially can limit the tuning range as their bandwidth may only be a few 10s of nm, thus in recent years there has been a push to integrate dielectric DBRs [44] into tunable VCSELs, which can have 100 nm bandwidths. A second consideration is that the MEMS needs to be designed such that the mirror can physically move far enough to cover the entire desired wavelength range. Another important factor is the overlap of the cavity's electric field peak with the gain. If the cavity is not carefully designed, the electric field peak drifts off the gain region, resulting in the overlap factor of the electric field with the active region falling off, eventually requiring more gain than the active region can provide at the edges of the tuning range. The final factor is the bandwidth of the gain, which ultimately limits the wavelength range over which a device can lase.

Since the first tunable VCSELs were introduced, considerable progress has been made in optimizing tuning range. Figure 1.2 shows the evolution of VCSEL tuning range as a function of time. Blue dots indicate GaAs-based VCSELs, while red dots indicate InP-based structures. The first tunable VCSELs had tuning ranges on the order of 20 nm [36], [37]. Further optimization pushed the tuning range up to 30-40 nm within a few years [42], [46]. Later, using techniques such as an integrated anti-reflection coating between the air gap and bottom VCSEL structure, tuning ranges of over 60 nm have been achieved [47]. The largest reported tuning range is now 76 nm [48].

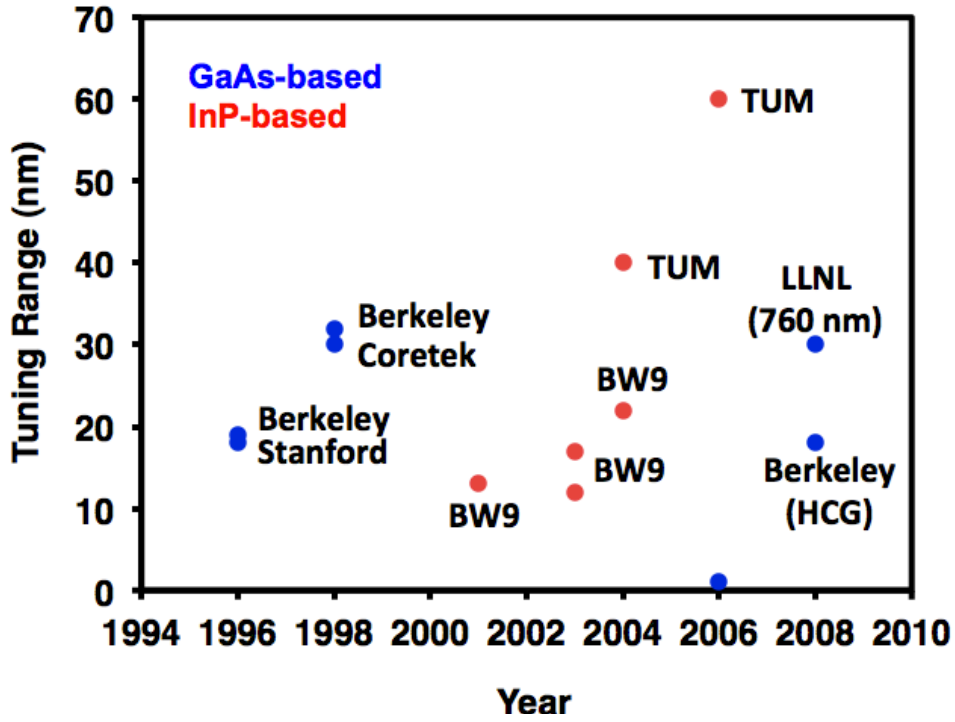

Figure 1.2 VCSEL tuning range as a function of time. Blue dots indicate GaAs-based VCSELs and red dots InP-based VCSELs.

1.4.2 Tuning Speed

Tuning speed is the other major performance consideration for tunable VCSELs. For many of the applications for tunable VCSELs, it is desirable to decease wavelength-tuning time as much as possible. In particular, next generation optical communications systems desire wavelength tunable sources with tuning speeds much less than one microsecond. High cost tunable lasers such as sampled grating lasers have been able to achieve this speed [49] for some time because their tuning is due to electrically induced effects instead of mechanically induced effects.

Initial tunable VCSELs showed tuning speeds on the order of one millisecond [38]. After mechanical optimization, tuning speeds on the order of 10 μs were achieved [50]. Given a required tuning range and maximum system voltage, MEMS-tunable VCSELs are limited in their tuning speed by the thickness of their movable mirror layer (For further discussion of this point see Section 3.2). If an epitaxial DBR is used, this means a mirror on the order of 3 to 10 μm.

In recent years, groups have switched to dielectric DBR mirrors as the tunable mirror, which can be thinner as they require fewer pairs to achieve the same reflectivity as an epitaxial DBR. This allows for faster tuning. The fastest speeds achieved with this approach are approximately 1 μs [43], [51]. Most recently, high contrast gratings have been integrated into tunable VCSEL structures [52]. Due to their much thinner profile of ~150 nm, tuning speeds of down to 20 ns have been reported [53]. A full discussion of HCG tunable VCSELs is presented in Chapter 3.

1.5 Multiwavelength VCSEL Arrays

Another item of research has been multiwavelength VCSEL arrays. These are of particular interest for optical communications applications where wavelength division multiplexed (WDM) sources are required. These sources have been produced for many years for the telecommunications market, with modern arrays using DFB lasers reaching extremely high performance, with precisely defined wavelength spacing and high modulation speeds [54]. As bandwidth requirements for optical communications links rise higher and higher, the need for a multiwavelength source becomes necessary in more and more applications. Unfortunately, the present DFB multiwavelength array technology is quite expensive, and may not be able to reach costs low enough for implementation in the consumer applications where WDM sources will be required in the near future.

The VCSEL can be easily used in a high-density array configuration with positions relative to each other lithographically defined at will. As they are VCSELs, they can in principle be fabricated at a much lower cost than other WDM sources. The VCSEL's potential in this application was first proposed in the early 1990s [55]. The first realized approach to an array of VCSELs emitting at multiple wavelengths used growth-induced variation of the thickness of the the VCSEL cavity [55], [56]. Later approaches used techniques such as patterned substrates [57], non-planar MOCVD growth [58], and anodic oxidation and etching [59]. None of these approaches proved to be scalable to mass fabrication and have moved beyond the research lab, so a better approach that provides precise repeatable control of wavelength spacing in an array is still an open topic of research.

Recently, two approaches to creating multiwavelength arrays using high contrast gratings have been proposed, in which the wavelength can be defined after epitaxial growth. These approaches show promise for realizing a low cost multiwavelength VCSEL array. Full discussion of this approach can be found in Chapter 6.

1.6 VCSEL Modal Characteristics

1.6.1 Polarization Stable VCSELs

For many applications, polarization stability is critical for VCSELs, especially sensing and communications applications. Different polarization modes can emit on slightly different wavelengths and have different light-current characteristics, thus a switch between polarization modes under operation can cause the wavelength or output power to suddenly jump. This sort of instability can wreak havoc when sensing the signal in an application. This makes it critical for VCSELs to emit in a single uniformly polarized mode. Typical VCSEL structures are circularly symmetric, so no strong selection mechanism exists intrinsically. This causes the polarization of the VCSEL to change randomly under operation as a function of temperature, bias current, feedback, etc. [60], [61].

Much research has been performed to solve the problem of a lack of intrinsic polarization selection in the structure. Subwavelength gratings are well known to have birefringent characteristics for light polarized parallel or perpendicular to the grating dimension. This characteristic has been the main tool utilized to induce some sort of polarization selection in a VCSEL structure.

By patterning the top layer of a DBR with a properly designed subwavelength grating, a difference in effective reflectivity can be induced, causing one polarization to see much higher loss within the structure, effectively preventing it from lasing. This concept has been demonstrated over the past few years [62-65]. The drawback to this approach though is that since the grating is on the topmost pair of the DBR, the difference in loss between the two polarization modes cannot be that large. During high-speed modulation or under a certain amount of optical feedback, this method may not provide enough difference in loss.

A second approach is to put a subwavelength grating within the cavity itself. With the right design, the cavity's Fabry-Pérot wavelength can be tens of nanometers apart between the parallel and perpendicular polarizations. If one of the polarizations is on the gain peak of the active region, the other will be far off. In this case, the large difference in gain between the two modes causes the VCSEL to be pinned to one polarization. This approach has been recently demonstrated [66]. This approach requires fabricating a grating within the cavity itself though, so from a cost and complexity standpoint is not as desirable as a surface grating.

High contrast gratings provide an enhanced polarization differentiation compared to these other subwavelength grating approaches. A full discussion of the polarization differentiation in VCSELs using high contrast gratings can be found in section 2.4.

1.6.1 Large Area Single Mode VCSELs

In VCSELs, higher order modes exist when the waveguiding inherent in the structure allows for it [67], generally above a certain current aperture size. These higher order modes are detrimental to many applications. The higher order modes lase at slightly different wavelengths than the fundamental mode, compromising the spectral purity of the laser, which is detrimental in sensing applications or mid and long distance optical communications links. Additionally, under modulation, output power is generally switching between the various modes, which is problematic for high-speed modulation in a dispersive environment.

Thus, to achieve devices for these applications, a small aperture size is typically used, precluding higher order modes. The drawback is that this also limits the maximum output power to much less than could be achieved with a larger aperture due to self-heating effects. Thus, there has been a search for ways to increase the size of the current aperture in a VCSEL, also increasing the power output, without losing the single mode optical characteristic.

One approach to maximize output power is to engineer the waveguiding of the structure by etching holes in the structure similar to a photonic crystal fiber [68], [69] to force larger apertures to be single mode. This tends to also increase resistance and threshold of the device though as well as add fabrication complexity.

An alternative approach to eliminating the higher order modes is to add some differentiation in the loss seen by the fundamental and higher order modes. This has been realized by introducing a surface relief designed so that the area of the DBR the fundamental mode physically occupies has a lower loss than the area that the higher order modes occupy [70].

A third approach to achieving a larger area single mode device would be to design a mirror such that differentiates based on the perpendicular wavevector, or equivalently differentiates based on angle of the incoming light. Higher order modes have a larger perpendicular wavevector, so a mirror with a highly angular dependent reflectivity would be desirable. DBRs unfortunately, show an extremely weak angular dependence, so they cannot be used for such an approach. This approach has been recently demonstrated using an HCG though [71], [72] as the

HCG's reflectivity can designed to be a strong function of angle. Further discussion of using an HCG for higher order mode differentiation is provided in section 2.5.

1.7 Conclusion

Since their initial proposal, VCSELs have rapidly developed. Though they have reached wide commercial success, many areas of research remain, especially in the areas of non-GaAs based VCSELs, tunable VCSELs, modal characteristics, and arrays of VCSELs emitting at multiple wavelengths. In the following chapters, we discuss high contrast gratings and their application to VCSEL, especially in solving problems in some of these areas.

Chapter 2 High Contrast Gratings

2.1 Introduction

Gratings are a fundamental optical device with a long history. James Gregory discovered gratings in the 1600s by observing the diffraction of light through a bird's feather. Since then they have become an important component of many optical systems most notably monochromators and spectrometers. Common diffraction gratings are made of strips of material surrounded by some other material of another index, spaced at greater than the wavelength of interest. Through diffraction, the light is transmitted or reflected from the device in different directions, which are dictated by the grating's design. By nature, these gratings are also dispersive, so the direction of the reflected and transmitted beams is a function of the wavelength.

Gratings can also be made subwavelength, at which different characteristics appear. At grating periods of much less than one wavelength, the material essentially appears to the light as a single material of an average index of the grating bars and material between them. This average index is not the same for electric fields polarized parallel and perpendicular to the grating bars due to the boundary conditions in Maxwell's equations. Thus, these deep subwavelength gratings are useful in applications where some polarization anisotropy is needed.

In between the regime of diffraction gratings and these deep subwavelength gratings are near subwavelength gratings, which have properties altogether different from both diffraction and deep-subwavelength gratings. In particular, high contrast gratings, which are made up of a subwavelength grating structure with a periodicity less than but near to the wavelength of interest and completely surrounded by a low index material such as air or SiO_2, can be designed to show peculiar properties such as very broadband high reflectance or narrow high quality factor resonances.

These high contrast gratings are an exciting option for a wide range of optical devices and functionalities. The key feature is that they are totally surrounded by low index material, which gives them some extraordinary properties. They were proposed first in 2004 [73], [74] and first

implemented later that same year [75]. HCGs were initially implemented in a device in the form of a top mirror for a VCSEL [76], soon followed by a tunable VCSEL [77]. Since then they have been harnessed in many other devices. They have been shown as a shallow angle broadband reflector, suitable for a low loss hollow core waveguide [78]. Also they have been shown as high quality factor resonators [79]. In a mechanical system, they can be used as highly sensitive motion detectors [80]. In-plane polymer lasers have been fabricated using two HCG mirrors [81].

Very recently, groups have begun exploring the manipulation of the reflectivity phase of the high contrast grating in addition to the reflectivity magnitude. One exciting application of this phase manipulation is the ability to make lenses and focusing reflectors with just a single thin HCG [82], [83]. Another interesting application is the use of HCGs with different phases and dimensions, but the same thickness to create a low cost multiwavelength VCSEL array [84] (For further discussion, see Chapter 6.).

Our group first demonstrated that a high contrast can totally replace the top DBR in a VCSEL in 2006 [77]. Before that, subwavelength gratings had been used on VCSELs, but only as a means to suppress one of the two orthogonal polarization modes [62], [65], [85] by providing some anisotropy in the top mirror's reflection, not as a highly reflective mirror on its own. Previous subwavelength gratings on VCSELs still included both top and bottom DBRs. An HCG on the other hand also provides intrinsic polarization control to VCSELs [86] but simultaneously acts as the high reflectivity mirror.

HCGs on VCSELs have been a subject of much research interest because of the interesting properties they provide. They are roughly an order of magnitude thinner, shrinking the mirror thickness from several microns to a few hundred nm. This reduces the complexity and costs of the epitaxial requirements of the VCSEL structure. Because of the reduction of mass in the mirror, much faster wavelength tunable VCSELs have been realized [52], [53] (For further discussion, see Chapter 3). In addition to the reduced epitaxy requirements, high contrast gratings offer advantages in terms of optical characteristics in VCSELs, especially polarization control, and transverse mode control [71], which can lead to larger power single mode devices. Electrically-pumped HCG VCSELs have been shown at wavelengths of 850 nm [77], 980 nm [87], 1.32 μm [88], and most recently 1.55 μm [28].

In this chapter we focus on the practical design of a HCG integrated on a VCSEL as well benefits HCGs offer as an alternative as a top mirror to distributed Bragg reflectors (DBRs). In particular, we focus on practical design issues such as minimum HCG size, tolerance to fabrication error, and low index spacer thickness. Polarization control and higher order mode suppression are also explored.

2.2 Physical Basis

The physics behind the high contrast grating have been explored in detail over the past several years [89-91]. The physical basis of the broadband high reflectivity of the HCG is due to destructive interference of modes within the structure. When a plane wave is incident on an HCG, it breaks into several modes within the structure, usually just two. These modes propagate through the structure at different speeds and when the grating is properly designed, at the back interface of the structure the modes add up to on average zero energy. Thus no energy is coupled into the transmitted plane wave from the structure. Since the grating is below the periodicity

required to have propagating higher order modes, the only direction the energy can travel is back out the front interface. Thus, total reflection can be achieved.

2.3 TE and TM High Contrast Gratings

There are two configurations of high contrast gratings: those with high reflectivity for light polarized perpendicular to the grating bars, transverse magnetic (TM), and those with high reflectivity for light polarized parallel to the grating bars (TE). An example design of both a TE and a TM grating designed for high reflection at 1.55 μm is shown in Figure 2.1. In these designs, the grating is sitting on SiO_2. In general, the thinnest broadband TM designs are approximately a factor of 1.5 times thicker than TE designs.

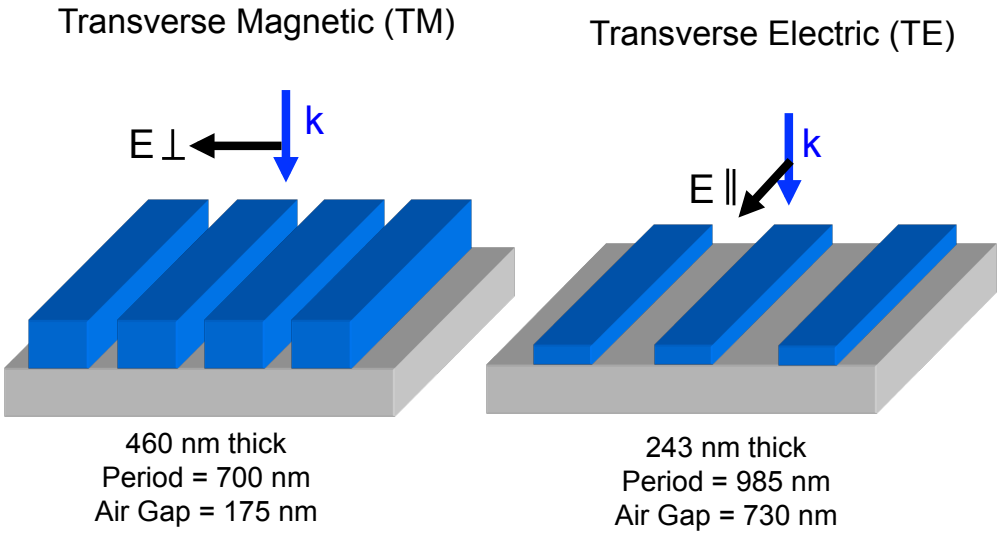

Figure 2.1 Example broadband highly reflective HCG designs at 1550 nm. Two designs are shown: (left) transverse magnetic (TM), with high reflectivity for light polarized perpendicular to the grating bars, and (right) TE, with high reflectivity for light polarized parallel to the grating bars.

The reflectivity of the highly reflective polarization for each design (reflected TE light for TE design and reflected TM light for the TM design) is shown in Figure 2.2 as a function of wavelength. The simulation was performed using rigorous coupled wave analysis (RCWA) [92]. The simulation structure consisted of an InP substrate (n=3.16), on top of which is a SiO2 layer (n = 1.47). The HCG material is Si (n = 3.48). A loss of k = 0.0005 was used in the silicon to approximate small losses due to free carrier absorption, etc. For the TM design, the period was 700 nm, the grating thickness 460 nm; the semiconductor duty cycle 75%, or equivalently, an air gap of 175 nm. The thickness of the SiO2 was 783 nm. For the TE design, the period is 985 nm; grating thickness 243 nm; semiconductor duty cycle 26%; and SiO_2 thickness 1.67 μm.

The reflectivity of the TE and TM designs is above 99% over a 100 nm bandwidth in the TE case and a 300 nm bandwidth in the TM case. Note that this bandwidth is a function of the HCG design, and the high reflectivity is not necessarily always a wider bandwidth for a TM design.

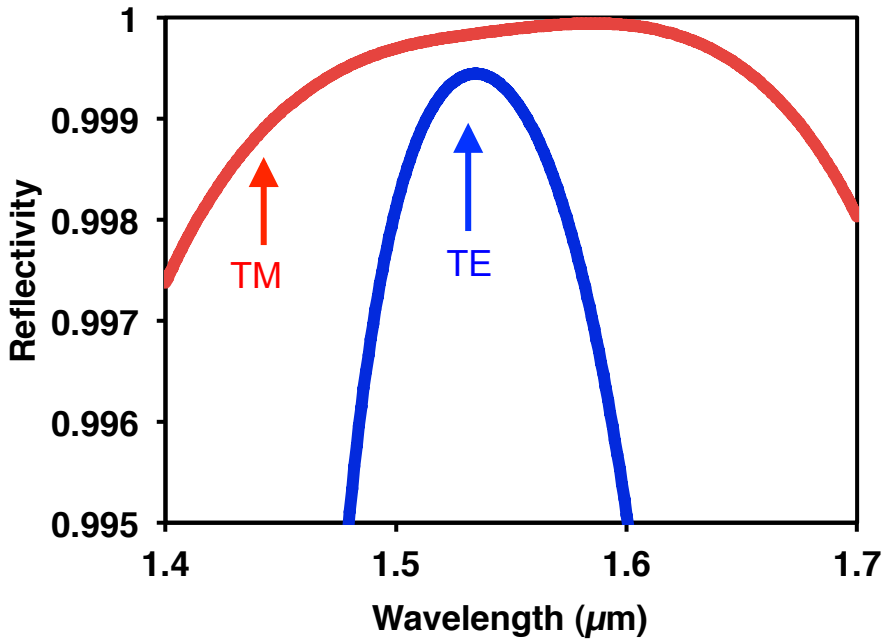

Figure 2.2 Calculated reflectivity of TE (with TE incident light) and TM (with TM incident light) designs as a function of wavelength. Both have a broadband high reflectivity band over 100 nm. Note that this bandwidth can be tweaked as a function of HCG design, and TM is not always necessarily the broader bandwidth design.

2.4 Polarization Mode Suppression

As mentioned in Chapter 1, deterministic control of polarization has been a topic of much research in VCSELs recently. High contrast gratings, being subwavelength gratings by nature, also provide polarization-dependent reflectivity, and when properly designed, pin the output polarization of the VCSEL to a lithographically determined polarization. Since the HCG provides all of the reflectivity to the structure, a high degree of difference in modal loss can be designed between the polarization perpendicular to and parallel to the grating, unlike the most common approach, shallow surface subwavelength gratings [62], [65], [85]. This comes about due to a large difference in reflectivity between TE and TM polarized light, which creates a large difference in round trip cavity loss between the two polarizations with the cavity.

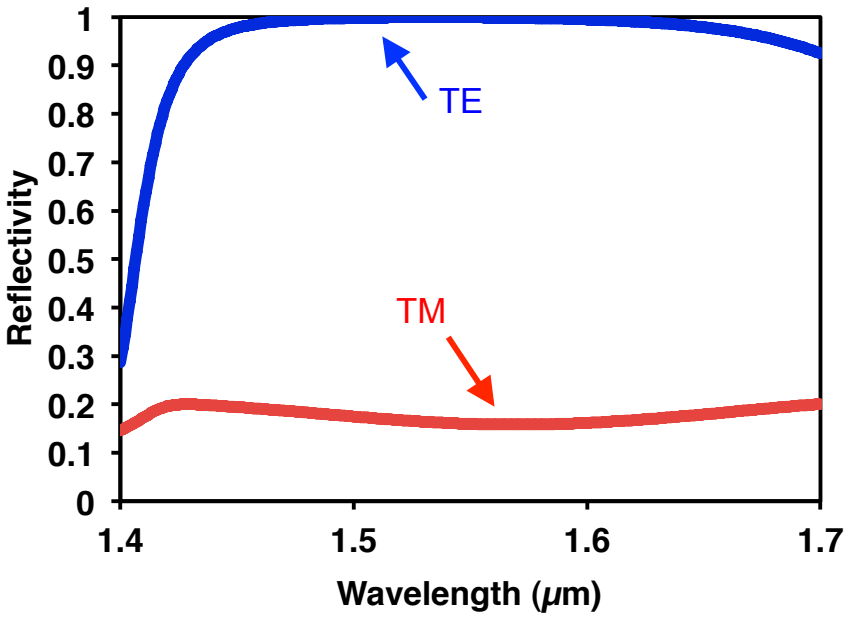

Figure 2.3 Calculated reflectivity of a TE designed HCG with TE (blue) and TM (red) incident light as a function of wavelength. While the HCG is highly reflective for TE light over a 100 nm bandwidth, it is less than 20% reflective for TM light, creating a large difference in round-trip cavity loss between the two modes.

The reflectivity of a TE HCG for both TE (light parallel to grating direction) and TM (light perpendicular to the grating direction) is shown in Figure 2.3 as calculated by RCWA. The simulation structure consisted of an InP substrate (n=3.16), on top of which was a SiO2 layer (n=1.47). The HCG material is Si (n=3.48). A loss of k=0.0005 was used in the silicon to approximate small losses due to free carrier absorption, etc. For the TE design, the period is 985 nm; grating thickness 243 nm; semiconductor duty cycle 26%; SiO_2 thickness 1.67 µm. A high differentiation between reflectivity is seen for TE and TM light. While the TE reflectivity is above 99% over >100 nm, the TM reflectivity is not greater than 20%.

Similar behavior can be seen in a TM HCG design. Figure 2.4 shows the calculated reflectivity for a TM HCG with a similar simulation setup as for the TE design in Figure 2.3. For the TM design, the period was 700 nm, the grating thickness 460 nm; the semiconductor duty cycle 75%, equivalently, an air gap of 175 nm. The thickness of the SiO2 was 783 nm. The TM design shows an even wider high reflectivity bandwidth of over 300 nm for TM-polarized light. The TE-polarized light has reflectivity as low as 5% at 1.49 µm varying up to high reflectivity around 1.65 µm. Experimentally, the HCG has been shown to pin the devices polarization well under varying operation conditions in several device structures [28], [86].

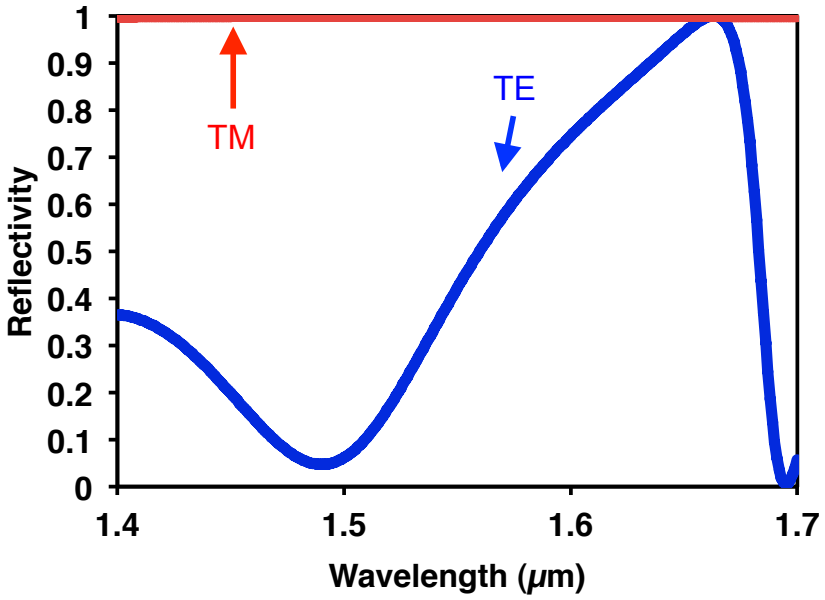

Figure 2.4 Calculated reflectivity of a TM designed HCG with TE (blue) and TM (red) incident light as a function of wavelength. While the HCG is highly reflective for TM light over a 300 nm bandwidth, it is as little as 5% reflective for TE light.

2.5 Higher Order Mode Differentiation

Another important advantage in utilizing a high contrast grating on a VCSEL is that higher order modes can be suppressed. This is advantageous for many applications and can result in higher power output from the VCSEL. Engineering the VCSEL's waveguiding properties [68], [69] or providing a difference in modal loss as a function of physical area have been explored [70].

2.5.1 Physical Basis

An alternative approach would be to design a mirror such that differentiates based on the angle of the incoming light. This approach can be exploited by an HCG though, since the HCG's reflectivity can be designed to be a strong function of angle as opposed to a DBR which is relatively angle insensitive. Figure 2.5 shows the reflectivity of both a DBR (red) and a HCG (blue) as a function of angle as measured from perpendicular to the mirror. DBRs show an extremely weak angular dependence, so they cannot be used for this type of approach. The HCG on the other hand show a much stronger dependence, with the reflectivity falling off drastically at angles greater than 5º.

The HCG used in this simulation was 145 nm thick, had a 640 nm period, and a ~400 nm air gap. This HCG was a TE-HCG, designed to be highly reflective at 850 nm for light with an electric field polarized along the direction of the bars (further details on this design, including the reflectivity spectrum for TE and TM polarizations can be found in section 3.3.2). This HCG is suspended over a 900 nm air gap, which is above 2 pairs of DBRs ($Ga_{0.88}Al_{0.12}As$ and $Ga_{0.1}Al_{0.9}As$ designed for 850 nm), which are included in the design for current spreading

purposes. The DBR used in the simulation is a standard out-coupling top DBR of 24 pairs of $Ga_{0.88}Al_{0.12}As$ and $Ga_{0.1}Al_{0.9}As$ designed for a 850 nm VCSEL.

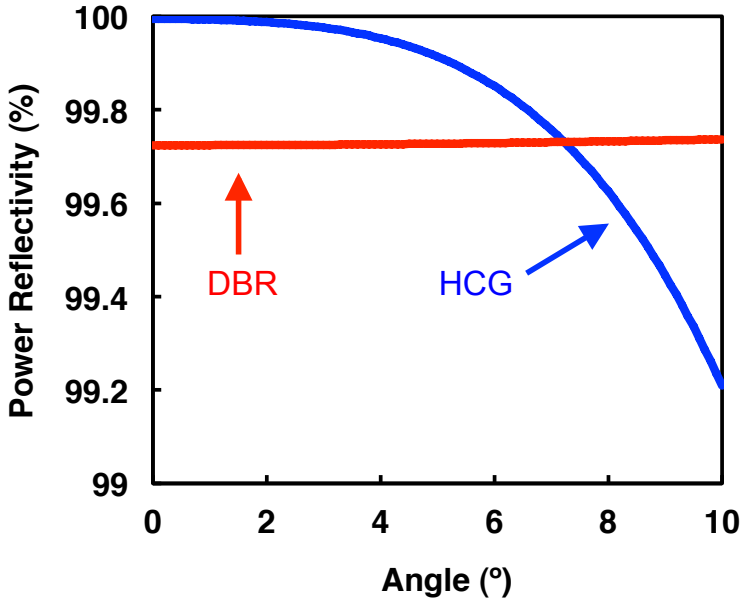

Figure 2.5 RCWA simulation of mirror reflectivity as a function of angle in air as measured from perpendicular to the mirror. The DBR (red) has a nearly constant reflectivity as a function of angle while the HCG's reflectivity (blue) starts falling off at around 5º. The HCG's highly angle dependent reflectivity contributes to its higher order mode differentiation.

2.5.2 Simulation

Figure 2.6 shows mirror loss as a function of VCSEL aperture size for both a planar DBR and a 9 period (or equivalently ~6 μm wide) TE-HCG. The results are obtained using a FDTD simulation at 850 nm. The simulation is performed by launching a beam with either the first or second order mode characteristic at the desired aperture size and measuring the energy that is returned through the aperture. The DBR and HCG designs used in this simulation are the same as in section 2.5.1. As can be seen in the simulation, there is very little differentiation in loss between the 1st (blue, solid) and 2nd (blue, dashed) order DBR modes as the DBR's reflection is fairly indifferent to reflection. At small aperture sizes (<1.5 μm) in the DBR case, an increasing loss is seen due to diffraction losses.

In the HCG's case though, things are much different. A high differentiation is seen in loss between the 1st (red, solid) and 2nd (red, dashed) order modes. While a DBR shows a reasonable differentiation between 1st and 2nd order modes only at aperture sizes less than 3 μm, the HCG sees a high differentiation at all aperture sizes, thus single mode operation can be expected up to much larger aperture sizes. The differentiation can be directly attributed to the high angular dependence of the HCG's reflectivity.

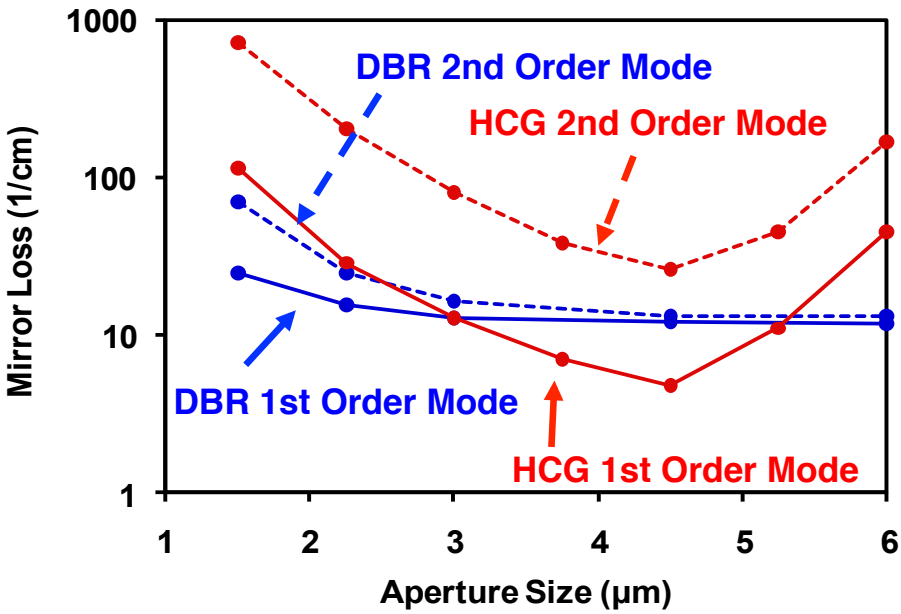

Figure 2.6 FDTD simulation of mirror loss as a function of aperture size (and equivalently angle, with the small apertures having a higher angle) and mirror for a planar DBR and a 9 period (6.1 μm) TE-HCG. DBRs (blue) show a differentiation in loss between the 1st (blue, solid) and 2nd (blue, dashed) order modes of the VCSEL only at very small aperture sizes. HCGs (red) on the other hand, show a strong differentiation between 1st (red, solid) and 2nd order (red, dashed) modes.

Note that at aperture sizes above 4.5 μm, the finite size of the HCG (6.1 μm) also starts to affect the overall mirror loss, causing the mirror loss to increase as the aperture size becomes on the order of the size of the HCG, so the edge of the mode starts to exceed the HCG area. Larger area HCGs would not show this same effect. In the best case, it can be engineered to further increase the single mode aperture size, because at some aperture size the 2nd order mode does see low enough loss to also lase. If the HCG size is picked to be just larger than that point, this rise due to the finite HCG area would allow for an even larger aperture size single mode VCSEL. The other interesting conclusion to be drawn from Figure 2.6 is that a larger aperture is required for an HCG VCSEL to lase in the first place than a DBR VCSEL.

2.5.3 Experiment

In experiment, this mode differentiation is seen. An HCG VCSEL and a VCSEL with a standard top DBR mirror containing 24 pairs of DBR were fabricated for comparison. Further details on the HCG VCSEL structure and fabrication can be found in section 3.3. Figure 2.7 shows the spectrum of both an HCG VCSEL (red) with 8 periods (5.5 μm) and a DBR VCSEL (blue). Both VCSELs have the same underlying structure and approximately the same aperture size of around 5 μm. The only difference between the structures was the top mirror: one had an HCG and the other a standard 22 pairs of DBR. The HCG VCSEL in this case is single mode, while the DBR VCSEL is highly multimode, agreeing well with the simulation. Indeed the larger required aperture size to achieve lasing compared to the DBR was also seen in experiment.

Further experimental study of the HCG's mode control characteristics for a TM-HCG can be found in reference [71].

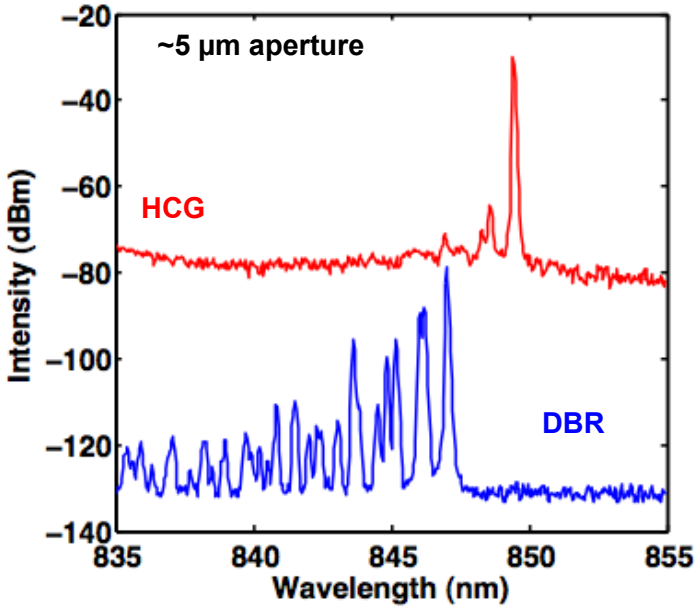

Figure 2.7 Spectrum of a 8 period (5.5 μm) TE-HCG VCSEL (red) and a DBR VCSEL (blue) with approximately the same aperture size of around 5 μm. While the HCG VCSEL is single mode, the DBR VCSEL is highly multimode.

2.6 Minimum High Contrast Grating Size

Initial analysis [73], [74] of HCGs was performed assuming infinite periodicity along the direction of periodicity and infinitely long grating bars, but in practice both dimensions are finite. The reflectivity of a HCG does not have an obvious limitation based on the lateral area. HCG simulation and design are typically are performed using the Rigorous Coupled Wave Analysis (RCWA) method [92]. This method assumes infinite periodicity, so the effect of reducing the grating to just a few periods is not obvious. Analytic treatment of the HCG structure [89] shows that there are no propagating waves in the plane of the HCG, so intuitively the size of the HCG should not significantly affect the overall reflectivity of the grating, as there is no dependence of a given grating period on the number of periods to its sides.

2.6.1 Simulation

To simulate the case of TE-HCGs with a finite number of periods, the reflectivity of a HCG was calculated using a finite-difference time-domain (FDTD) simulation (using the commercial software Lumerical FDTD Solutions). The simulation was performed varying two parameters: the grating size (number of periods) and the size of the oxide aperture. The reflectivity was calculated by launching a Gaussian beam with waist the size of the aperture through the entire top mirror structure, including 4 pairs of DBR, from the aperture and measuring the reflected power. The TE-HCG in the simulation was 145 nm thick, had a 640 nm period, and a ~400 nm

air gap and was designed for high reflectivity at 850 nm (further details on this HCG design can be found in section 3.3.2). The wavelength of the Gaussian beam used in the simulation was 850 nm. From this reflectivity, mirror loss could be calculated for each case.

The results are shown in Figure 2.8. As the HCG is shrunk, the mirror loss is not significantly affected until the HCG becomes approximately the same size as the aperture itself. As the size is further decreased to less than the size of the aperture, the mirror loss increases significantly, since the high reflectivity HCG region no longer covers the whole beam width. This result indicates that in fact there is little effect on the reflectivity of the HCG on the number of periods of the HCG.

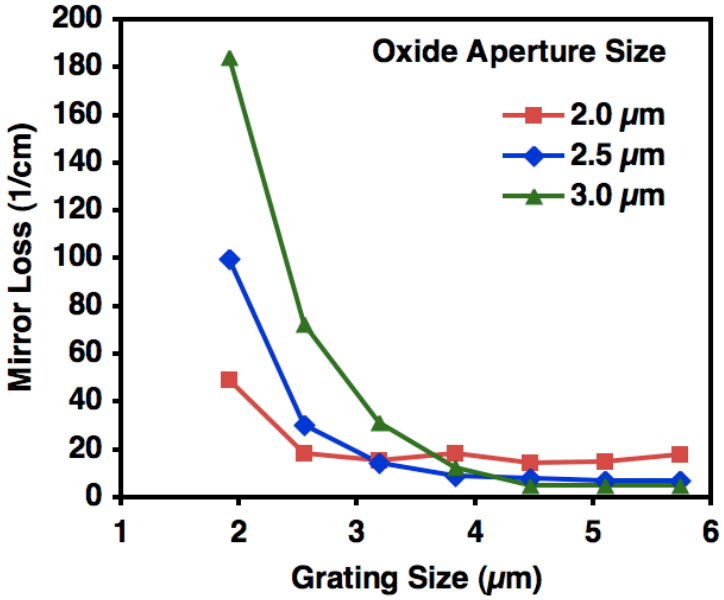

Figure 2.8 Mirror loss of the TE-HCG structure as a function of mirror loss and grating size. The mirror loss of the device is constant until the HCG is slightly larger than the aperture size, indicating the reflectivity of the HCG is not significantly impacted by the number of periods in the structure.

2.6.2 Experiment

To experimentally probe the effect of size of the TE-HCG on VCSEL performance, a series of TE-HCG tunable VCSELs were fabricated with square HCGs of sizes from 12 μm (18 periods) down to 2.3 μm (3 periods). The VCSELs in this study were fabricated on the same wafer at the same time to ensure uniformity. Further details on the HCG VCSEL structure and fabrication can be found in section 3.3. VCSELs were found to lase with HCGs of as few as 4 periods (2.9 μm × 3 μm × 145 nm). Scanning electron microscopy (SEM) images of the series of HCGs down to 3 HCG periods are shown in Figure 2.9.

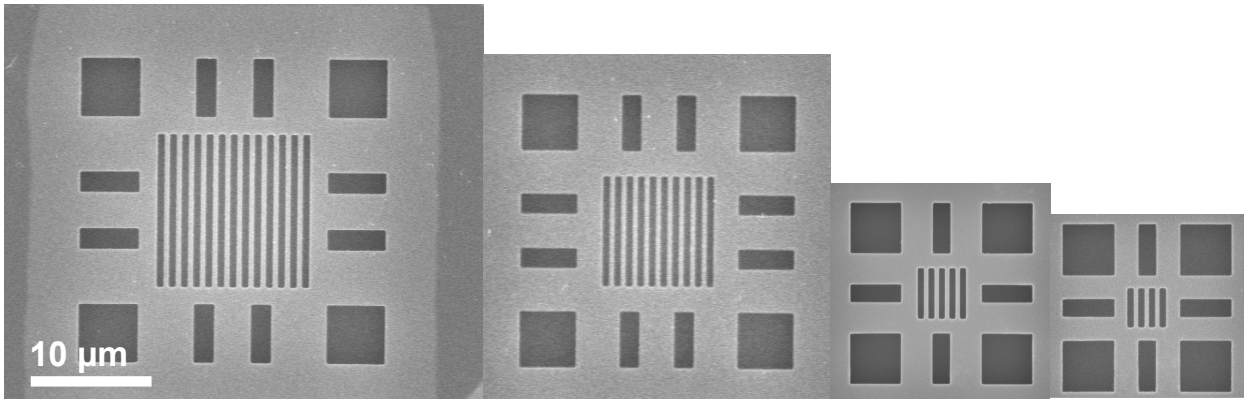

Figure 2.9 SEM images of the series of fabricated HCGs integrated on VCSELs. a) 12 periods (8 µm X 8 µm). b) 9 periods (6 µm X 6 µm). c) 4 periods (2.9 µm X 3.0 µm). d) 3 periods (2.3 X 2.5 µm). The VCSELs lased with HCGs down to 4 periods (c).

Light-current characteristics of the VCSELs with various sizes of TE-HCG are shown in Figure 2.10 a). The devices have approximately the same size oxide aperture, estimated to be ~3 µm, and are otherwise identical except for the HCG size. It should be mentioned that the oxidation process was performed on an approximately 100 µm size mesa, and hence there is an inherent inaccuracy of ~1 µm between the HCG and oxide aperture. The threshold current and maximum differential resistance as a function of mirror size are shown in Figure 2.10 b) and c), respectively. The VCSELs show similar characteristics until the HCG has less than 7 periods (4.8 µm). When the HCG has fewer periods than 7, its threshold increases as the number of periods is further reduced. No devices with 3 periods lased experimentally, though with better alignment of the HCG to the aperture and matching of the aperture size of the HCG, this may be possible. This trend matches well with the simulation, which shows that mirror loss and correspondingly, laser threshold is constant until the HCG is only slightly larger than the aperture. These devices have an oxide aperture size of 3±1 µm, so we observe a similar trend experimentally. This shows that, in fact, the number of HCG periods does not have a significant effect on the overall reflectivity. Only the physical overlap of the mirror itself with the aperture is significant.

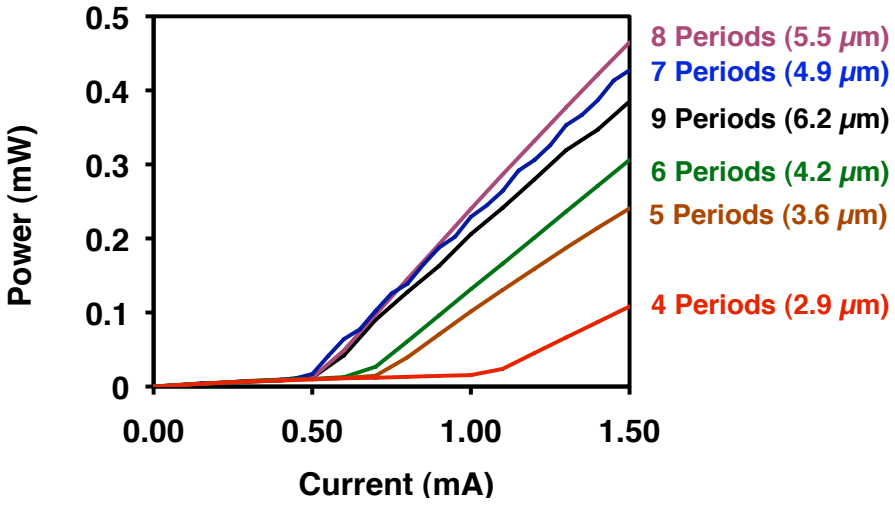

(a)

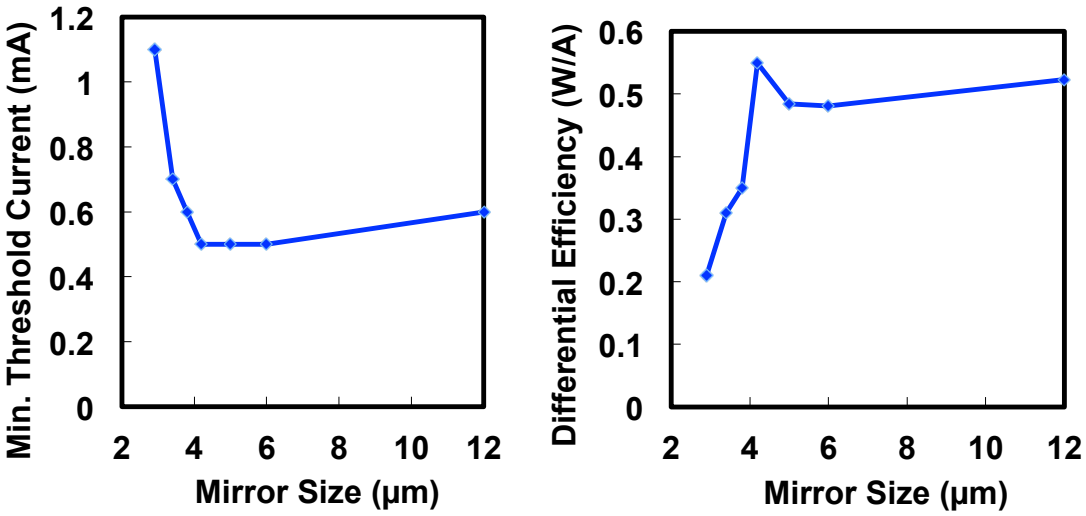

(b) (c)

Figure 2.10 a) Light-current characteristics of TE-HCG VCSELs with different size HCGs. Device characteristics are nearly unchanged until the HCG has less than 7 periods (4.8 μm). b) Minimum threshold current as a function of HCG size of VCSELs where the rest of the structure is the same. c) Maximum differential efficiency as a function of HCG mirror size. Experimentally, little effect is seen on device performance until the HCG has fewer than 7 periods.

2.7 Spacer Layer Requirements

An important parameter to keep in mind when designing VCSELs with a high contrast grating is the distance between the high contrast grating and the rest of the VCSEL structure. Because the HCG spacing is not subwavelength in the semiconductor in the VCSEL body, if the VCSEL body is too close to the grating, the first diffraction order is no longer totally evanescent

and can propagate in the VCSEL body. Any power that leaks out into the first order mode is lost, so reflectivity back into the VCSEL is reduced. Through rigorous analysis [89], it can be shown that the attenuation constant of the evanescent mode goes as:

$$\alpha \propto \sqrt{(\frac{\lambda}{\Lambda})^2 - n^2} \tag{2.1}$$

where λ is the wavelength of interest, Λ is the grating period, and n is the index of the material between the HCG and the VCSEL. Thus, if one wants to bring the HCG as close as possible to the VCSEL body, which is desirable for reducing cavity losses due to diffraction loss, it is best to have as small of an HCG period as possible and as low as possible refractive index medium between the HCG and VCSEL body.

Figure 2.11 shows the reflectivity of both a TM and TE HCG as simulated by RCWA as a function of the thickness of the low index media between the HCG and VCSEL body. The simulation wavelength was 1.55 μm. The simulation structure was the same as in section 2.3, consisting of an InP substrate (n = 3.16), on top of a SiO2 layer (n = 1.47). The HCG material is Si (n = 3.48). A loss of k=0.0005 was used in the silicon to approximate small losses due to free carrier absorption, etc. For the TM design, the period was 700 nm, the grating thickness 460 nm; the semiconductor duty cycle 75%, equivalently, an air gap of 175 nm. For the TE design, the period is 985 nm; grating thickness 243 nm; semiconductor duty cycle 26%; and SiO_2 thickness 1.67 μm.

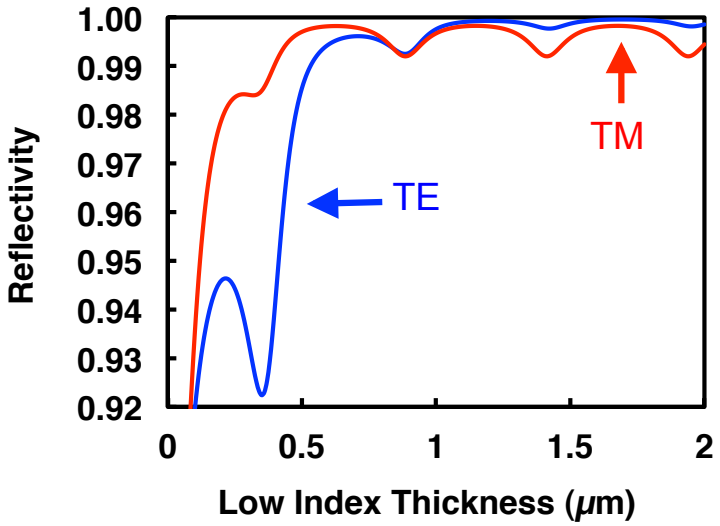

Figure 2.11 The reflectivity of a TE (blue) and TM (red) HCG as a function of the thickness of the low index media (in this case SiO_2) between the HCG and VCSEL body. The TM HCG can be closer to the VCSEL body due to it's smaller period.

In this case the TM HCG design can be closer to the VCSEL body due to its smaller period of 700 nm compared to the TE's 985 nm period. The TM design has sufficient reflectivity at as little as ~780 nm of SiO_2 spacer whereas the TE design requires a minimum of ~1200 nm of SiO_2 spacer. A periodic dip can be seen in the reflection as a function of air gap. This

corresponds to the point where the reflected light from the HCG is exactly out of phase with the reflection from the interface between the VCSEL body and low index material.

2.8 Tolerance to Fabrication Error

In order for a high contrast grating to be useful in a mass produced product, it must also be tolerant to errors inherent in the fabrication process. None of the dimensions, duty cycle, period, or thickness can be too critical or achieving repeatable device performance will not be possible, so a HCG should be designed such that it can tolerate errors during fabrication. Generally there is a tradeoff between all of these parameters as well as with the bandwidth of the high reflectivity section.

2.8.1 Key Parameters

From a practical point of view, the duty cycle of a high contrast grating is the most difficult variable to control. In modern lithography systems, the width of an opening is sensitive to the exposure conditions such as exposure dosage and focal depth, so it is desirable to have an HCG that provides high reflectivity despite any fabrication imperfections causing a difference in duty cycle. Using the Marvell Lab at UC-Berkeley, lithographic grating patterns can be repeatedly achieved with grating air gaps of ±20 nm from the designed dimension. This can be achieved using either electron beam lithography or DUV stepper lithography. Though in a state-of-the-art industry cleanroom, higher accuracy may be achievable, it is always desirable to have a larger tolerance to error as higher accuracy requires more cost and calibration.

The period of the grating can typically be controlled down to the nanometer but not sub-nanometer scale, so it is desirable to have some tolerance to period as well in the design. We typically design our high contrast gratings to be tolerable to ±10 nm error in period.

The thickness of the grating is generally the variable which is the best controlled. In a VCSEL, the HCG layer can be epitaxially grown to high precision. Modern MOCVD growth techniques routinely achieve ±1% of the desired thickness. This precision is required in a VCSEL structure, as otherwise the cavity and gain would be detuned too imprecisely to repeatably achieve high performance VCSELs. Thus, we can assume the high contrast grating layer to be within ±5 nm of the desired design thickness. In some cases though, it may be desirable to deposit the HCG material, such as if the HCG is to be sitting on a low index oxide instead of totally suspended in air. In the case of a deposited HCG layer, a much larger tolerance to thickness is desirable. Such a design is presented in section 4.2.

2.8.2 Example Design

The reflectivity at 850 nm as a function of period and grating air gap width of an example TE HCG design is shown in Figure 2.12. The design is simulated using rigorous coupled wave analysis (RCWA) [92]. This design is optimized for a large tolerance to air gap width while maintaining a reasonable tolerance to period (±10 nm) and thickness (±5 nm). At the middle of the range of desirable periods (635 nm), anywhere between 320 nm and 420 nm air gaps provide enough reflectivity for a VCSEL to lase (~99.5%). This provides a margin of error of ±14% from the design center. Even if the period were off by 10 nm to 645 nm, an approximately 80 nm window of air gaps (or ±11% from the design center) would provide sufficient reflectivity.

The other direction, 625 nm, has an even larger window of high reflectivity air gaps, ~130 nm (or ±17% from the design center).

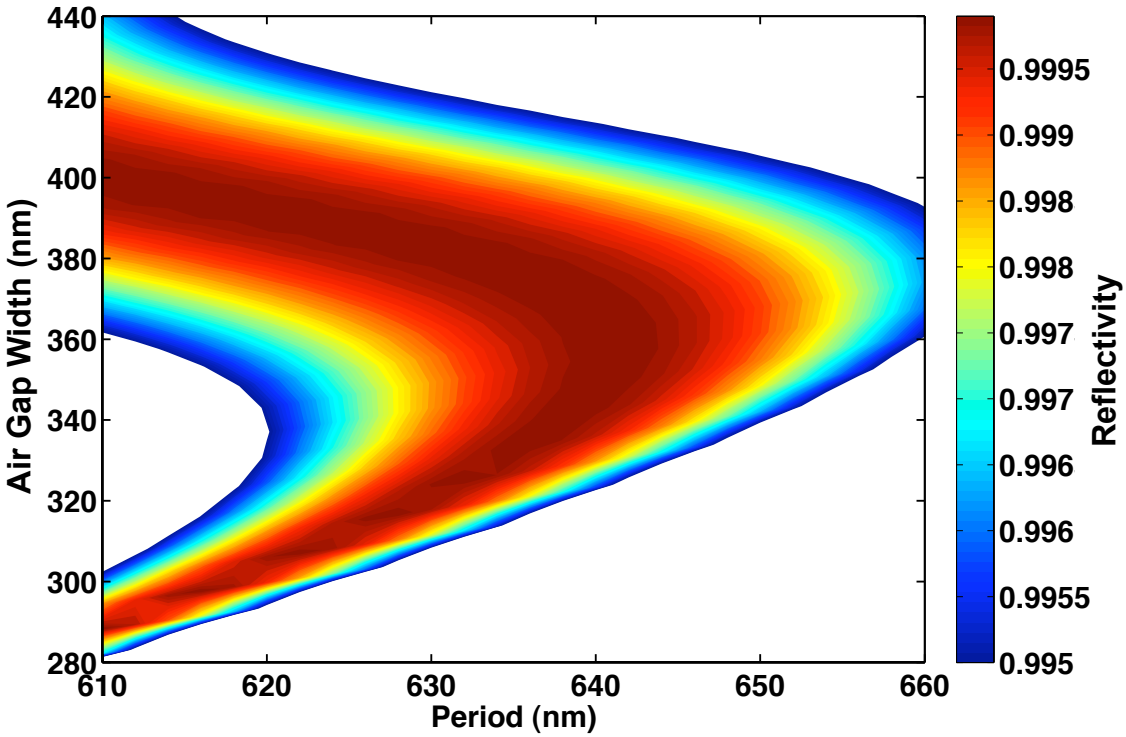

Figure 2.12 HCG Reflectivity as a function of the grating's air gap width and period. The RCWA simulation is performed using a grating thickness of 145 nm and at a wavelength of 850 nm using TE-polarized light.

Figure 2.13 shows reflectivity as a function of wavelength and duty cycle (here semiconductor duty cycle, equivalent air gaps are also noted) at a fixed period of 640 nm and simulated using TE-polarized light. The tolerance of the grating to duty cycle variation as a function of wavelength is also seen to be quite good. The reflectivity bandwidth of the grating is over 100 nm wide across nearly a 100 nm range of air gaps at a fixed period.

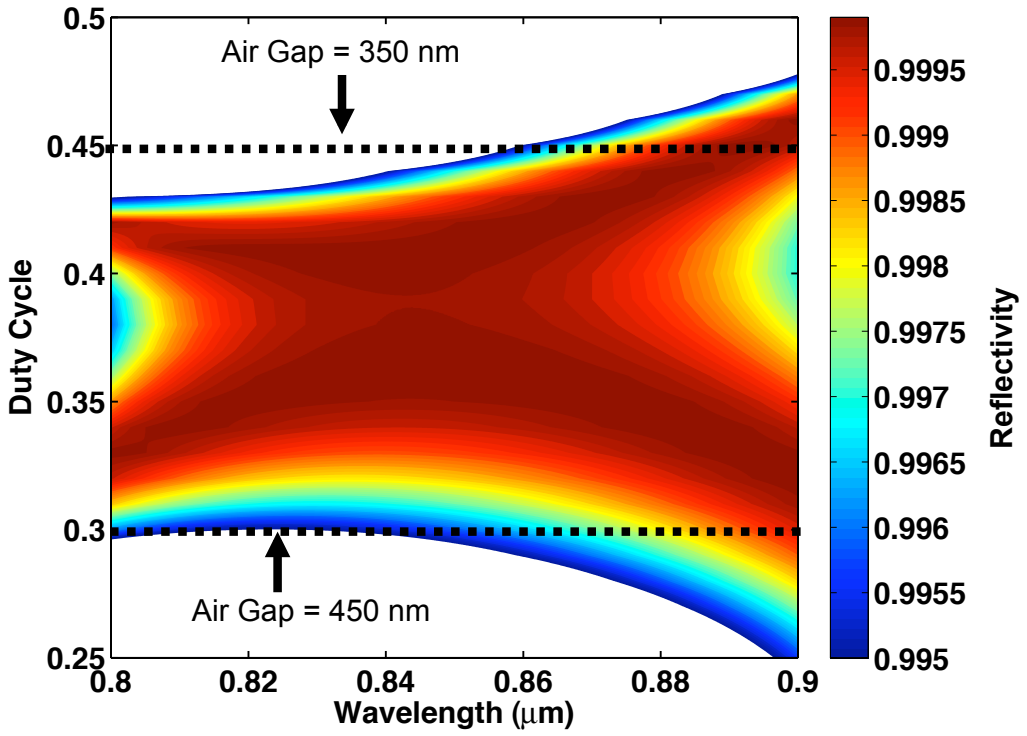

Figure 2.13 HCG reflectivity as a function of wavelength and duty cycle (equivalently air gap) at a fixed grating period of 640 nm using TE-polarized light.

2.8.3 Experimental Verification

To verify this design, a range of TE HCG designs were fabricated on an 850 nm HCG VCSEL with an HCG layer of ~145 nm. Further fabrication and device design details can be found in section 3.3. At a period of 640 nm, VCSELs with HCG air gap spacings from 328 to 420 nm were found to lase, verifying the simulation results. SEM pictures and light-current characteristics of the fabricated HCGs are shown in Figure 2.14. Despite being on the edge of the target dimension zone, the devices still have reasonable threshold currents and slope efficiencies. A similar study was performed on TM HCG VCSELs [93] varying the period as well as air gap. A similar robustness to variation was seen for the TM HCGs.

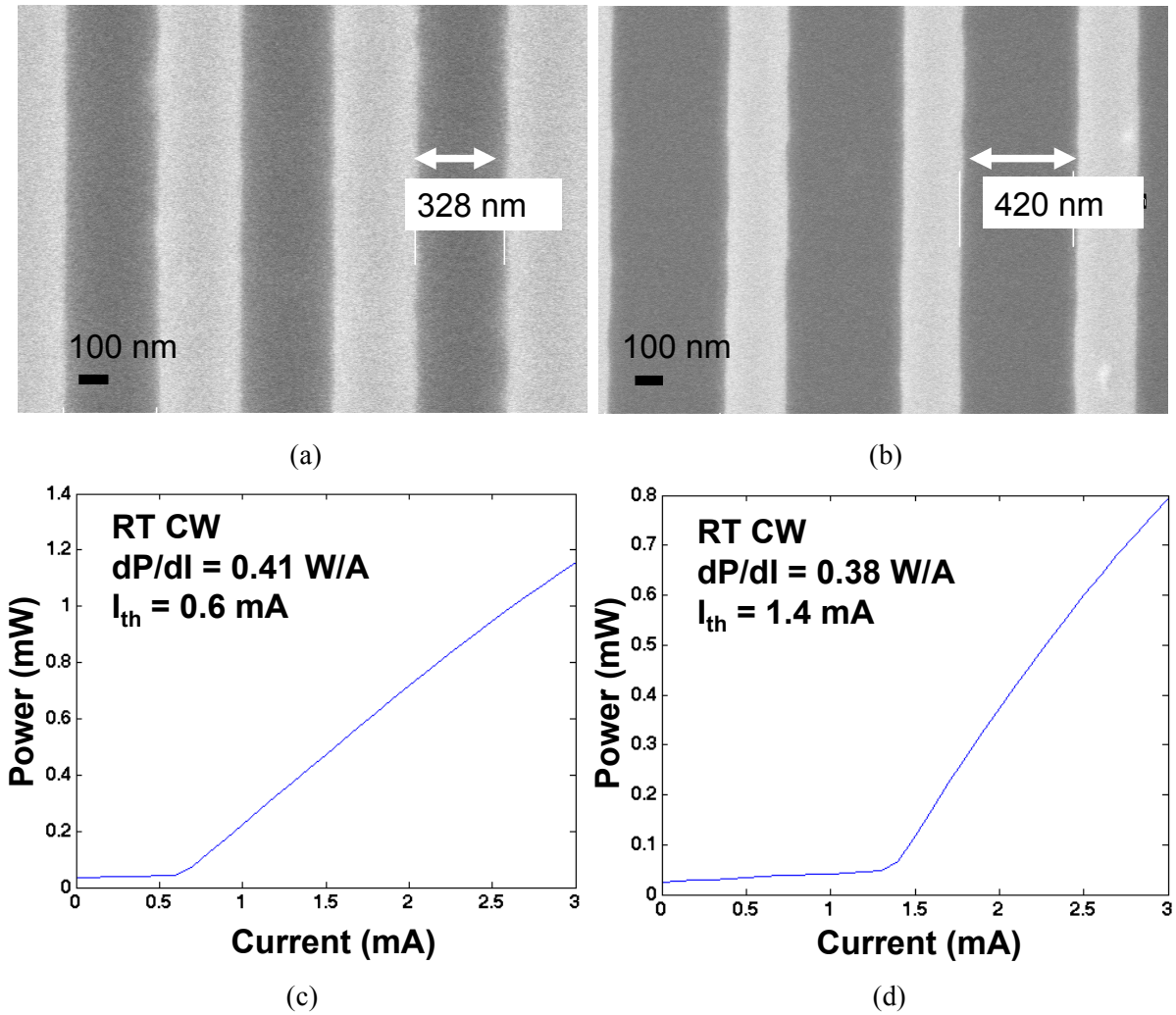

Figure 2.14 HCGs of different dimensions on the same underlying VCSEL structure. Despite much different air gaps, the VCSELs still lase, verifying the range of working HCG designs predicted by simulation. a) SEM picture of an HCG with a 328 nm air gap. b) SEM picture of a HCG with 420 nm air gap. c) Light-current characteristic of the VCSEL with HCG from a). d) Light-current characteristic of the VCSEL with HCG from b).

2.8.4 Variation across the HCG

Another interesting point of consideration is the effect of variation across the same HCG. When patterning HCGs using electron beam lithography for example, variation in HCG air gap is often seen due to the proximity effect [94] in electron beam lithography. Since the HCG is typically designed to work over a wide range of air gaps, intuitively it is not expected that variation of the air gap across the grating should have a major effect on the grating's reflectivity.

In experiment, this is seen to be true. Figure 2.15 a) shows an SEM image of a fabricated HCG where the photoresist was underexposed and residues remained on the surface after the device was completed. Figure 2.15 b) is zoomed in on the same HCG as seen in part a). Across

the HCG, the air gap is seen to vary from 96 nm to 142 nm due to the photoresist residues pulling the bars towards each other. Figure 2.16 shows the light-current curve of the device from a) and b). The device has a higher threshold than normal indicating a lower HCG reflectivity than normal, but still lases despite the fabrication defects.

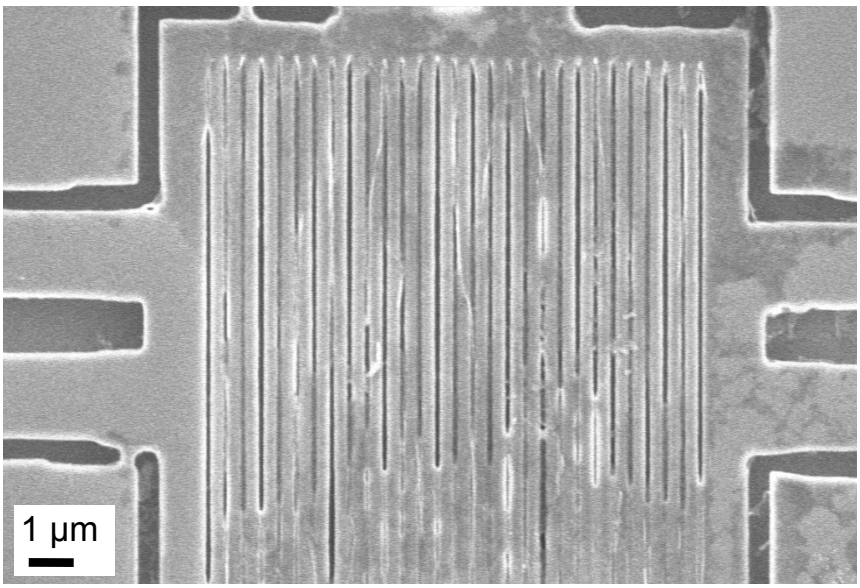

(a)

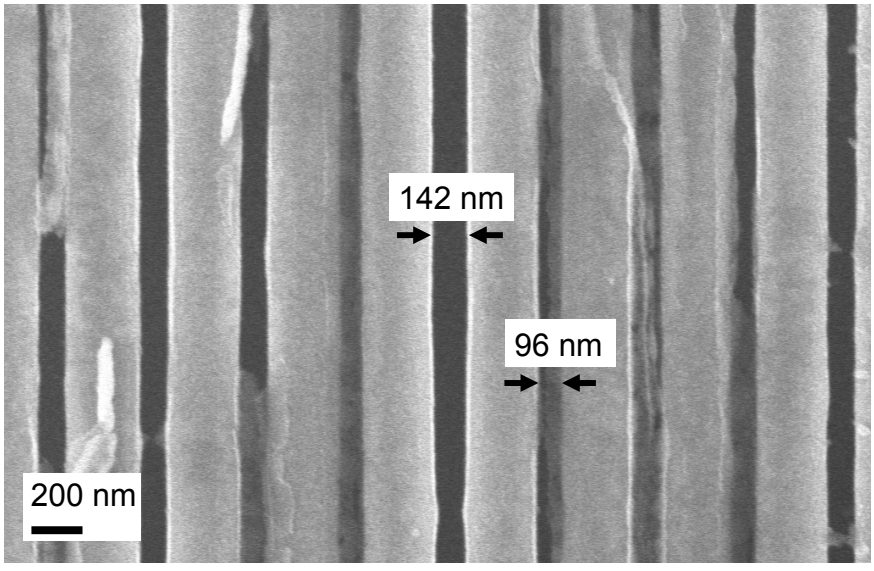

(b)

Figure 2.15 a) SEM picture of a fabricated TM HCG. Despite major non-idealities in the HCG, the VCSEL with this HCG lases. b) A zoomed in SEM picture of the same HCG as part a). The air gap is seen to vary from 96 nm to 142 nm across the same HCG.

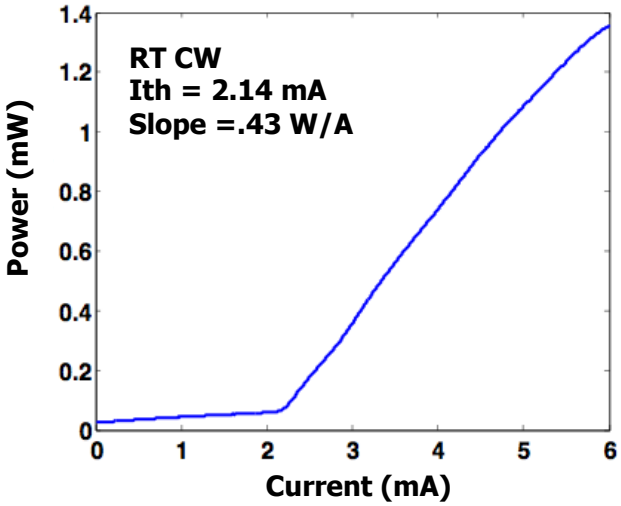

Figure 2.16 The light-current curve of the device from Figure 2.15. The device does have a higher threshold than normal indicating a lower HCG reflectivity than normal, but nonetheless lases.

2.9 Summary

In this chapter, we described high contrast gratings and their properties, especially with respect to VCSELs. Their basic properties have been explored as well as their features that can be exploited to create VCSELs with favorable properties, such as polarization anisotropy and higher order transverse mode selection. Additionally practical topics in their application to VCSELs were discussed such as their size, spacer layer requirements, and tolerance to fabrication error. Record small HCGs with as few as 4 periods (2.9 μm × 3 μm × 145 nm) were shown experimentally to provide sufficient reflectivity for a VCSEL to lase.

In the next chapters, we examine the HCG as applied to tunable VCSELs, InP-based VCSELs, and multiwavelength VCSEL arrays.

Chapter 3 Ultra-Fast Wavelength Tunable VCSELs using a High Contrast Grating

3.1 Motivation

Wavelength tuning speed is a critical performance parameter for tunable lasers. Designers for next generation optical communications networks desire low cost laser sources that can be tuned on a nanosecond time scale. Unfortunately, conventional tunable VCSELs have been unable to achieve that fast of a wavelength tuning speed. Their thick movable mirrors, on the order of microns thick, limits tuning times to the order of microseconds.

After HCGs were demonstrated as a suitable mirror in a VCSEL structure [77], [95], they were quickly recognized to offer a significant advantage in terms of wavelength tuning speed because of their reduced thickness. They were integrated into a tunable VCSEL structure [76] with the expectation of much higher tuning speeds than a conventional DBR-based tunable VCSEL structure, since the HCG is less than 5% of the thickness of the DBR it replaces. By integrating a TM HCG (245 nm thick, for a reflectivity band at 850 nm) into the movable mirror element in place of a DBR, a significant improvement in tuning response, to 3.3 MHz, was realized due to the 10X reduction in mirror thickness [52]. Afterwards, an even thinner (145 nm) transverse electric TE-HCG was integrated, resulting in a tuning response as high as 4.5 MHz [96].

By decreasing the size of the HCG to the smallest possible lateral area, we can further increase the resonance frequency of the mechanical structure because of the reduction in the mass of the mirror. Additionally, the actuators for the structure can be further stiffened from previous work. This chapter discusses the optimization of tunable VCSEL tuning speed, which allows us to fabricate structures with resonance frequencies much higher than those in previous works.

3.2 Case for a Thinner Mirror

The need for a thinner mirror is not totally obvious at first glance. The resonance frequency for any mechanical structure can be simply written as:

$$\omega = \sqrt{\frac{k}{m}} \tag{3.1}$$

where k is the stiffness of the mirror's actuators, and m is the mass of the movable element.

For the case of a tunable VCSEL it is convenient for the thickness of the actuators and the mirror itself to be the same thicknesses, otherwise complex fabrication processes are needed. A schematic of a typical tunable VCSEL structure is shown in Figure 3.1. The mirror of thickness t_{Mirror} is actuated towards the VCSEL body by a distance of Δd from it's resting position of d_0 by an electrostatic force between the mirror and VCSEL due to a voltage V applied between the mirror and the VCSEL body.

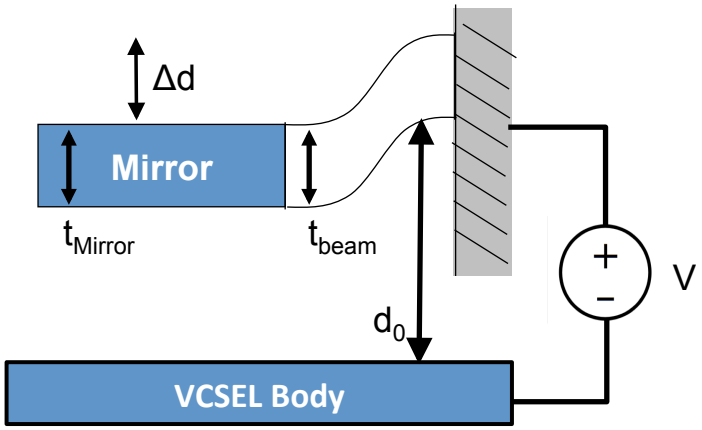

Figure 3.1 Schematic of a typical MEMS tunable VCSEL structure. The mirror and actuator thicknesses, t_{mirror} and t_{beam} respectively, are typically the same. A voltage V applied between the mirror and VCSEL body actuates the mirror by a distance of Δd towards the VCSEL body from its resting distance of d_0.

In the case of a simple cantilever, $k \propto t_{beam}^3$ [97] and $m \propto t_{Mirror}$. Since $t_{beam} = t_{Mirror}$, $\omega \propto t$. At first glance then, the device is expected to operate at a faster tuning speed with a thicker mirror. This simple analysis ignores other constraints on the system though. The stiffness k can also be written as:

$$k = \frac{F}{\Delta d} \tag{3.2}$$

where Δd is the displacement of the mirror due to the force F. Δd is directly related to the amount of wavelength shift of the VCSEL cavity, $\Delta d \propto \Delta\lambda$. Thus to achieve a certain required minimum tuning range $\Delta\lambda_{min}$, a certain minimum displacement Δd_{min} is required.

Force can also be written as:

$$F = \frac{\varepsilon A V^2}{(d_0 - \Delta d)^2} \tag{3.3}$$

where A is the area of the mirror; V the voltage applied between the mirror and VCSEL body; and ε the dielectric constant of air. Here again there is a system constraint. Typically, there is a maximum system voltage that can be applied V_{max}, and d_0 is dictated by the VCSEL design. Taking this into account, k can be rewritten as:

$$k = \frac{\varepsilon A V_{\max}^{\ 2}}{\Delta d_{\min}(d_0 - \Delta d_{\min})^2} \tag{3.4}$$

The mass of the mirror itself is:

$$m = \rho\, tA \tag{3.5}$$

where ρ is the density of the mirror material, t is the grating thickness, and A is the area. Rewriting ω in terms of k and m with the constraints of a maximum voltage V_{max}, and minimum wavelength range and corresponding actuation range Δd, ω is:

$$\omega = \sqrt{\frac{\varepsilon A V_{\max}^{\ 2}}{\Delta d_{\min}(d_0 - \Delta d_{\min})^2 m}} = \sqrt{\frac{\varepsilon V_{\max}^{\ 2}}{\Delta d_{\min}(d_0 - \Delta d_{\min})^2 \rho t}} \tag{3.6}$$

Thus, $\omega \propto \sqrt{1/t}$. Therefore, when realizing a practical system with a maximum tuning voltage and a required tuning range and corresponding distance that the mirror is required to move, the thinner the mirror, the higher the maximum tuning frequency is that can be achieved.

3.3 VCSEL Design and Characteristics

3.3.1 VCSEL Design

The devices used in the following simulations and experiment are of similar design to previous nano-electromechanical optoelectronic (NEMO) tunable VCSEL designs [52], [96]. A schematic of the fabricated tunable VCSEL structure is shown in Figure 3.2. The structure is comprised of (starting from the *n*-GaAs substrate) 34 pairs of *n*-DBR consisting of alternating layers of $Al_{0.90}Ga_{0.10}As$ and $Al_{0.12}Ga_{0.88}As$, an active region with 3 GaAs quantum wells designed to emit at 850 nm, an aluminum oxide aperture to provide optical and current confinement. Above that is a top mirror consisting of 2 or 4 pairs of *p*-DBR of the same materials as the *n*-DBR, an air gap of ~900 nm, and a 145 nm thick *n*-TE-HCG layer of $Al_{0.6}Ga_{0.4}As$.

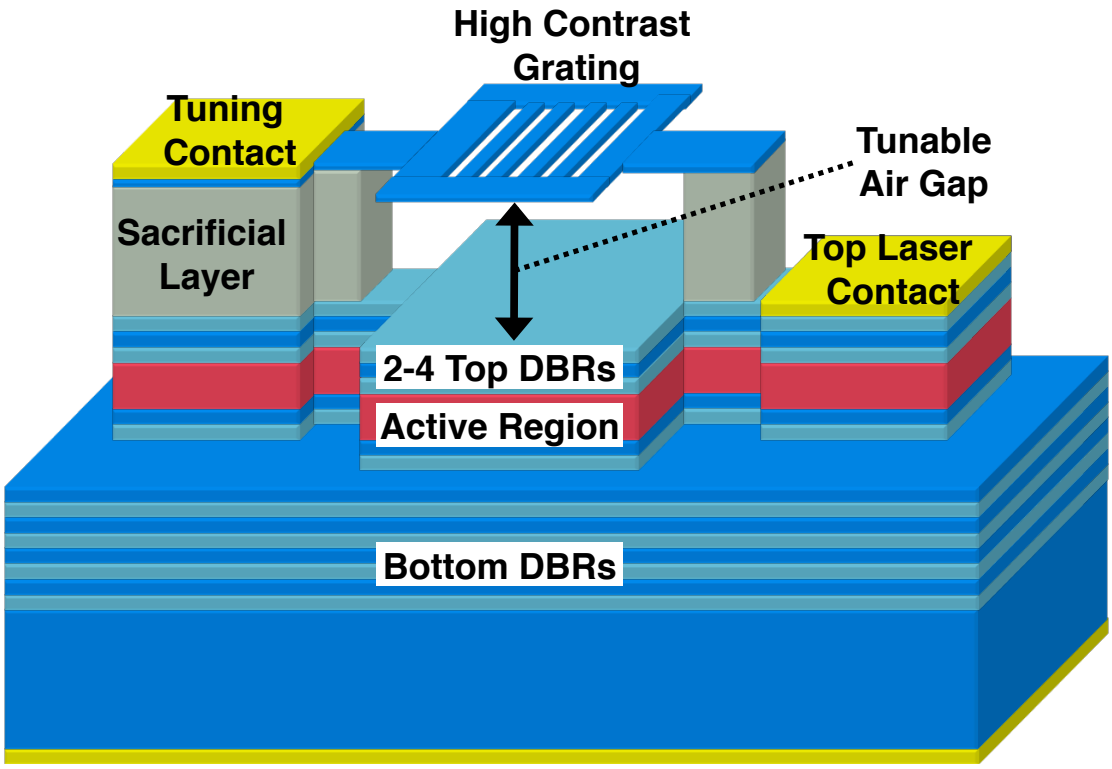

Figure 3.2 Schematic of a NEMO tunable VCSEL with a suspended TE-HCG in place of a typical top DBR.

Current is injected through the top laser contact to the *p*-DBR, which is present in the design only to provide current injection and protect the active region, to a backside contact on the bottom of the substrate. The HCG is fixed to supports by beams made up of the HCG material and can be electrostatically actuated by applying a reverse-bias voltage between the top tuning contact and top laser contact.

To verify the design, the electric field inside of the 850 nm VCSEL structure is simulated using a transmission matrix method [98]. A field is launched from one side of the structure, and recorded as it propagates through a transmission matrix that is incrementally increased in length. Figure 3.3 shows the electric field (blue) in the structure as well as the refractive index (red). The electric field is maximized across the active region to achieve as large an overlap factor as possible. The overlap factor is calculated to be 3.6%. The calculation is performed by integrating the field in the active region and dividing by the integral of the field throughout the structure, neglecting the field in the HCG itself, which is small. The lateral confinement is also assumed to be one.

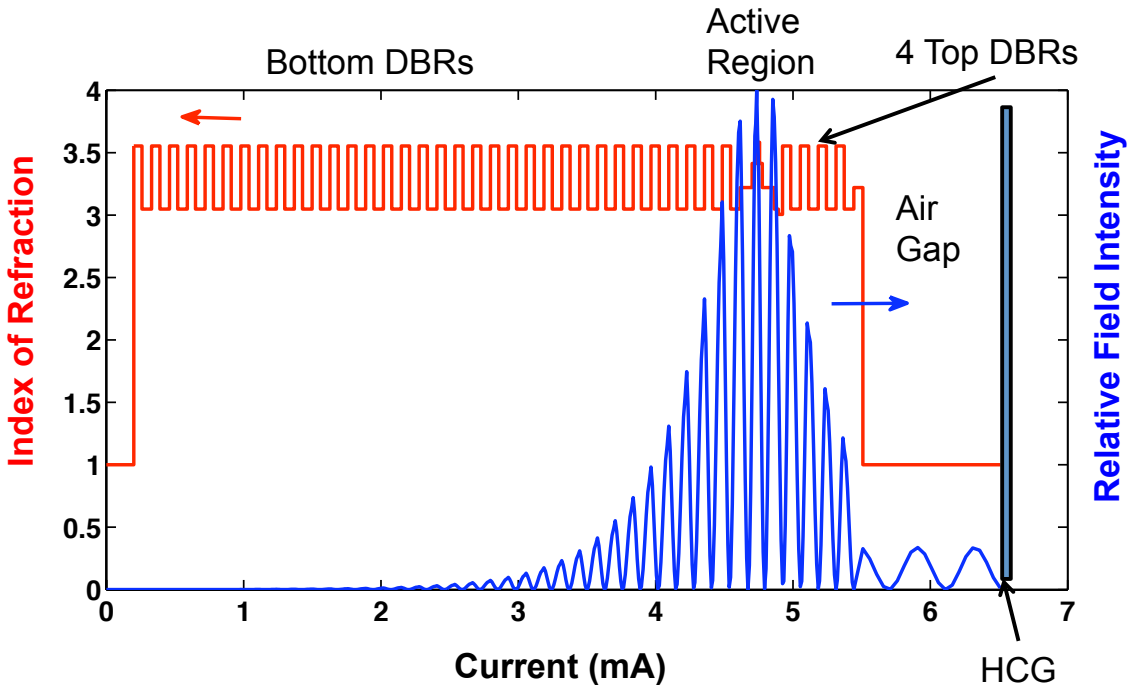

Figure 3.3 Electric field (blue) and index of refraction (red) as a function of distance inside of the 850 nm GaAs-based HCG VCSEL structure. The overlap factor of the electric field with the active region is 3.6%.

3.3.2 HCG Design

The TE-HCG used in this study has a period of 640 nm, a semiconductor duty cycle of approximately 38%, an HCG thickness of 145 nm, and an air gap of approximately 900 nm under no tuning bias. The reflectivity of the HCG as calculated by RCWA [92] is shown in Figure 3.4 under both TE (blue, electric field polarized along the direction of the HCG bars) and TM (red, electric field polarized perpendicular to the direction of the HCG bars) incident light. For TE light, there is a >99.9% bandwidth of over a 60 nm range. TM light on the other hand sees less than 50% reflectivity across much of the same range, so a high loss differentiation between the degenerate polarization modes in the VCSEL is expected. The HCG is made up of $Al_{0.6}Ga_{0.4}As$ (n = 3.2585 at 850 nm [99]) surrounded by air (n = 1) as the low index material.

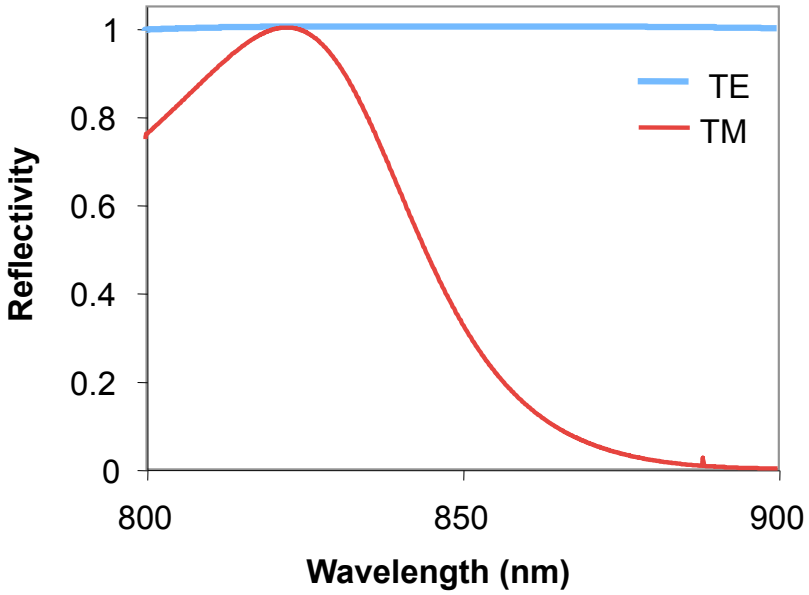

Figure 3.4 Reflectivity as calculated by RCWA for the 850 nm TE HCG for both incoming TE (blue) and TM (red) light. The design has a 60 nm band of reflectivity >99.9% for TE light but is much less reflective for TM light.

3.3.3 Tunable VCSEL Cavity Design

Actuating the HCG mirror closer to the VCSEL cavity changes the wavelength of the VCSEL. This actuation changes the size of the air gap and cavity length, shifting the output wavelength of the device. An RCWA [92] simulation of the Fabry-Pérot cavity wavelength versus the size of the air gap between the HCG and VCSEL body is shown in Figure 3.5. The gain bandwidth of the quantum wells, about 30 nm, is indicated in light red. The unactuated HCG is 900 nm from the VCSEL body, which gives a cavity emission of ~840 nm. Around 900 nm air gap the tuning coefficient is approximately 0.02 nm of wavelength shift per nm of physical mirror movement. As the air gap moves away from the unactuated state, the tuning coefficient increases and eventually moves out of the gain bandwidth of the quantum wells. Eventually, another mode moves into the cavity. The mode spacing in this design is approximately 30 nm. With more aggressive cavity designs, a larger mode spacing is achievable, allowing for larger tuning ranges when combined with an active region with a larger gain bandwidth.

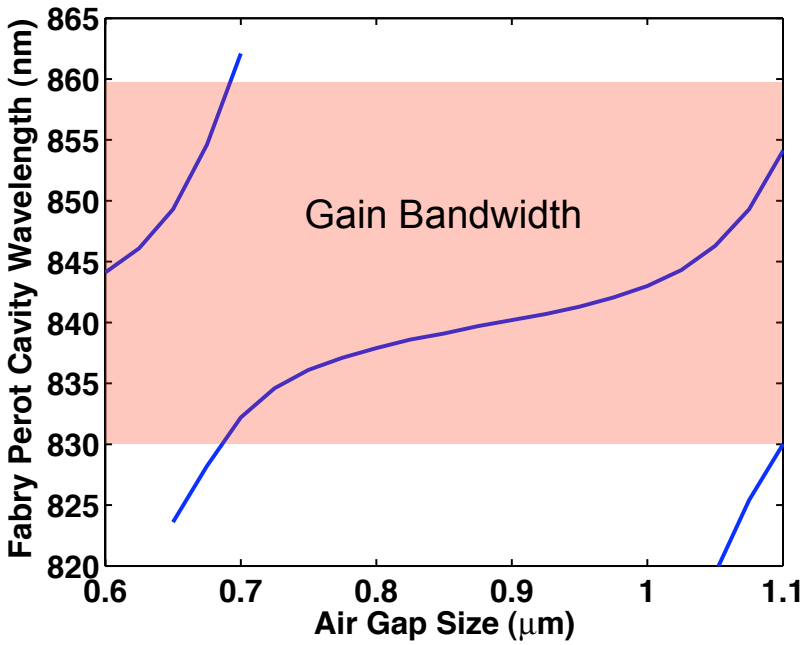

Figure 3.5 Fabry-Pérot cavity wavelength (blue) as a function of the size of the air gap between the HCG and VCSEL body. The approximate gain bandwidth of the quantum wells is overlaid in red. A tuning coefficient of 0.02 nm of wavelength shift/nm of mechanical movement is obtained with this structure.

3.3.4 VCSEL Fabrication Process

After epitaxial growth, the devices are fabricated by first depositing the tuning contact, shown in Figure 3.6 a) followed by a sulfuric acid-based wet etch down to the bottom DBRs to form electrically isolated mesas. Next, selective thermal oxidation of an $Al_{0.98}Ga_{0.02}As$ layer in the structure is used to form an oxide aperture for current confinement, shown in Figure 3.6 b). Afterwards, a two-step etch is used to reach the *p*-DBR and laser contact layer. First a sulfuric acid-based etch is used to etch through the HCG layer. Then, a citric acid-based selective etch is used to etch away the GaAs sacrificial layer and expose the *p*-DBR. After that, the metal is evaporated on the exposed *p*-DBR to form the top laser contact, shown in Figure 3.6 c). The backside *n*-contact is formed by a uniform evaporation of metal on the backside of the wafer. Finally, electron beam lithography is used to pattern the HCG. The HCG pattern is transferred via a RIE dry etch using $SiCl_4$, shown in Figure 3.6 d). Finally, the HCG is released from the rest of the structure using a citric-acid-based selective etch. This is followed by critical point drying to prevent pull-in of the HCG during the drying process, shown in Figure 3.6 e).

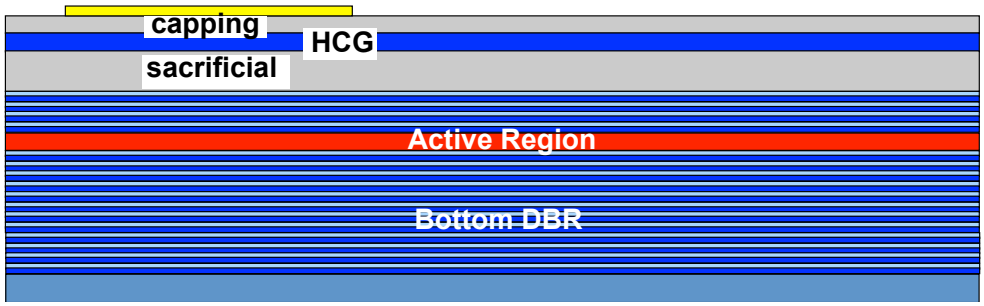
capping
HCG
sacrificial
Active Region
Bottom DBR

(a)

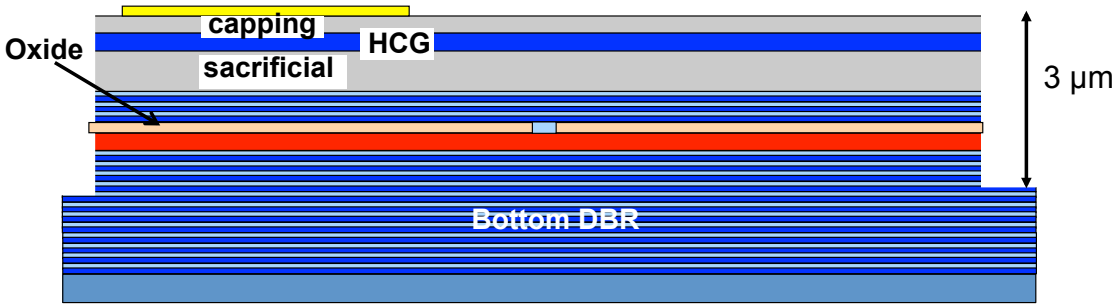
Oxide
capping
HCG
sacrificial
3 μm
Bottom DBR

(b)

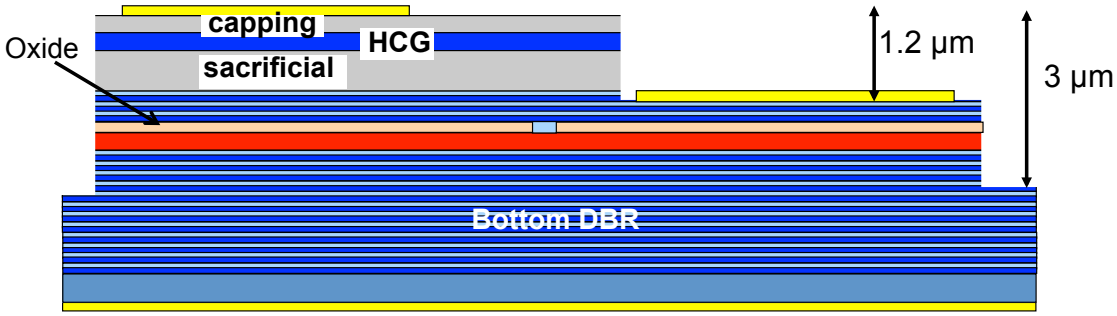
Oxide
capping
HCG
sacrificial
1.2 μm
3 μm
Bottom DBR

(c)

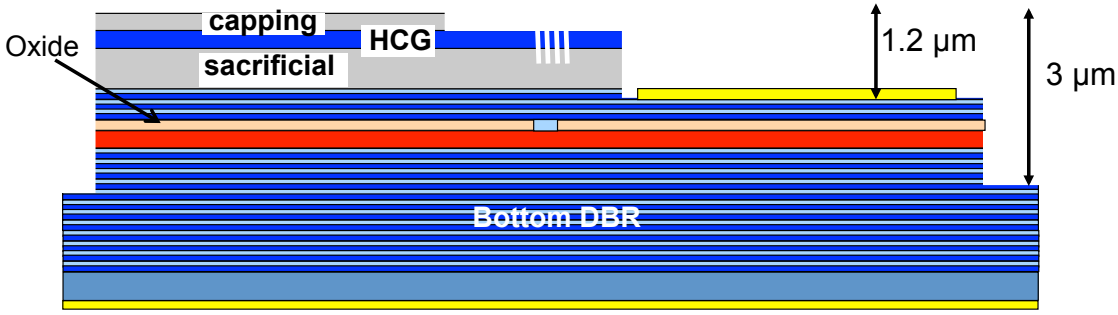
Oxide
capping
HCG
sacrificial
1.2 μm
3 μm
Bottom DBR

(d)

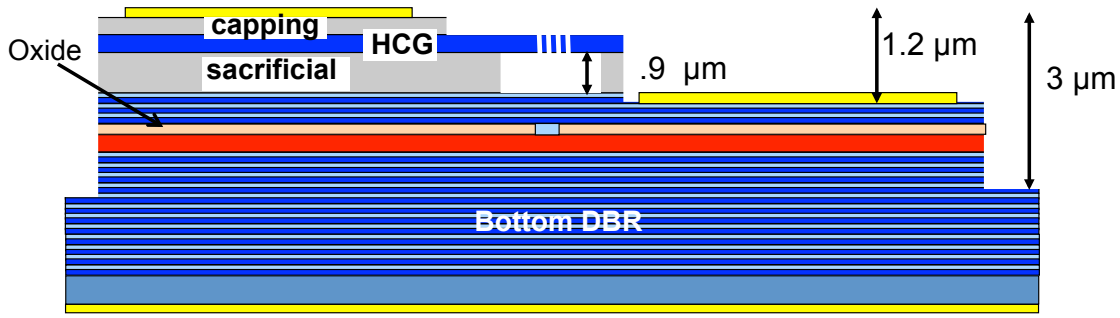

(e)

Figure 3.6 Schematic of the fabrication process for a HCG tunable VCSEL. a) The tuning contact is first deposited on top of the underlying epitaxial layers. b) A mesa is etched and an $Al_{0.98}Ga_{0.02}As$ layer in the structure is laterally oxidized except for the middle few microns to form a current aperture. c) Over part of the mesa, a selective etch down to the *p*-DBR below the sacrificial layer is performed with a subsequent metallization to obtain the *p*-side laser contact. A uniform metal layer is evaporated on the backside of the wafer to obtain the *n*-side contact. d) The HCG is patterned onto the structure using electron beam lithography, and the pattern is transferred into the HCG layer using a dry etch. e) The HCG is released using a selective etchant to etch away only the sacrificial material. This is followed by critical point drying to prevent pull-in of the HCG due to surface tension.

Figure 3.7 a) shows an SEM image of a completed device with the laser drive contact on the left, the high contrast grating on the VCSEL mesa in the center, and the tuning contact on the right. Figure 3.7 b) shows a zoomed in SEM image of the HCG in the center of a different completed device. The HCG can be seen in the center surrounded by actuators. The lighter-colored ring around the HCG seen in the image is the extent of the undercut of the sacrificial layer during the release etch.

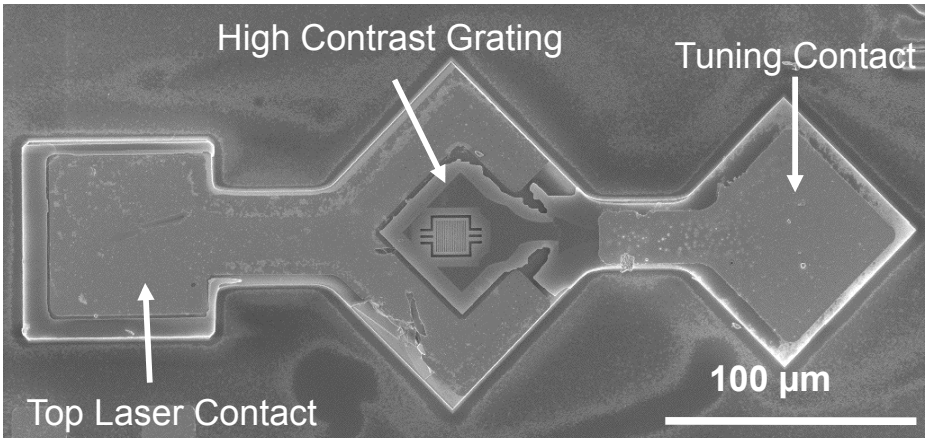

(a)

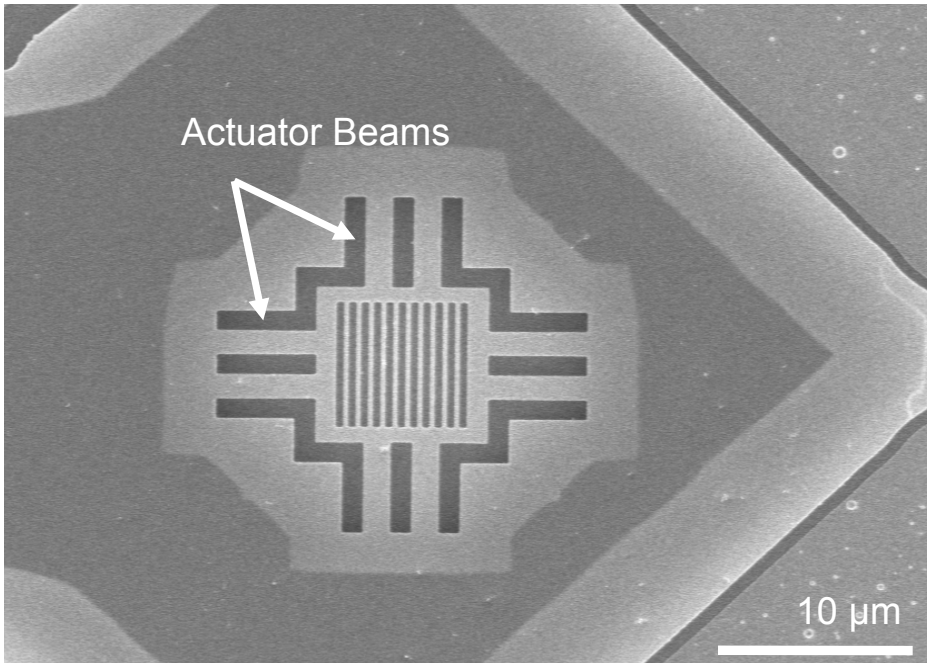

(b)

Figure 3.7 (a) Scanning electron microscope (SEM) image of a completed HCG tunable VCSEL. The top laser contact is on the left. A high contrast grating is in the middle of the laser mesa, and a tuning contact is on the right. (b) Zoomed in SEM image of the center of the mesa of another device, showing the HCG surrounded by actuator beams. The white ring surrounding the HCG indicates the extent of the undercut of the structure during the selective etch releasing the HCG.

3.3.5 VCSEL Electrical and Optical Characteristics

The tunable VCSEL devices with integrated TE-HCG show excellent optical characteristics. Devices have thresholds well below 1 mA, and slope efficiencies greater than 0.5 W/A, which are similar to conventional designs based on a top DBR as a mirror. The devices presented here

lase with only a single transverse mode. As the HCG mirror is designed to be highly reflective only for one orthogonal polarization, HCG VCSELs can lase in only one orthogonal polarization mode [11]. In the case of the TE-HCG, the electric field of the lasing mode is oriented parallel to the grating bars.

The light-current-voltage characteristic of a TE-HCG VCSEL is shown in Figure 3.8 a). The differential resistance of these VCSELs is relatively high because doping in the top *p*-DBRs has not been optimized. Figure 3.8 b) shows the spectrum of a different tunable TE-HCG VCSEL under various reverse bias voltages between the tuning contact and laser contact, and at a constant laser drive current of 3.5 mA. A continuous tuning range of ~6 nm is obtained with the TE-HCG VCSEL with single mode operation over nearly the entire range. This tuning range is the widest reported with a TE-HCG. This expanded tuning range is obtained using only 2 pairs of *p*-DBR instead. With more device structure optimization, this range should be expandable to greater than 15 nm as been shown with the TM-HCG VCSEL [52].

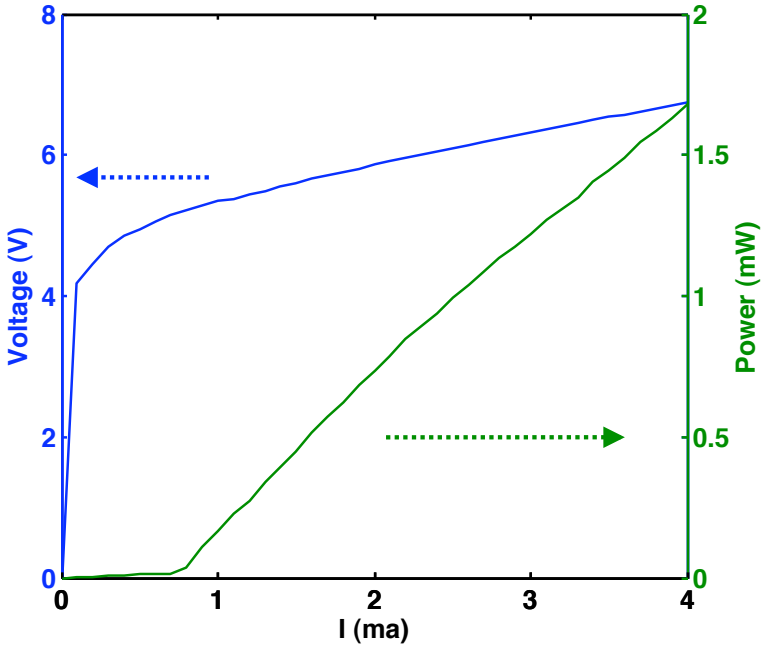

(a)

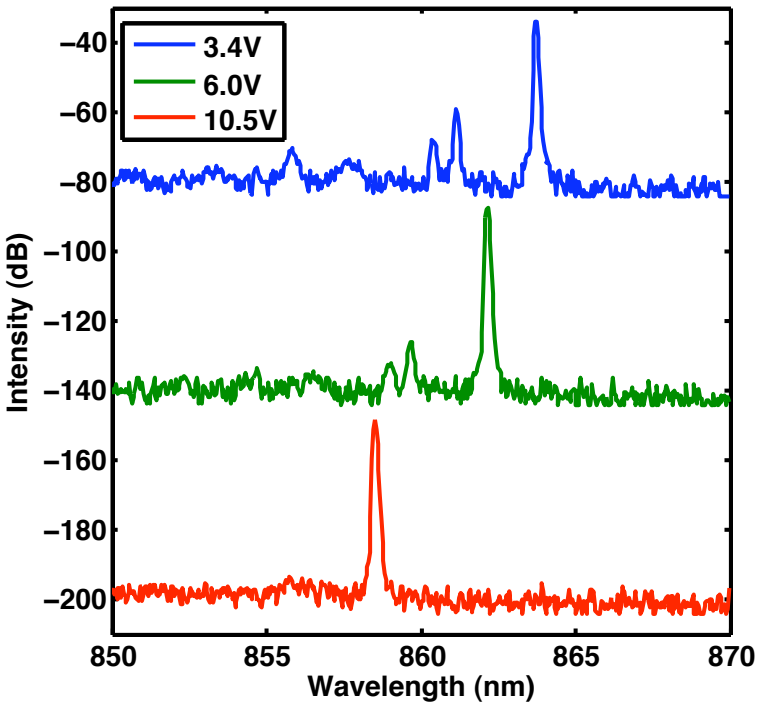

(b)

Figure 3.8 (a) Light-current-voltage characteristic of a TE-HCG tunable VCSEL under continuous wave, room temperature operation. (b) Spectrum of another TE-HCG tunable VCSEL at constant bias current of 3.5 mA with the tuning contact under reverse bias voltages (spectra offset by 60 dB for clarity) of 3.4, 6.0, and 10.5 V (blue, green, and red, respectively).

3.3.6 Laser Characteristics as a Function of Tuning Bias

The characteristics of a typical TE-HCG tunable VCSEL as a function of output wavelengths was tested to ascertain the uniformity of laser performance as a function of output wavelength. For this study, a TE-HCG tunable VCSEL with 4 pairs of top mirrors was used. The spectrum of this laser at several tuning voltages from 0 to 6 V when biased at a constant drive current of 1.5 mA under continuous wave room temperature operation is shown in Figure 3.9 a). Since this device has 4 pairs of top DBR, a reduced tuning range of 3.3 nm is achieved. Figure 3.9 b) shows a SEM image of the high contrast grating on the same device. The HCG used for this device was 12 X 12 μm^2 suspended in a bridge structure held up by two 5 µm long beams on either side.

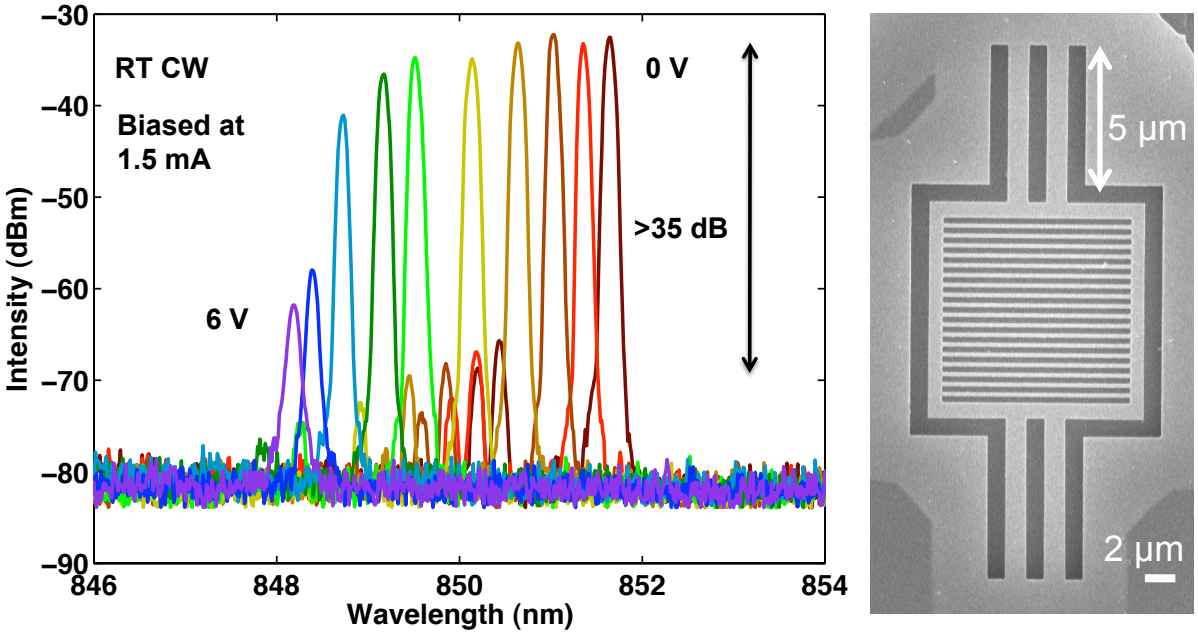

Figure 3.9 (a) Spectrum of a TE-HCG tunable VCSEL under various tuning bias voltages while the laser is biased at a fixed current of 1.5 mA under room temperature continuous wave operation. A tuning range of 3.3 nm was achieved. (b) SEM image of the HCG on the same device.

Various characteristics of a typical TE-HCG tunable VCSEL as a function of output wavelengths are shown in Figure 3.10. Figure 3.10 a) shows the output wavelength of the VCSEL as a function of tuning voltage. The wavelength shifts roughly quadratically with input voltage as the HCG's displacement. This matches well with theory, which predicts the displacement should go with voltage squared.

Figure 3.10 b) shows threshold current of the same tunable VCSEL as a function of output wavelength. At the blue end of the tuning range, the threshold current increases as the overall reflectivity from the top mirror decreases, as the reflection phase from the HCG and the VCSEL body to air gap goes out of phase with each other and destructively interfere.

Figure 3.10 c) shows the differential efficiency in W/A of the VCSEL as a function of output wavelength. As the wavelength becomes bluer, initially, the differential efficiency increases slightly as top mirror loss increases, but eventually plummets as the threshold current increases significantly, because the self-heating of the device at these higher threshold currents decreases device performance. The maximum differential efficiency is always near the threshold current.

Figure 3.10 d) shows the peak output power of the same VCSEL at a fixed drive current of 2.2 mA as a function of output wavelength. Again, as the wavelength gets bluer, the peak output falls as a result of the threshold increasing while the current where thermal rollover occurs stays approximately the same.

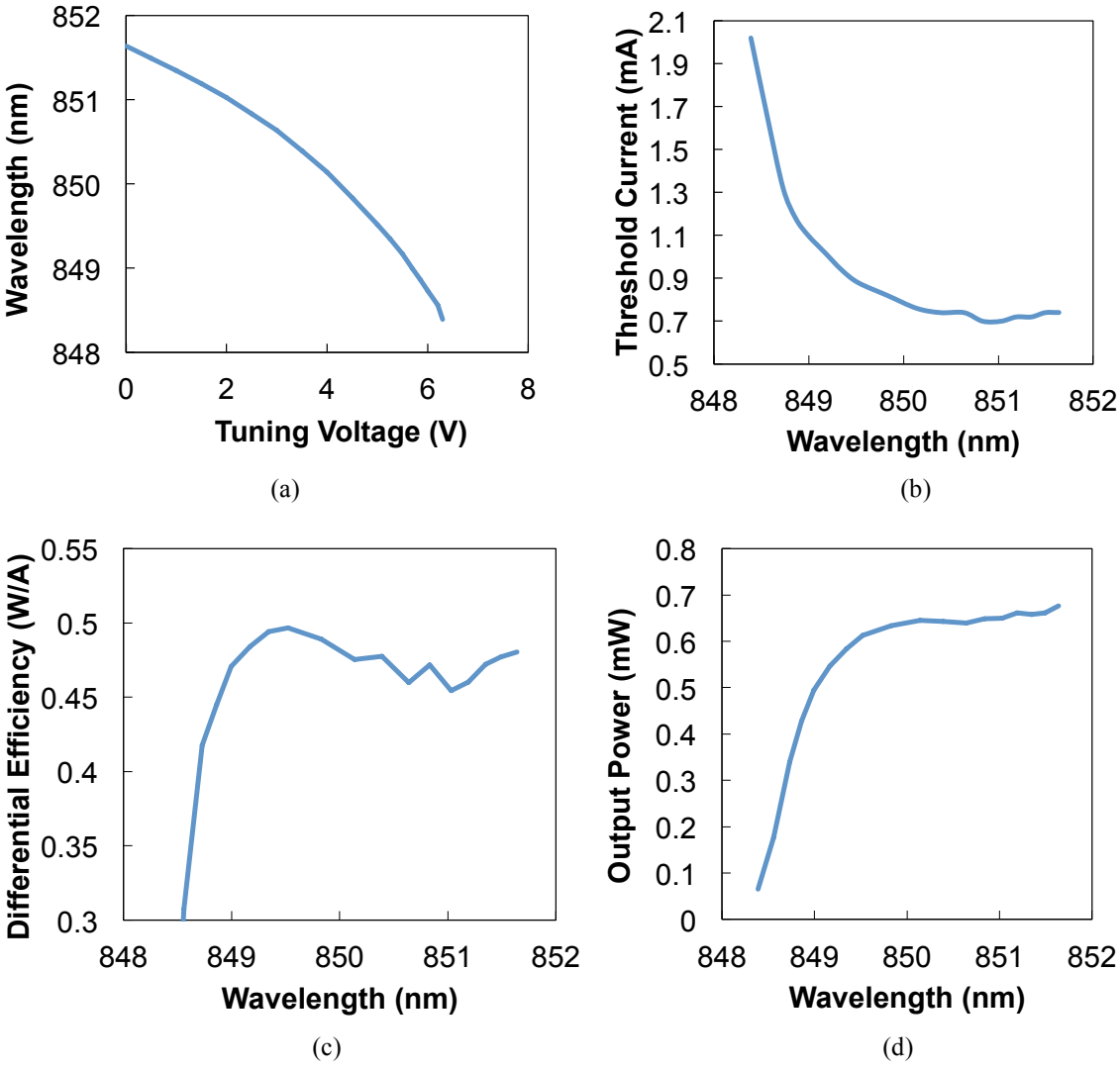

Figure 3.10 (a) Output wavelength of a TE-HCG tunable VCSEL as a function of tuning voltage. (b) Threshold current of the same tunable VCSEL as a function of output wavelength. (c) Differential efficiency in W/A of the same VCSEL as a function of output wavelength. (d) Peak output power of the same VCSEL at a fixed drive current of 2.2 mA as a function of output wavelength.

3.3.7 Blocking Junction Electrical Characteristics.

One major advantage of tunable VCSELs versus other tunable lasers is their low power consumption. Since the devices are actuated electrostatically, any power consumed during operation is due to leakage between the two contacts where the actuating voltage is applied. In the HCG VCSEL structure, current is blocked between the HCG MEMS structure and the rest of the VCSEL structure, which acts as the attracting plane, by a p-i-n junction.

The current-voltage (blue) and power-voltage (green) characteristics of the tuning p-i-n junction (as measured from the top laser contact to the tuning contact) are shown in Figure 3.11. Under reverse bias, this junction does not break down until greater than 35 V are applied to it. The typical regime of operation for HCG tunable VCSELs is less than 15 V of applied reverse bias, so under typical operation, on the order of a few hundred nanowatts are consumed, which is insignificant compared to the laser's power consumption which is on the order of 10 mW. This is in stark comparison to tunable sampled grating lasers or external cavity lasers, which typically have tuning power requirements alone of at least 10 mW.

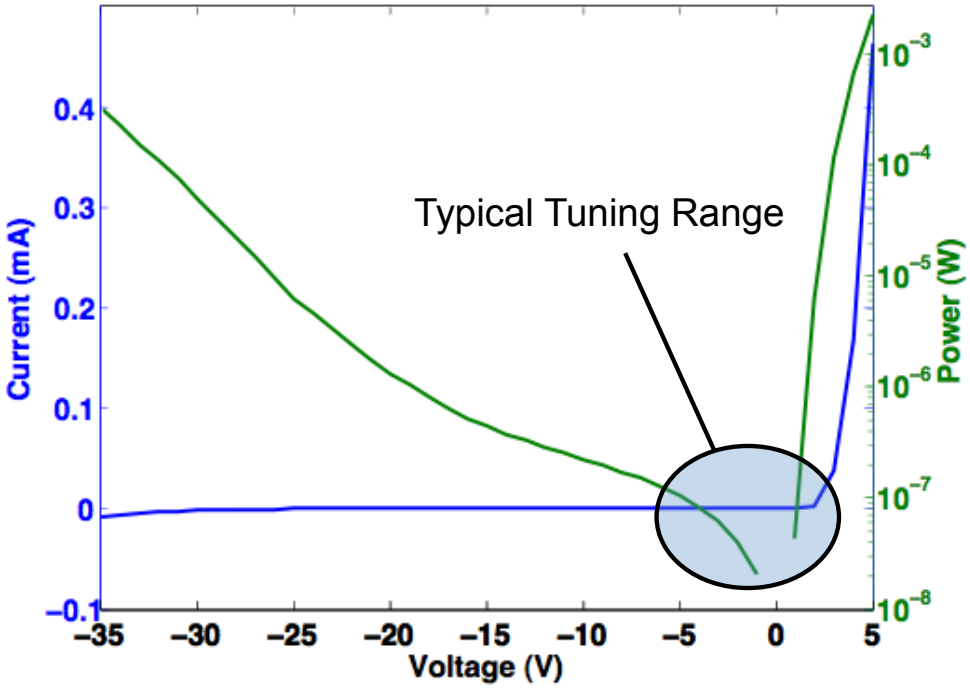

Figure 3.11 Experimental current-voltage (blue) and power-voltage (green) characteristics of the HCG tunable VCSELs. In the reverse bias regime, where the devices are typically operated, less than 1 μW of power is consumed by the tuning junction.

3.4 Mechanical Response

3.4.1 Frequency Response Measurement Method

The mechanical frequency response of the HCG was measured by biasing the VCSEL at a constant current through the laser contact and applying a DC voltage with a sinusoidal AC modulating voltage between the tuning contact and laser contact, actuating the mirror, as shown in Figure 3.12 a). The modulating voltage causes the spectrum of the device to broaden in an optical spectrum analyzer (OSA) as the laser is changing wavelength many times over the OSA's slow sampling time (~1 s/nm with ~500 sampling points per nm) as shown in Figure 3.12 b).

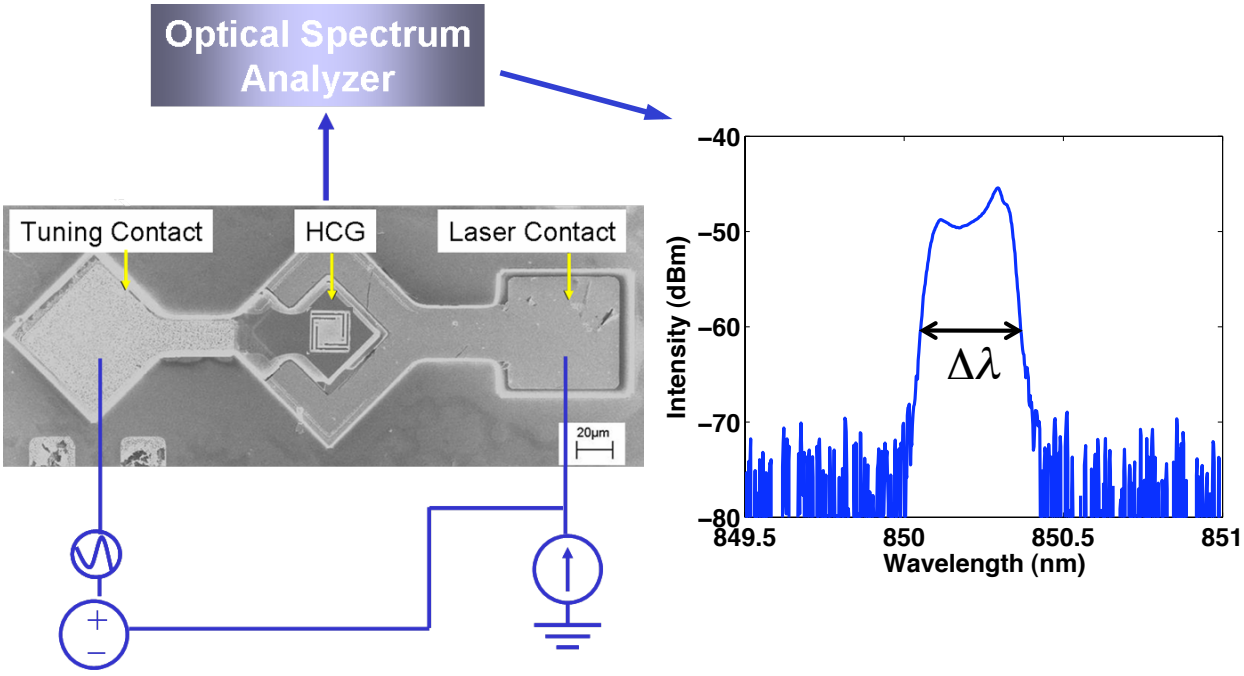

(a) (b)

Figure 3.12 a) To measure the mechanical response of the MEMS, the laser is driven at a constant bias current and a DC voltage plus a small signal variable frequency AC voltage is placed between the laser contact and tuning contact. b) The output is monitored on an OSA, which, due to its long integration time compared to the AC frequency, sees an average of the laser's output wavelength, which appears broadened due to the AC wavelength tuning. The amount of this broadening is used to ascertain the frequency response.

By measuring the width of the broadened spectrum and subtracting the unactuated width, a mechanical response can be ascertained. Figure 3.13 a) shows the normalized frequency response curve on the left with the corresponding spectrum at 20 kHz on the right side. Figure 3.13 b), c), d), and e) show corresponding spectrums for 1 MHz, 3.5 MHz, 5.2 MHz, and 6 MHz respectively.

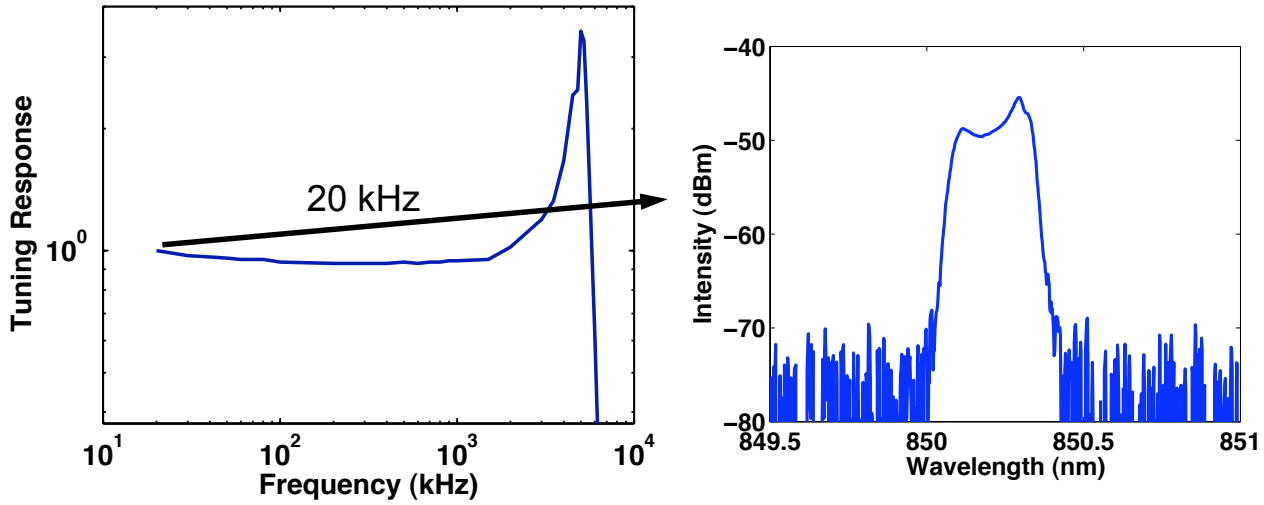
Tuning Response
10^0
20 kHz
10^1
10^2
10^3
10^4
Frequency (kHz)
Intensity (dBm)
−40
−50
−60
−70
−80
849.5
850
850.5
851
Wavelength (nm)

(a)

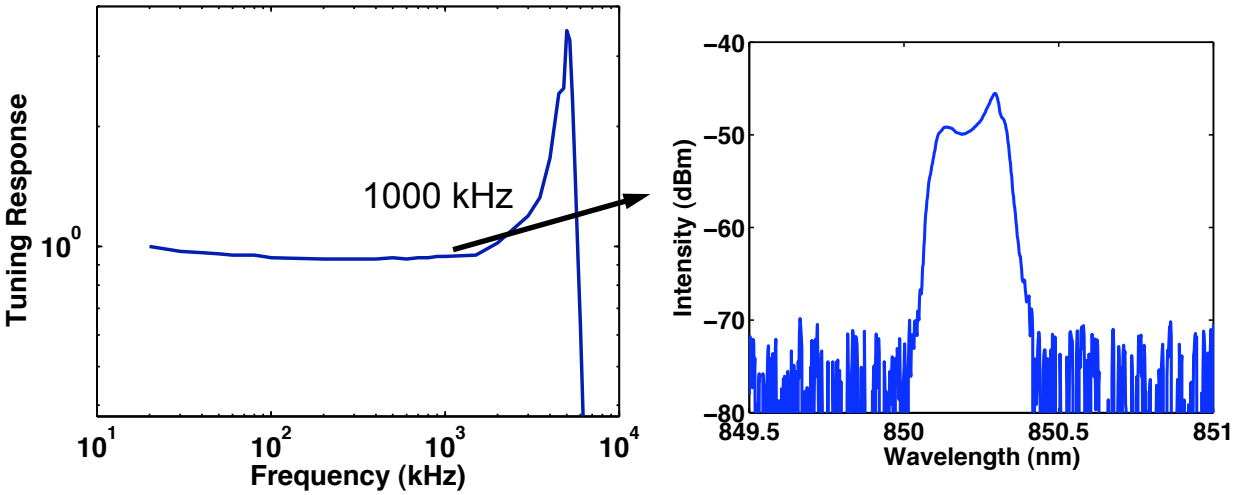
Tuning Response
10^0
1000 kHz
10^1
10^2
10^3
10^4
Frequency (kHz)
Intensity (dBm)
−40
−50
−60
−70
−80
849.5
850
850.5
851
Wavelength (nm)

(b)

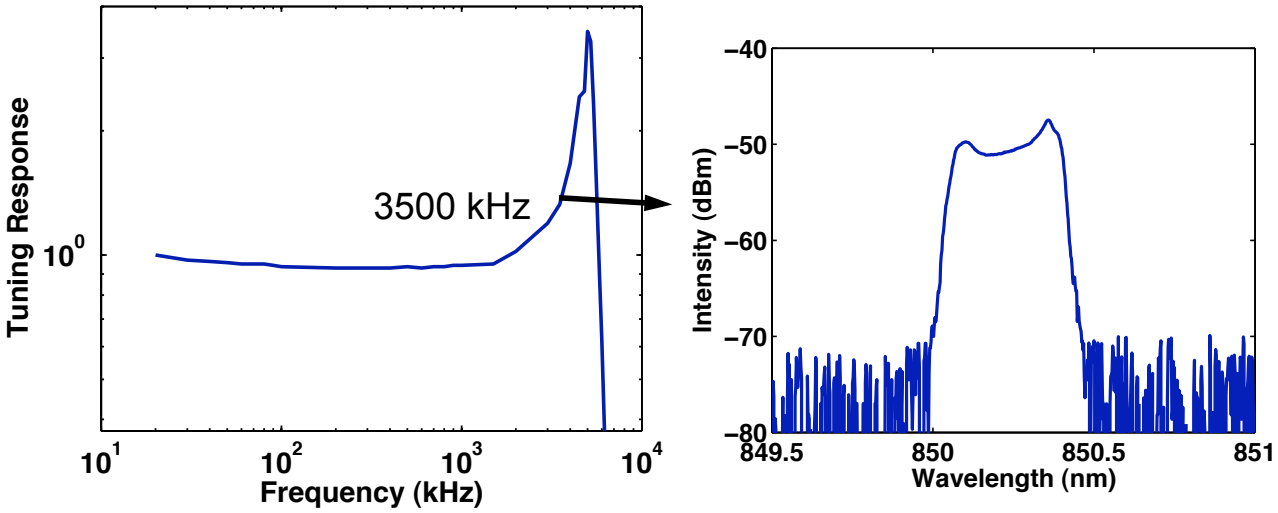
Tuning Response
10^0
3500 kHz
10^1
10^2
10^3
10^4
Frequency (kHz)
Intensity (dBm)
−40
−50
−60
−70
−80
849.5
850
850.5
851
Wavelength (nm)

(c)

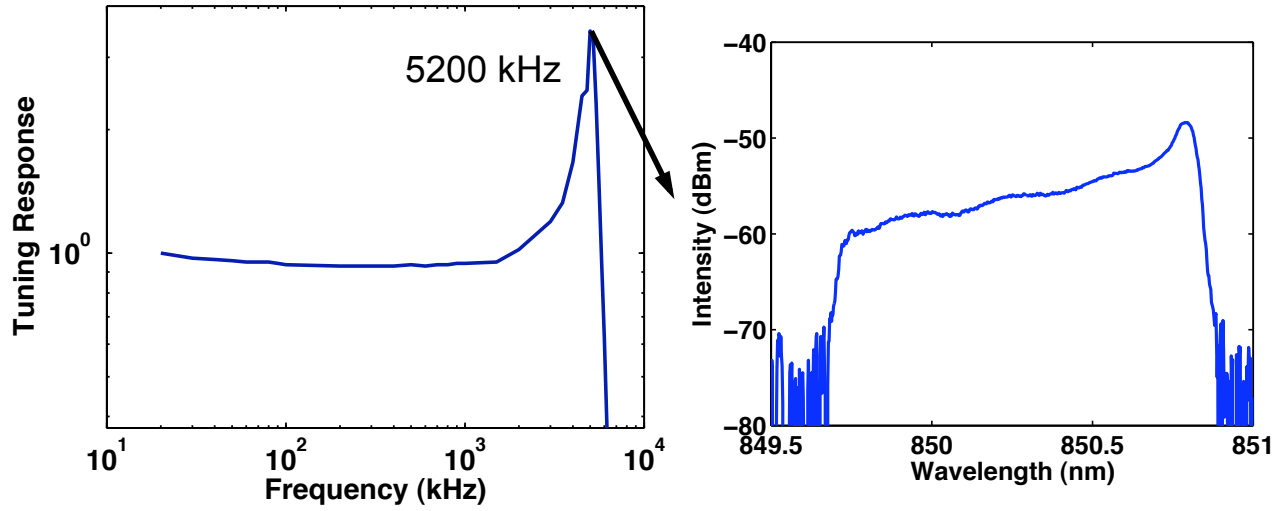
Tuning Response
10^0
5200 kHz
10^1
10^2
10^3
10^4
Frequency (kHz)
Intensity (dBm)
−40
−50
−60
−70
−80
849.5
850
850.5
851
Wavelength (nm)

(d)

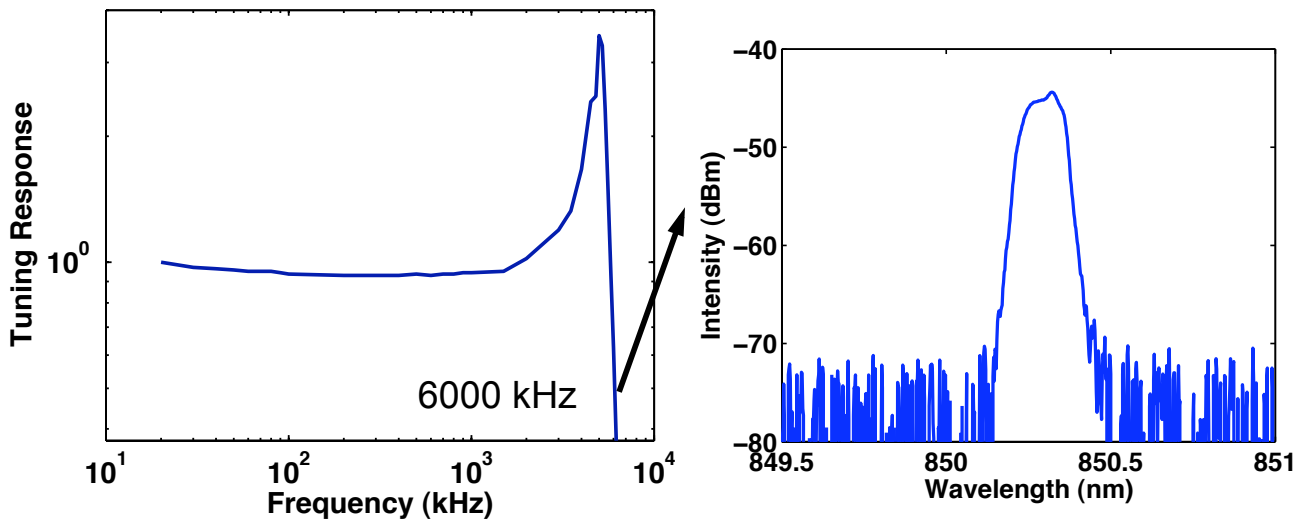

(e)

Figure 3.13 Example mechanical tuning response curves and corresponding spectrum as recorded by the optical spectrum analyzer. a) Example spectrum at 20 kHz AC modulation. b) Example spectrum at 1000 kHz AC modulation. c) Example spectrum at 3500 kHz AC modulation. d) Example spectrum at 5200 kHz AC modulation. e) Example spectrum at 6000 kHz AC modulation.

3.4.2 Frequency as a Function of Mirror Size

As was discussed in section 3.2, as we reduce the overall mass of the structure, we expect the mechanical frequency response of the MEMS structure to increase to higher frequencies. A series of devices were fabricated with identical VCSEL bases but with different size HCGs down to 4 μm. The actuators were all 3 μm long and with a width proportional to the dimension of the HCG, making the device comparable to a membrane. Indeed as the high contrast grating area was shrunk, an increase of the mechanical frequency response is seen, shown in Figure 3.14. Figure 3.14 a) shows the normalized wavelength broadening under modulation as a function of frequency for various HCG sizes. Figure 3.14 b) shows the extracted resonance and -3 dB frequencies. Devices with 4 μm x 4 μm HCGs had a resonance frequency of 5.3 MHz and a -3 dB frequency of 7.9 MHz.

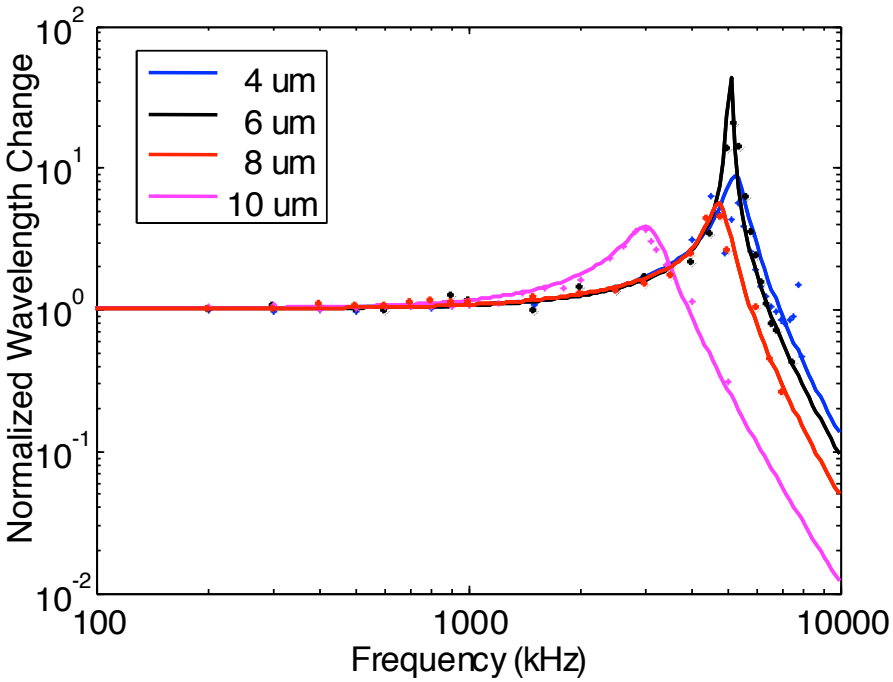

(a)

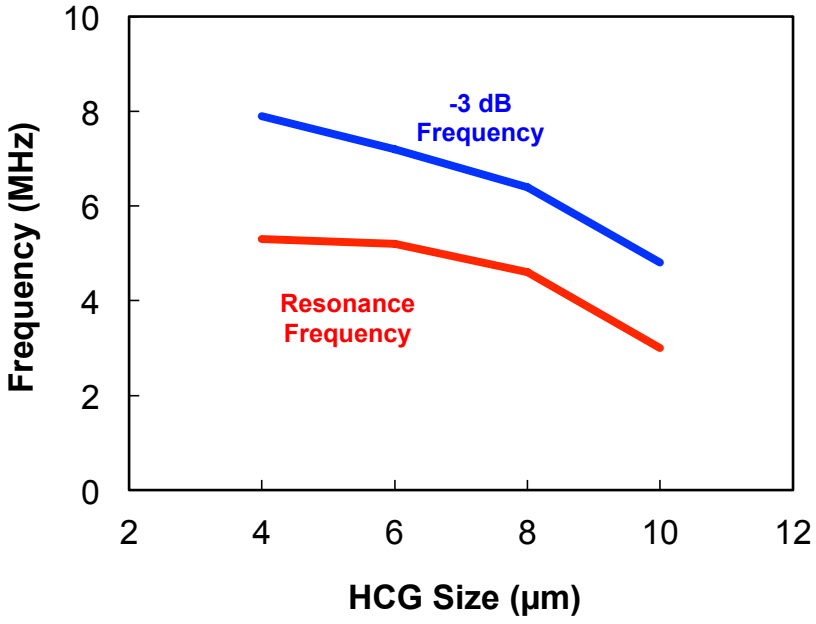

(b)

Figure 3.14 a) Normalized wavelength change as a function of input frequency to the tuning pad for various sizes of HCGs. Devices with different sizes of HCGs from 10 μm X 10 μm down to 4.1 μm X 4 μm are shown. b) Resonance and -3 dB frequency as a function of HCG size. The device with a 4 μm X 4 μm has a -3 dB frequency response of 7.9 MHz.

3.4.3 MEMS Analysis

In order to achieve as high as possible tuning speed, the structure was optimized to be as stiff as possible, while still being able to deflect the device by a measurable amount at high frequencies in our experimental setup. Limiting our measurement setup was the peak-to-peak voltage that we could achieve at frequencies greater than 10 MHz. The structure was stiffened by making the actuators as short as possible and making the actuators as wide as possible, almost fully surrounding the mirror itself. The actuators in the stiffest structures were only 3 μm long and nearly the length of the HCG itself, minus some small gaps so the actuators did not take too long to release.

The resonance frequency of the structure was estimated following standard beam equations [97] and assuming the mass of the beams was negligible. The result is shown in the green curve in Figure 3.15. Given the small size of the structure though, the mass of the beams is not actually negligible. The effective mass of the beams can be described by the equation:

$$m_{eff} = \frac{13}{35}\rho\, t_b\, w_b\, l_b \tag{3.7}$$

where ρ is the material density; t_b is the beam's thickness; w_b is the width of the beam; and l_b is the length of the beam. This expression is derived using the Rayleigh-Ritz method. The resonance frequency as a function of grating size and including the effective mass of the beam is shown in the blue curve in Figure 3.15. The resonance frequency is less at all sizes due to the added effective mass of the beams.

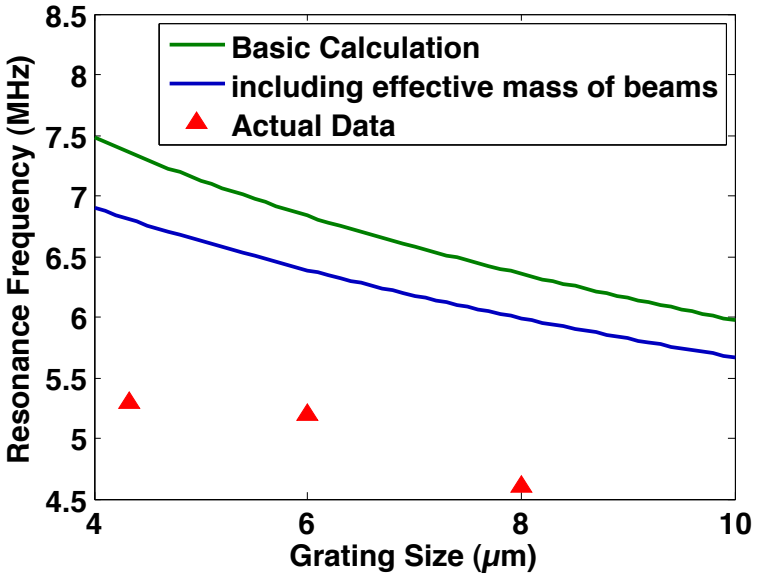

Figure 3.15 Resonance frequency of the mechanical structure as a function of grating size. The green curve shows the resonance frequency neglecting the effective mass of the beams; the blue includes the effective mass of the beams. Measured values are shown as red triangles.

The red points show the actual measured resonance frequencies. The actual resonance frequency is even less than the predicted values. This is likely due to the ends of the beams not

being totally fixed with respect to the rest of the structure. During the release, some undercutting occurs beneath the point where the beam is fixed to the rest of the structure. Thermal damping is another possible factor for the discrepancy between theory and measurement.

3.4.4 Frequency Response of the Smallest HCG

After optimization of alignment of the HCG to the aperture, an even smaller HCG of just 3.6 μm X 3.5 μm was realized. Figure 3.16 a) shows a tilted view SEM image of the smallest working HCG. Figure 3.16 b) shows a surface normal SEM image of the HCG.

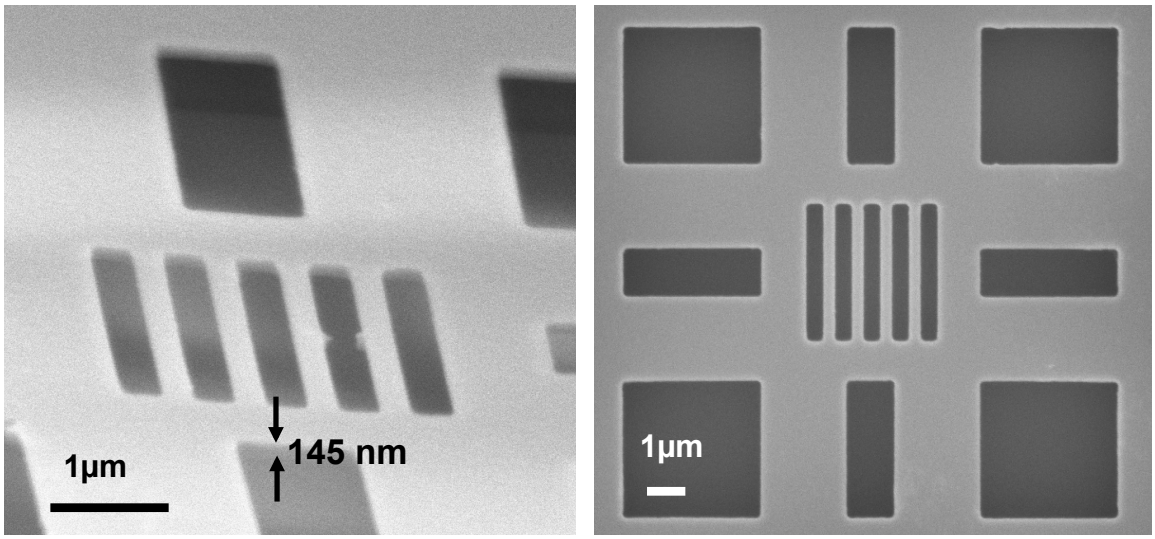

(a) (b)

Figure 3.16 SEM images of a 2.9 μm × 3 μm × 145 nm HCG, the smallest lasing HCG VCSEL (a) tilted view showing the 145 nm thickness of the TE-HCG (b) top view

The actuators on this smallest HCG device were made as stiff as they could be while still achieving a reasonable tuning range (~1 nm) with our available measurement setup, and also staying within reasonable reverse bias currents through the MEMS (less than 30 V and a few μA of current). For this design, the mechanical supports are 3 μm long and 2 μm wide. Two supports were connected to each of the 4 sides of the HCG mirror. The frame around the outside of the HCG is about 1 μm wide.

The spectrum of a device with a 3.6 μm HCG, with various AC modulation frequencies on the mechanical tuning contact is shown in Figure 3.17 a). The device is driven at a 1.4 mA laser bias current with a 22 V DC bias and a 10 V peak-to-peak AC signal between the laser contact and tuning contact to provide mechanical actuation. This device required higher tuning voltages than the device in Figure 3.9, because it's mechanical actuators were designed to be several times stiffer, requiring higher actuation voltages.

The tuning range of the device in Figure 3.17 is limited to less than 1 nm because a maximum voltage of approximately 40 V could be applied between the tuning contact and laser contact before the blocking junction between the two contacts breaks down. The full tuning range could be achieved at this tuning speed by modifying the structure so that more electrostatic

force can be applied; for example, by using aluminum oxide between the tuning and laser contact, or by optimizing the air gap to get the best tradeoff between electrostatic force and breakdown voltage.

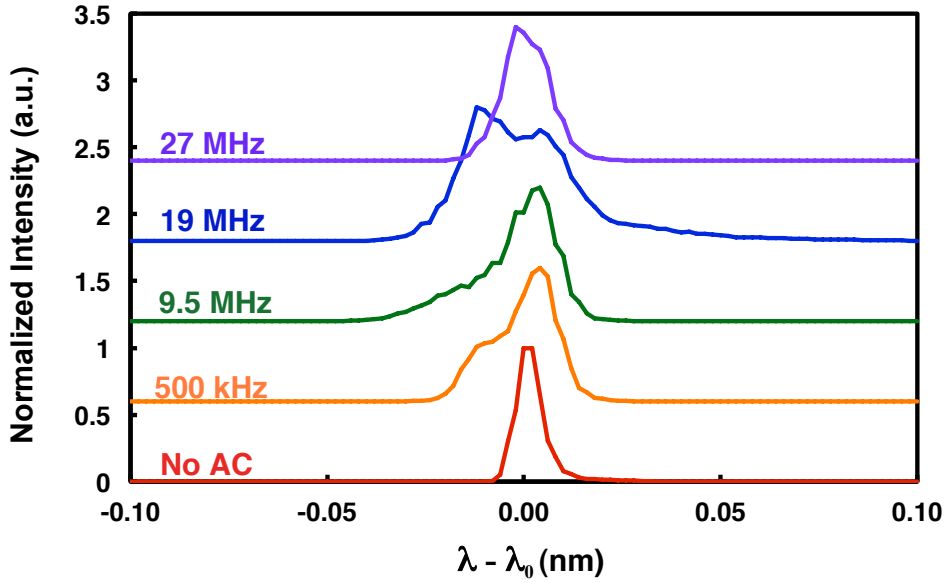

(a)

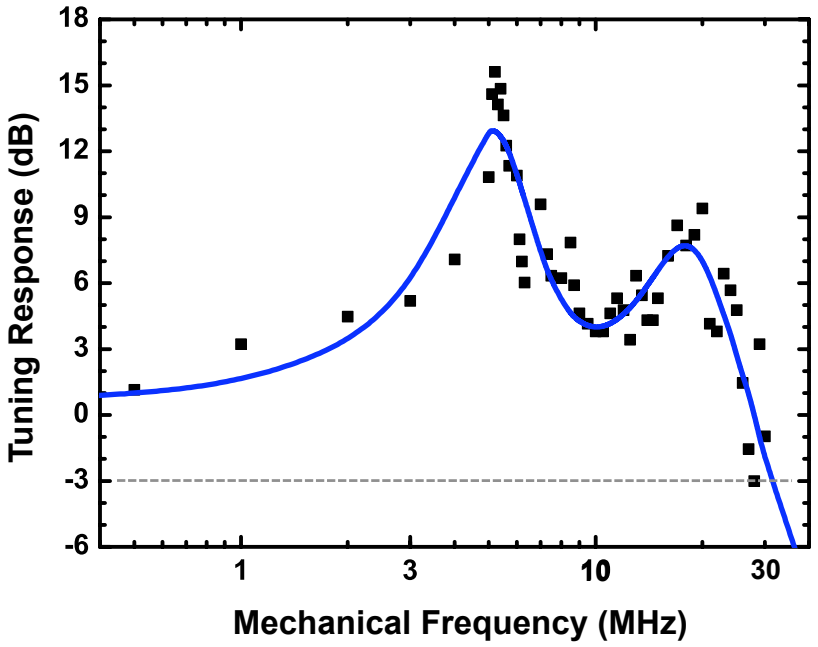

(b)

Figure 3.17 (a) Spectrum of a tunable VCSEL at constant bias of 1.4 mA with a mechanical tuning signal applied between the tuning contact and laser contact of a DC voltage plus an AC voltage at various frequencies. (b) The normalized relative optical wavelength change of the VCSEL, corresponding to the mechanical actuation of the HCG, as a function of input frequency to the tuning contact. The -3dB point in optical response occurs around 27 MHz.

Figure 3.17 b) shows the relative optical tuning response from the mechanical tuning at various input frequencies. The response has two peaks due to two relatively closely spaced mechanical resonances. Our measurement setup is limited to 30 MHz. This ultra small HCG shows optical response to AC tuning signals up to a -3 dB point of ~27 MHz, which is 5X higher than previously reported HCG tunable VCSELs [96].

3.5 Summary

The effects of the size of a HCG were studied when incorporated on a tunable VCSEL through simulation and experiment. The HCG size and actuator dimensions were optimized to achieve the fastest measurable tuning speed. With these compact HCGs, mechanical tuning response is seen up to a -3 dB point of ~27 MHz, 5X faster than previous reports. This increase of tuning speed may enable further applications of tunable VCSELs and other wavelength-tunable optoelectronic devices such as optical filters, sensors, and detectors.

Chapter 4 1325 nm Buried Tunnel Junction High Contrast Grating VCSEL

4.1 Motivation

Initially high contrast gratings (HCG) were implemented on 850 nm VCSELs [77], [100]. On 850 nm VCSELs, various advantageous features such as reduction in mirror size [77], polarization control [86], and higher order transverse mode control [71] were realized. For the data communications applications that these 850 nm VCSELs are commonly used for though, these features are not totally necessary, as the signal typically only travels only a few hundred meters, so dispersion is less of a consideration from a system point of view.

For distances of more than a few hundred meters, having a polarization stable single mode device becomes critical in order to achieve high-speed operation. Dispersion causes a modulated multimode laser signal to spread significantly, thus a device with a single polarization stable mode is necessary. In addition, at these distances, loss in the fiber causes attenuation of approximately 2 dB/km for an 850 nm signal [101]. Thus, the 1.32 and 1.55 μm bands become the wavelength bands of choice because of their much lower losses of 0.5 dB/km and 0.2 dB/km, respectively. 1.32 μm is particularly interesting because it is also the minimum of dispersion in optical fiber [101]. Thus for applications with distances less than 20 km where loss is not a dominant concern, 1.32 μm-based systems can provide the simplest, lowest cost option because that wavelength has the minimum dispersion and thus requires the fewest additional components to correct for dispersion.

Designing a VCSEL at 1.32 μm provides challenges not seen at 850 nm. On a GaAs substrate, it is difficult to achieve an active region at this wavelength. Some success has been achieved using GaInNAs [14], [102], but typically an InP-based structure is used [26], [103]. At 1.3 μm, an HCG mirror on a VCSEL would be extremely useful, because the small refractive index contrast available at that wavelength on the InP material system requires DBRs of on the order of 50 pairs, which can be over 10 μm thick. The removal of one of the epitaxial mirrors

from this structure results in a much thinner, more manageable epitaxy for 1.3 μm InP-based VCSELs.

From the perspective of high-speed modulation, there is further cause to remove the epitaxial mirror and replace it with a high contrast grating. Thick epitaxial DBR mirrors have a large photon penetration depth, which causes long photon lifetimes in the cavity, damping the high frequency optical response. Thus from a high-speed modulation point of view, it is important to remove all traditional epitaxial mirrors [20].

Though the HCG makes the epitaxial requirements of a VCSEL structure simpler, the initial GaAs-based HCG approach does make the fabrication process of the devices more complicated. In particular, it requires a sacrificial layer etch [77] to fully surround the HCG in a low index material. This sacrificial etch needs to have a high selectivity to the HCG layer, so that the HCG thickness can still be well controlled. The etch time also needs to be carefully designed so that the sacrificial layer is only partially etched away, as after the etch some areas of sacrificial material are still needed in some areas to provide mechanical support to the suspended high contrast grating.

The initially proposed HCGs [73] consisted of a Si HCG sitting on a low index SiO_2 layer, allaying the need for this sacrificial etch. This can also be achieved on a VCSEL structure by a deposition of a low index material and then a high index layer after the epitaxial growth of the rest of the structure.

In this chapter, we present the first 1.3 μm HCG VCSEL. The devices emit at 1320 nm and are based on an InP substrate. The top, out-coupling mirror consists of a lossy, amorphous high index silicon layer on a low index silicon dioxide material, with the HCG patterned on the silicon layer. No sacrificial layer etching is needed with this design, simplifying fabrication. Also, no epitaxial DBR layer pairs are used at all in this structure. This HCG approach greatly reduces the epitaxial requirements for InP-based VCSELs and uses a simplified approach for fabricating HCGs. Additionally, this is the first HCG VCSEL without any DBR layers aiding the top reflectivity of the HCG.

4.2 High Contrast Grating Design

4.2.1 Design of HCG on SiO_2 Spacer Layer

The Si high contrast grating on a SiO_2 spacer required a different design than had been previously used when the HCG was fully surrounded by air [77]. Compared to an HCG fully surrounded by air, a design with a SiO2 spacer needs to have its period slightly increased as well as the semiconductor duty cycle slightly decreased in order to still achieve the desired reflectivity and reflectivity bandwidth.

Both TE and TM designs were considered. The optimized TE HCG design had a period of 820 nm with an air gap of 640 nm. Figure 4.1 shows the simulated TE (solid blue) and TM (dashed red) reflection characteristics of the TE design. The simulation was performed using the RCWA method [92]. The reflection was simulated with a plane wave excitation from the InP (n = 3.17) substrate side through a 1020 nm SiO_2 low index (n = 1.44) layer and a 196 nm Si HCG layer (n = 3.55). In addition, a-Si is not perfectly lossless, so the simulation included a slight loss of $\alpha = 10\ cm^{-1}$ in this layer. This corresponded to the loss of a-Si measured on a sample wafer using the photothermal deflection method. The same a-Si was used for the device as described in section 4.4

The TE reflectivity in this design was over 99% over a more than 100 nm reflection bandwidth. The TM reflectivity on the other hand was between 10% and 20% across the same wavelength range. This large difference in reflectivity creates an extremely large difference in mirror loss between the two polarizations, so that the VCSEL emission should be pinned to the TE polarization.

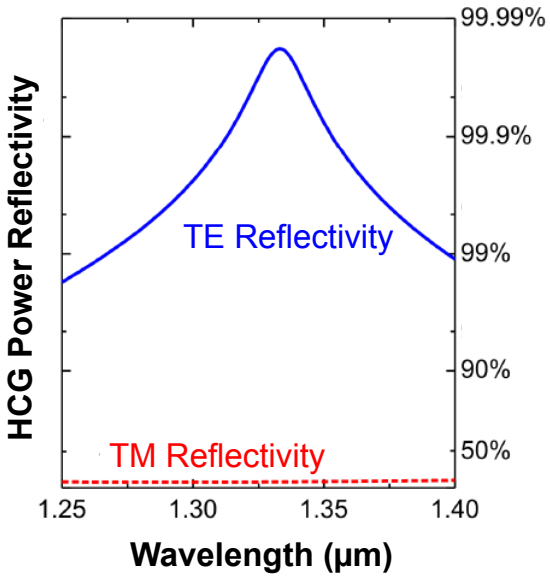

Figure 4.1 Simulated reflectivity of a TE HCG used for both TE and TM polarized light. TE reflectivity is above 99% over a 100 nm range while TM reflectivity is much less than 50% across the same wavelength range. For the simulation, the HCG period is 820 nm with an air gap of 640 nm. The grating is 196 nm thick with a 1020 nm SiO_2 region between it and the InP substrate.

For the evaluated TM design, the HCG parameters were a grating thickness of 362 nm (n = 3.55), a period of 565 nm, a semiconductor duty cycle of 75%, and a SiO_2 spacer (n = 1.445) thickness of 625 nm. RCWA simulation was again used as for the TE case. In the TM case, the reflectivity was even more broadband. At first glance, there was little difference in device performance whether the TE or TM design was chosen.

4.2.2 Effect of Loss on HCG performance

One major concern for this structure was the effect of the loss of the a-Si on the overall reflectivity of the HCG. Though the loss of the a-Si was measured on a dummy sample, we were not sure that the a-Si as deposited on the wafer would be the same. To study the effect of loss, a RCWA simulation was performed varying the loss in the a-Si layer for both optimized TE and TM a-Si on SiO_2 spacer designs. For the TM design, the parameters were a grating thickness of 362 nm (n = 3.55), a period of 565 nm, a semiconductor duty cycle of 75%, and a SiO_2 spacer (n = 1.445) thickness of 625 nm. For the TE design, the parameters were a period of 820 nm, a semiconductor duty cycle of 25%, a grating thickness of 196 nm, and a SiO_2 spacer thickness of

1020 nm. Both structures were sitting on an InP substrate (n = 3.17) with optical excitation incident from substrate side.

Figure 4.2 shows the reflectivity as a function of loss, with TE in red and TM in blue. Both designs are relatively unaffected by losses up to 10 cm^{-1}. The TE provides reasonable reflectivities even with losses up to 100 cm^{-1}. The better performance of the TE design can be attributed to its much smaller volume of a-Si per unit area. The TE design only has 20% as much volume a-Si as the TM design per unit area.

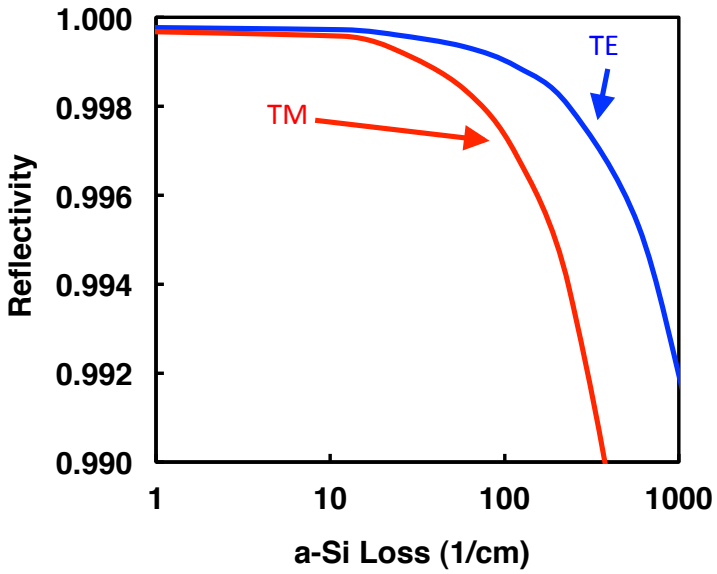

Figure 4.2 Simulated reflectivity of the HCG as a function of loss in the a-Si layer for both optimized TM (red) and TE (blue) designs. The TM design is more sensitive to loss, presumably because it has much more Si volume than the TE design per unit of mirror area. The TE design can tolerate losses greater than 100 cm^{-1}, while still providing reasonable overall reflectivities.

4.2.3 Fabrication Tolerance of Si HCG on SiO_2 Spacer

Additionally, the fabrication tolerance of the Si HCG on SiO_2 spacer layer was studied by RCWA. The simulation structure consisted of a launched TE-polarized wave from a InP substrate traveling through the 1020 nm SiO_2 spacer layer and 196 nm a-Si HCG layer. The period and air gap of the HCG layer were swept and the reflectivity recorded. Figure 4.3 shows the power reflectivity of the HCG layer as a function of the HCG air gap and period. The light blue X denotes the dimensions used in Figure 4.1. The black dotted line denotes 99.5% reflectivity, which is approximately the minimum needed for the VCSEL to lase. For this design, the sensitivity to period is approximately ±20 nm and air gap approximately ±50 nm, similar to the design completely suspended in air (see section 2.8).

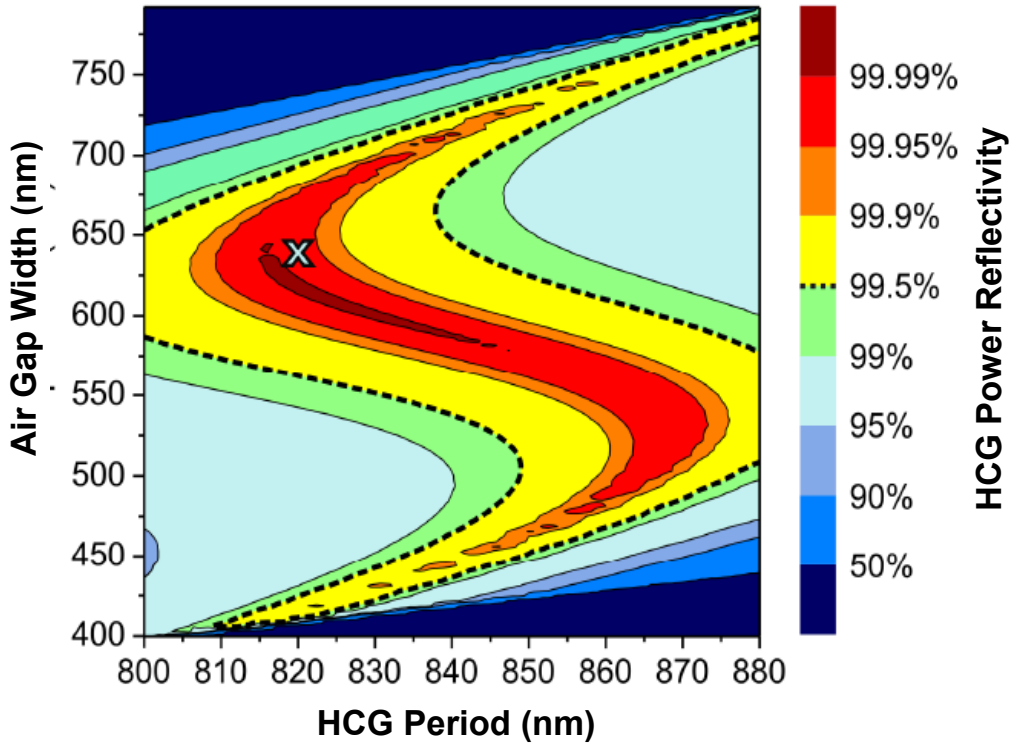

Figure 4.3 HCG power reflectivity as a function of HCG air gap width and period. The HCG design is quite tolerant to dimension imperfections in the fabricated HCG. The dotted line shows the 99.5% reflectivity region, which is approximately the minimum reflectivity required for the VCSEL to lase. The light blue X shows the dimensions used in Figure 4.1.

4.3 VCSEL Design

The long wavelength HCG VCSEL is based on the high-speed long-wavelength VCSEL structures with a short cavity and record modulation bandwidth [20] pioneered by the group of Prof. M. C. Amann at the Technical University of Munich. A schematic of the VCSEL structure is shown in Figure 4.4. A buried tunnel junction (BTJ), whose dimensions are lithographically controlled, serves as the current aperture. Since a BTJ is used, most of the relatively optically lossy and electrically resistive *p*-material is replaced by *n*-material. An InP cladding layer is used on both the *n*- and the *p*-side of the device, serving mutually as a current and a heat spreader. The active region for these devices was designed to emit at 1320 nm.

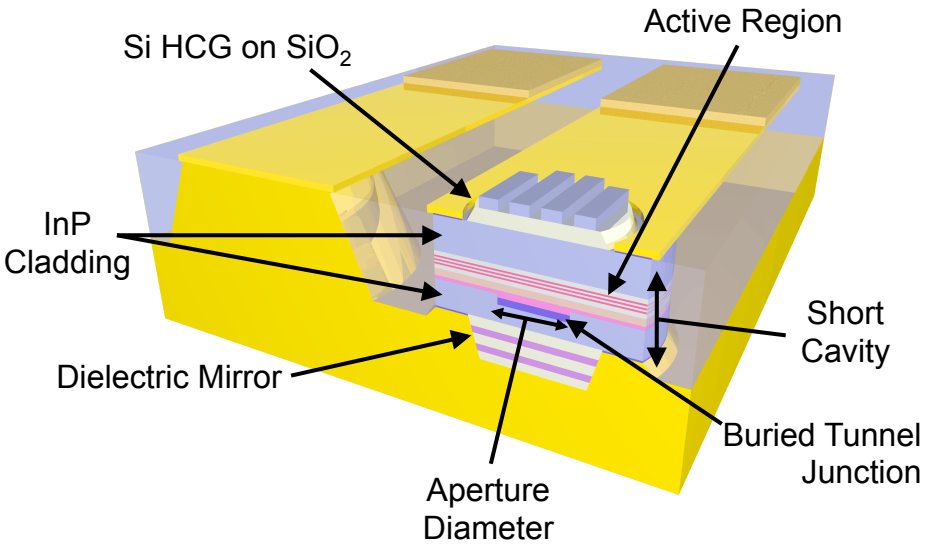

Figure 4.4 Schematic cross section of the 1.32 μm HCG VCSEL.

The base structure for these devices was grown by molecular beam epitaxy (MBE). Compared to 1.55 μm devices, the aluminum content in the GaAlInAs BTJ layers must be raised to avoid direct band gap absorption at 1.3 μm. As a consequence of the high Al content, the regrowth over the BTJ was performed by metal-organic chemical vapor deposition (MOCVD) with which the higher aluminum content material can be more easily regrown. For comparison to the HCG VCSEL, a VCSEL structure similar to that in [104] was fabricated using a dielectric mirror consisting of 5 pairs of AlF_3 and ZnS instead of the HCG. Benzocyclobutene (BCB) was used as low dielectric constant passivation layer, reducing the capacitance between the pads and the substrate. With the dielectric mirror, however, polarization mode stability is not guaranteed due to the lack of a polarization anisotropy. In addition, higher order transverse modes are not as strongly suppressed, as they would be with an HCG (see section 2.5 for further discussion).

The amorphous layers making up the Si HCG and SiO_2 spacer layer were deposited by e-beam evaporation. Their thickness was controlled by in-situ white light reflectometry. The grating was defined by electron beam lithography and transferred into the a-Si HCG layer using SF_6-based dry etching. Though electron beam lithography was used here, the dimensions are also suitable for conventional DUV lithography.

Scanning electron microscope images of the fabricated HCG are shown in Figure 4.5. Figure 4.5 a) shows a SEM image of the completed device. Figure 4.5 b) shows a zoomed in SEM image of the HCG bars. Roughness of the sidewalls on the order of 30 nm was seen as a result of the amorphous nature of the Si. Though the simulated mirror reflectivity is well above 99.9%, a reasonable out-coupling power is expected due to fabrication imperfections such as this sidewall roughness.

The HCGs were fabricated with the bars oriented along the [011]-axis of a (100)-InP-wafer, i.e. perpendicular to the large flat. This design was for high reflectivity for transverse electric (TE) polarized light (as discussed in section 4.2). The a-Si thickness was measured to be 196 nm. The SiO_2 spacer layer was measured to be about 1020 nm. The fabricated grating periodicity was around 820 nm. The Si bar widths were approximately 200 nm.

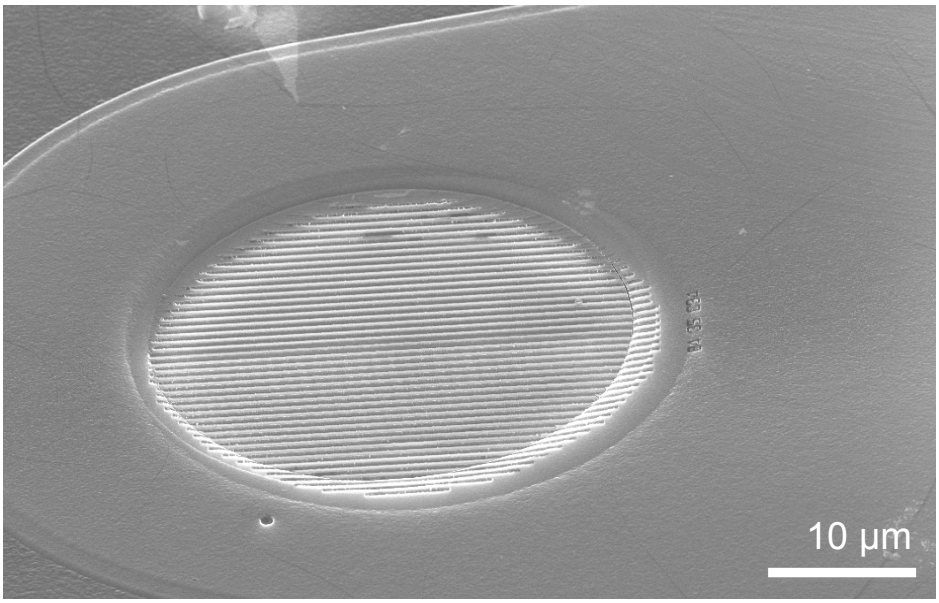

(a)

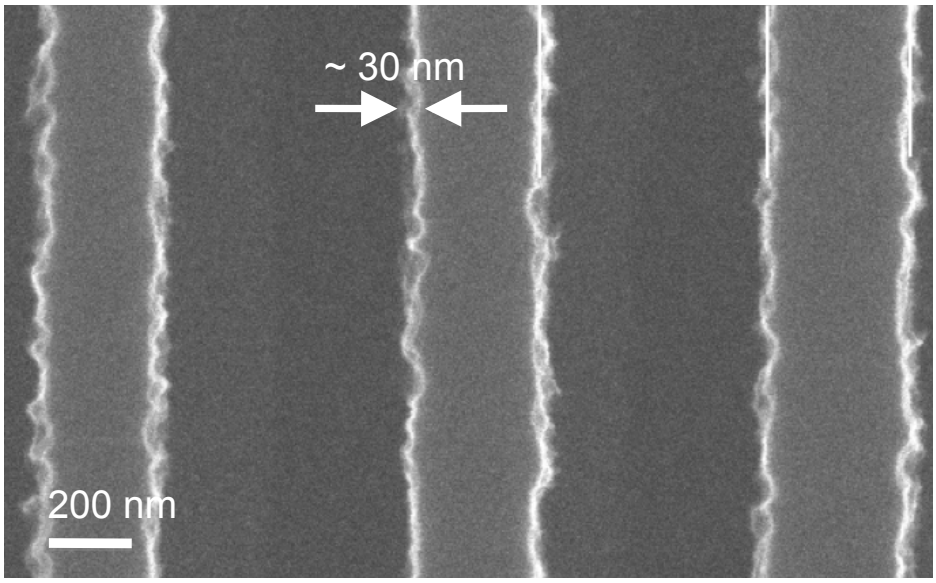

(b)

Figure 4.5 a) SEM image of a completed HCG VCSEL device. b) Zoomed in image of the individual HCG bars. Some sidewall roughness on the order of 30 nm was seen due to the amorphous nature of the Si.

4.4 Device Performance

4.4.1 CW Light-Current and Spectral Characteristics

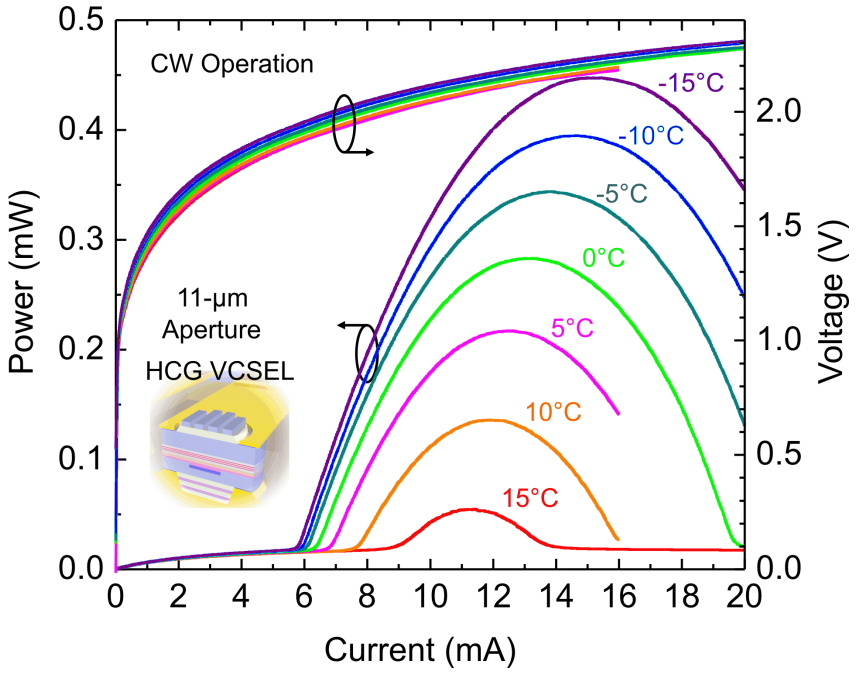

Figure 4.6 Light-current-voltage characteristics of a 1325 nm HCG VCSEL with an 11 μm aperture under continuous wave operation at various heat seat temperatures from -15º C up to 15º C.

The light-current-voltage (LIV) characteristics of a 1325 nm HCG VCSEL with an 11 μm BTJ aperture is shown in Figure 4.6. The device operates under continuous wave excitation at temperatures up to 15º C. The maximum power achieved is ~0.45 mW with a threshold current of less than 6 mA, achieved at -15ºC. The devices tend to have their minimum threshold around -30º C, indicating that the active region was not detuned optimally. Figure 4.7 shows the spectrum of the same device under CW excitation at -15º C under various bias currents. The devices emit around 1320 nm and are single mode under all biases. A tuning coefficient is 0.3 nm/mA is exhibited. These devices were the first experimentally demonstrated electrically pumped continuous wave InP-based VCSELs using a high contrast grating.

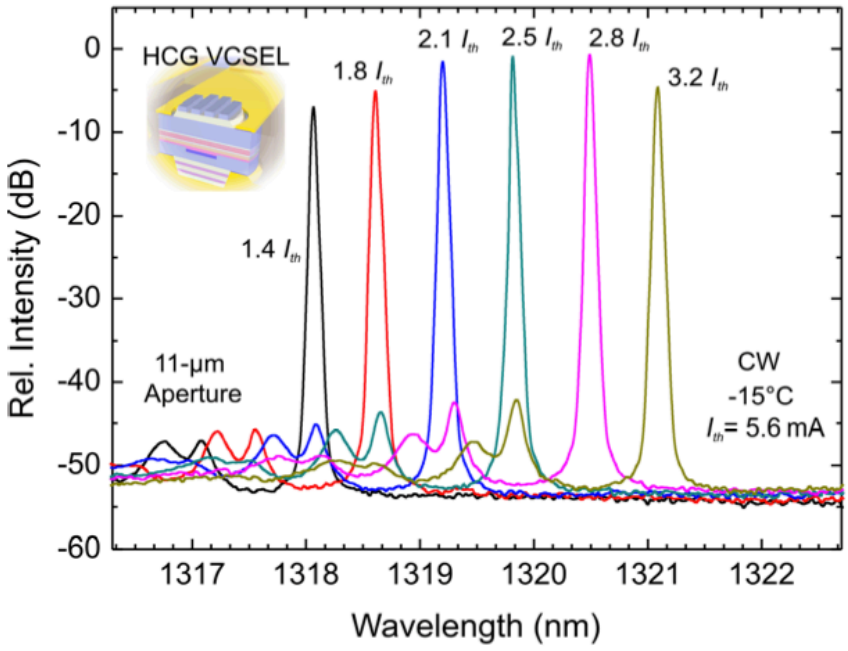

(b)

Figure 4.7 Spectrum of a 1325 nm HCG VCSEL at various bias currents under continuous wave operation at -15º C. A tuning coefficient of 0.3 nm/mA is obtained.

4.4.1 Aperture Dependent Light-Current and Spectral Characteristics

Under pulsed operation of 200 ns pulses, which were 0.1% duty cycle, the devices operated up to 60º C. Figure 4.8 a) shows the light-current characteristics of the HCG VCSELs at different aperture (BTJ) sizes from 11 up to 25 μm under pulsed operation at 20º C. A maximum output power of 4 mW was seen with a 17 μm aperture. The lowest threshold current was achieved with the 11 μm aperture. Figure 4.8 b) shows the same 17 μm aperture device from part a) under pulsed operation at various heat sink temperatures. The device lases under pulsed operation at up to 60 º C.

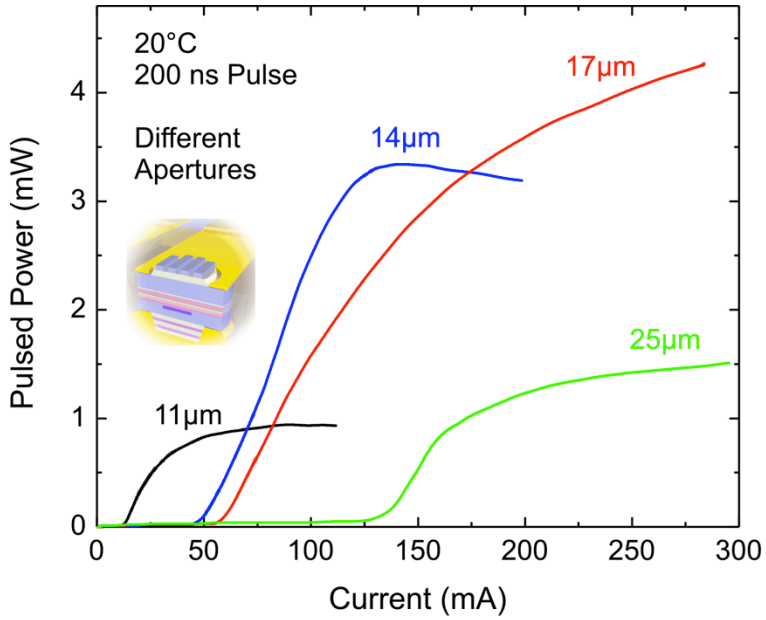

(a)

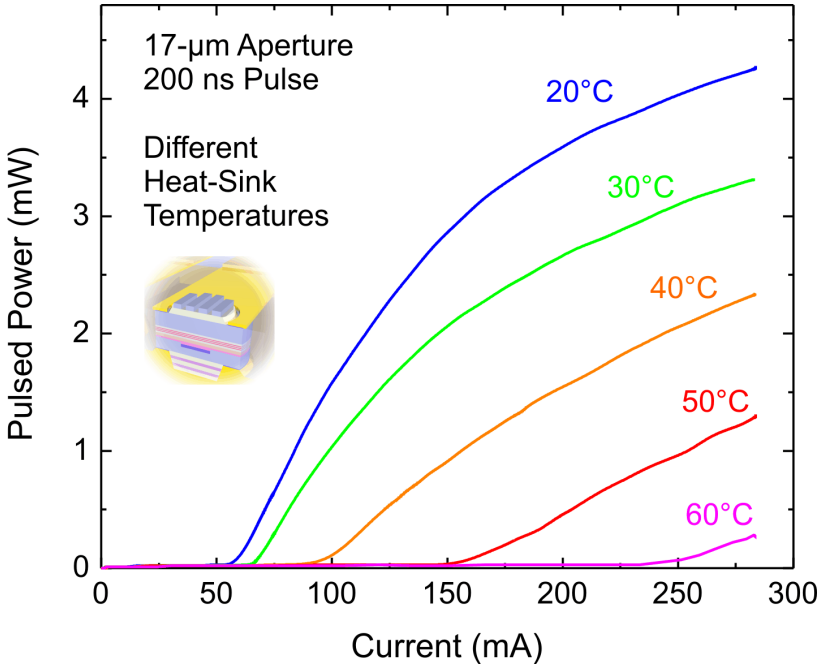

(b)

Figure 4.8 a) Light-current characteristics of the 1320 nm HCG VCSELs at different aperture (BTJ) sizes under pulsed operation at 20º C. A maximum output power of 4 mW was seen with a 17 μm aperture. b) The same 17 μm aperture device from a) under pulsed operation at various heat sink temperatures from 20º C up to 60º C.

Figure 4.9 shows the spectral characteristics of the same devices from Figure 4.8. All devices are under pulsed operation with 200 ns pulses and a 0.1% duty cycle. The spectrum was taken by butt-coupling a multimode fiber close to the VCSEL aperture to collect all emission from the device. Figure 4.9 a) shows the pulsed spectra at a 20º C heat sink temperature for various BTJ aperture sizes from 11 µm up to 25 µm at a constant current density of 50 kA/cm^2 for all devices. Despite the relatively large aperture sizes, devices with up to 17 µm BTJ apertures show single mode characteristics with >20 dB side mode suppression ratios. Figure 4.9 b) shows the spectrum of the 11 µm aperture device at various heat sink temperatures. The device lases up to 60º C. A tuning coefficient of 0.06 nm/K was obtained with a constant current density at all temperatures.

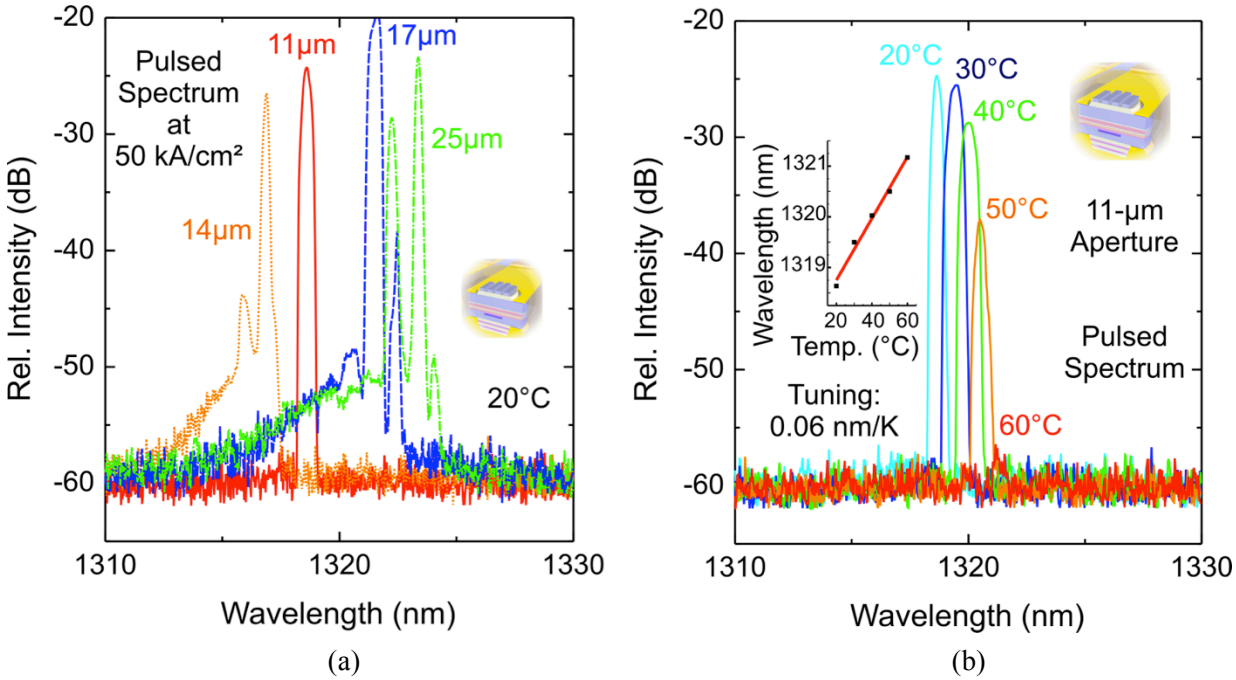

Figure 4.9 1320 nm HCG VCSELs under pulsed operation. a) VCSELs with various aperture sizes up to 25 µm at a constant current density at 20º C. Devices remain single mode with aperture sizes of 11 µm up to 17 µm. b) Spectra of the 11 µm device at various heat sink temperatures up to 60 º C. A tuning coefficient of 0.06 nm/K can be extracted.

4.4.2 Transverse Mode Characteristics

In order to compare the HCG to a DBR, a set of identical VCSELs were fabricated with a dielectric DBR top mirror instead of a HCG. These DBR VCSELs were fabricated from the same wafer as the HCG VCSELs. The wafer was split into several pieces at the point of fabricating the top mirror, which was the last process step. The HCG VCSELs were expected to show much larger single mode aperture devices as discussed in section 2.5.

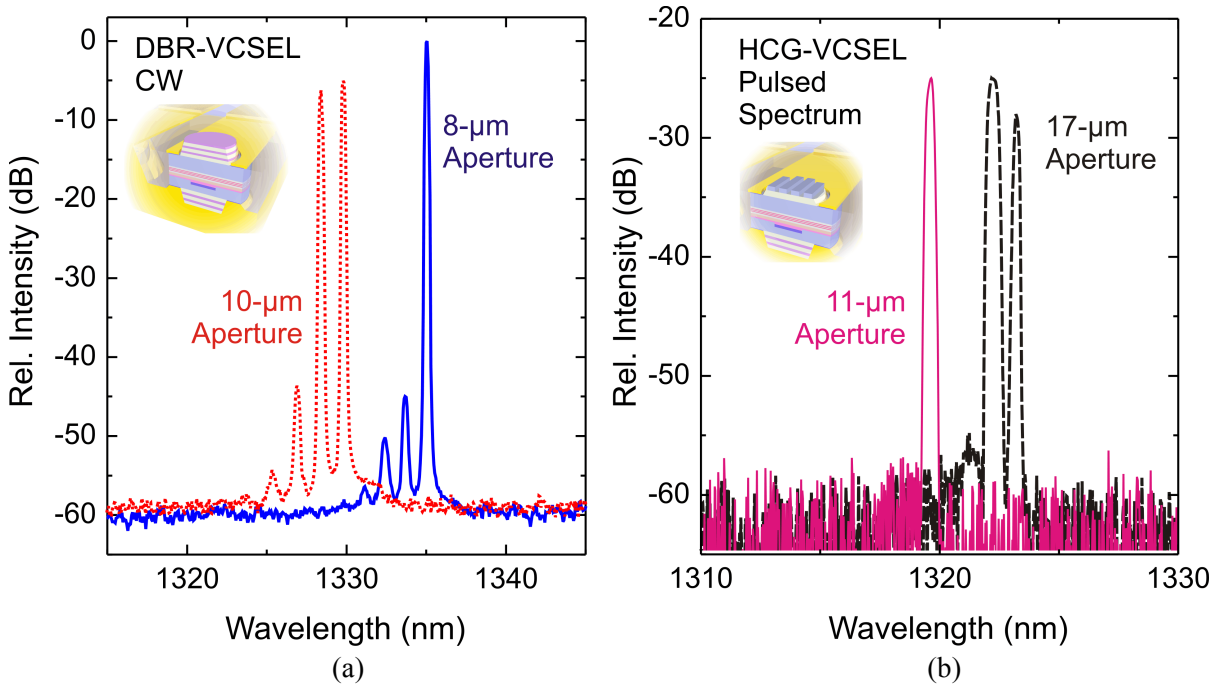

Figure 4.10 Comparison of spectra of both a 1325 nm DBR-based VCSEL and a HCG-VCSEL at different buried tunnel junction aperture sizes. a) CW spectrum from DBR-based VCSELs with identical structure to the HCG VCSELs reported here except for the top mirror. DBR VCSELs with an 8 μm aperture are single mode, while 10 μm aperture devices are not. b) Pulsed spectrum from HCG VCSELs. HCG VCSELs with 11 μm apertures are single mode while devices with 17 μm apertures are not. Note that the HCG VCSEL spectra are also taken at over twice the current density of the DBR VCSELs.

Figure 4.10 shows of spectra of both a 1325 nm DBR-based VCSEL a) and an HCG-VCSEL b) with different BTJ aperture sizes. The DBR-based VCSELs are driven under continuous wave operation, while the HCG VCSELs with an identical structure except for the top mirror, are driven under pulsed operation. The DBR VCSEL with an 8 μm aperture is single mode, while the device with a 10 μm aperture is not. For the HCG VCSELs, the 11 μm aperture HCG VCSELs are single mode while 17 μm devices are not. Unfortunately, no HCG VCSELs with aperture sizes in between 11 and 17 μm lased due to fabrication problems, so the demarcation between the single mode and multi mode regime was not entirely certain. It should be noted that the HCG VCSEL spectra are also taken at over twice the current density of the DBR VCSELs, a regime where they would be even more likely to be multimode than a comparable DBR VCSEL. Figure 4.11 shows the side mode suppression ratio versus the BTJ aperture diameter for both DBR and TE HCG VCSELs. Clearly, switching the DBR for an HCG increases the aperture size that yields single mode devices by approximately 4 μm.

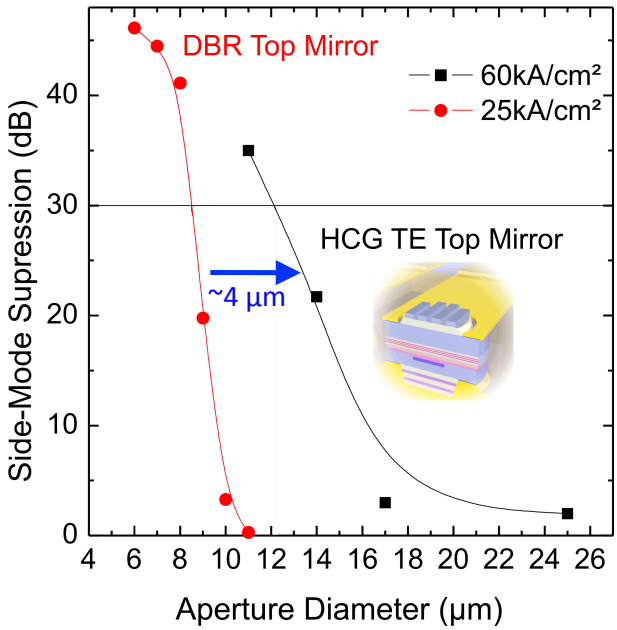

Figure 4.11 Side mode suppression ratio versus buried tunnel junction aperture diameter for DBR and TE HCG VCSELs. Switching an HCG for a DBR increases the aperture size that yields single mode devices by approximately 4 µm.

4.5 Performance Discussion

Unfortunately, device performance from this design was not as good as was anticipated. We expected to achieve room temperature CW devices with higher single mode output powers and higher modulation speed than comparable DBR-based devices.

This was not achieved for several reasons. Devices from the same process run with DBRs did perform somewhat better, but they were not nearly as good as expected. Problems through the fabrication process caused yield to be low in both the HCG and DBR VCSELs. In addition, the DBR VCSELs had much higher threshold currents than expected of approximately 3 mA, when less than 1 mA was expected. This high threshold meant lower output powers than would otherwise be expected as well as lower modulation speeds than expected. The most likely cause for this was that the buried tunnel junction was not placed exactly at an antinode in the VCSEL cavity, leading to high optical losses in the cavity, as losses rise exponentially as the BTJ drifts from the antinode. The growth run for these VCSELs had used a novel growth method. After the definition of the BTJ, overgrowth was performed using MOCVD instead of MBE, as had been done previously. As this was a novel process, the overgrowth thickness may have been slightly off, causing the BTJ to be away from the antinode in the full structure.

Another difference between the HCG and DBR versions of the VCSEL was the emission wavelength. The DBR VCSELs lased around 1335-1340 nm while the HCG VCSELs lased around 1315-1320 nm. Given the active region was the same, this meant that the cavity detuning and active region gain was significantly different between the two designs. The active region had been designed for best performance at 1340 nm, thus the superior performance of the DBR-based devices. By cooling the HCG VCSELs, we saw much better performance, as the gain was

more optimally aligned as the device was cooled. The lowest laser thresholds were seen at around -30º C in the HCG VCSEL devices. This offset was due to the silicon dioxide spacer layer being slightly too short, making the cavity too short overall.

The last and perhaps strongest reason for the sub-optimal performance was the a-Si itself. As the a-Si is evaporated by electron beam evaporation, it is highly susceptible to contaminants, which can be incorporated into the evaporated material. Later analysis showed that the a-Si as deposited on these structures may have had an index of refraction as low as 2.8 due to impurity incorporation during evaporation.

The HCG design itself is a strong function of refractive index as shown in Figure 4.12. This simulation is calculated using RCWA with a fixed HCG design: a period of 820 nm, a semiconductor duty cycle of 25%, a grating thickness of 196 nm, and a SiO_2 spacer (n=1.445) thickness of 1020 nm sitting on an InP substrate (n = 3.17) with TE excitation incident from substrate side. As the index changes from the design value of a-Si, n = 3.55, the high reflectivity bandwidth decreases. Additionally, the peak of the reflectivity band blue-shifts with a lower refractive index. In this case, if the refractive index of the a-Si HCG was less than ~3.3, the HCG would not provide enough reflectivity for the VCSEL to lase CW.

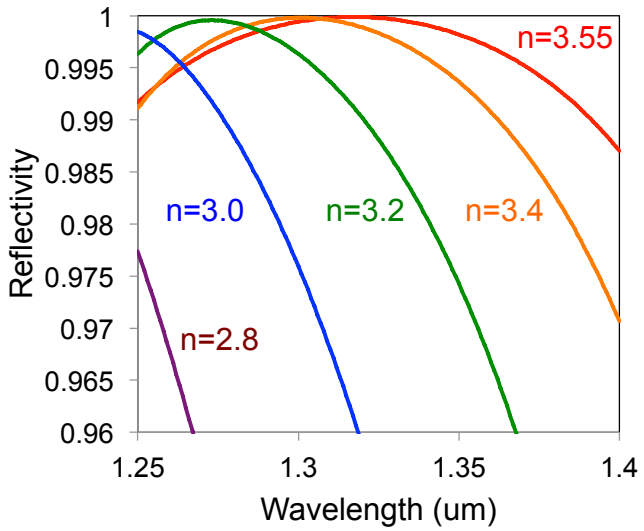

Figure 4.12 Reflectivity of a fixed HCG design as the index of refraction of the HCG layer varies. As the index decreases, the high reflectivity bandwidth shrinks and the peak of the high reflectivity band blue-shifts.

Despite all these problems, the 1325 nm HCG VCSEL nonetheless lased, indicating that with further optimization to the process and structure, a high performance, high-speed room temperature continuous wave device should be achievable. We expect performance in excess of the DBR-based short cavity designs previously shown [20], [104].

4.6 Summary

In this chapter, we showed the first electrically pumped InP-based high contrast grating VCSELs emitting at 1325 nm. These VCSELs are promising as low cost devices for mid-distance optical communications systems. Devices were demonstrated with a peak CW emission

of 0.4 mW at cooled temperatures. Peak powers exceeding 4 mW were achieved under pulsed operation at room temperature. Device performance was not as strong as expected due to some fabrication-related difficulties. With more optimization to the fabrication process and structure, higher performance devices are expected.

The devices are the first HCG VCSELs to operate with a non-crystalline, slightly lossy HCG layer deposited by evaporation. We have shown that this approach has a high potential to achieve a simply fabricated HCG without the need for a suspended structure or release process. Additionally, we have demonstrated the first HCG VCSEL without any DBRs in the top mirror aiding the reflectivity of the top HCG. With this approach, larger aperture, higher power, single mode VCSELs with higher modulation speeds are expected to be realized.

Chapter 5 InP-based Proton Implant HCG VCSEL

5.1 Motivation

Long wavelength VCSELs are promising as a low cost laser source for metro area access networks [38], high speed optical interconnects, and diode laser spectroscopy [39]. Many potential applications for VCSELs in next generation access networks and passive optical networks (PONs) require the VCSELs to operate at 1.55 μm, and the InP material system is the widespread choice for a 1.55 μm active region. InP-based VCSELs have traditionally been more challenging to realize when compared to GaAs-based short wavelength VCSELs because of several additional technical challenges posed by the InP material system, the most difficult of which are the top mirror and current aperture.

As discussed in section 1.3, there have been several approaches that have been demonstrated to solve these issues. All of these solutions though have required added cost and complexity to the VCSEL manufacturing process. To date, long wavelength InP-based VCSELs have not made a major impact on the market. Designing an InP-based device structure that can be produced for as low of a cost as GaAs VCSELs has remained a problem.

The integration of a high contrast grating, which also allows the use of a proton-implant-defined aperture [105], offers an approach that can potentially reach a price point on the order of GaAs-based VCSELs. High contrast gratings are an extremely interesting alternative mirror on an InP-based VCSEL as they can totally negate the need for one or potentially both of the DBRs. These DBRs create major difficulties in both epitaxial growth and device performance. Additionally many of the other features of HCGs such as intrinsic polarization control, larger area single transverse optical modes, and high speed wavelength tuning are also advantageous for long wavelength VCSELs.

The grating also enables an easy solution to the problem of forming a current aperture in InP-based VCSELs. Proton implantation is a well-known technique for creating current apertures in a VCSEL structure [105] with high reliability [106]. Unfortunately, it has some limits as to what

depths it can be used to achieve blocking in a structure. Typical proton implantation systems can reach accelerating voltages of up to 400 keV, which limits maximum depths at which it can be used in a structure to approximately 4 µm from the surface. This excludes its use in an InP structure with a thick layer above the active region, as the proton implantation depth should be just above the active region for best performance. With the HCG as a top mirror, there is no concern as there is only about 3 µm of epitaxial material between the active region and the surface. Proton implantation is a much easier technique to implement than the commonly used buried tunnel junction on InP [11].

In this chapter we will explore the application of an HCG to a 1.55 µm InP-based VCSEL. The design, fabrication, and experimental results of the first HCG VCSEL on an InP platform operating continuous wave at room temperature are shown. Due to a great reduction in epitaxial layer thickness above the active region, we can use the simple technique of proton implantation to form a current aperture in the VCSEL, negating the need for the complications of regrowth needed to create a buried tunnel junction. This novel design, hence, enables only one epitaxy step and simple fabrication, features that are necessary to manufacture high yield, low cost, long wavelength VCSELs.

5.2 HCG VCSEL Design and Fabrication

5.2.1 VCSEL Design

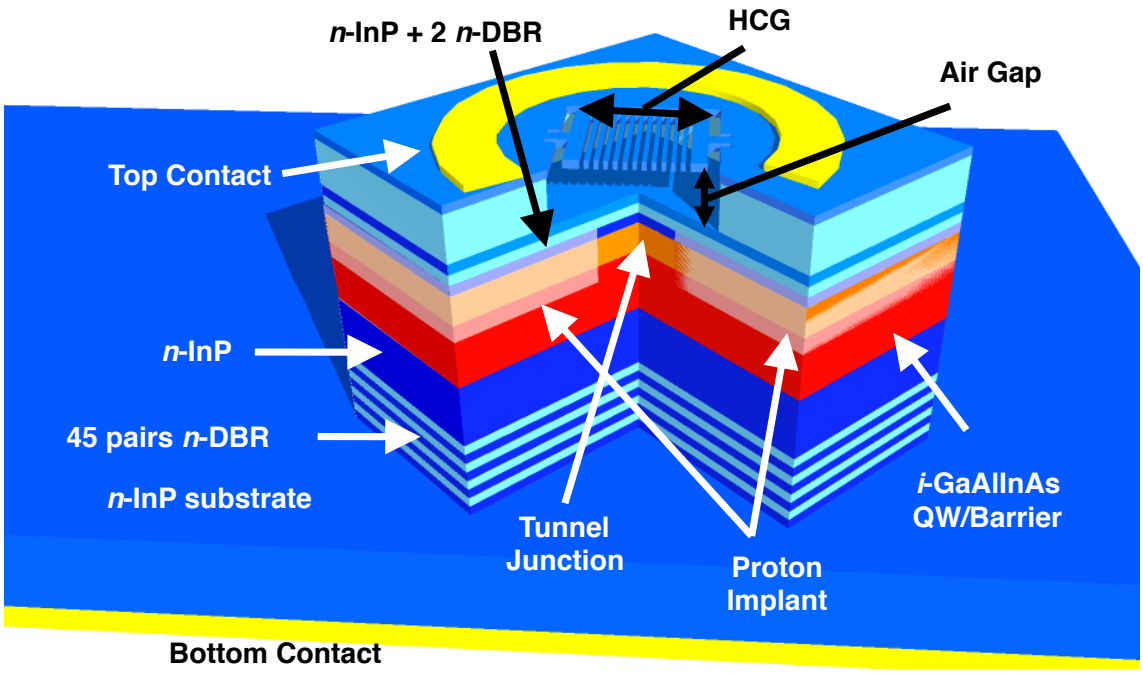

Figure 5.1 Schematic of a 1550 nm VCSEL with a suspended TE-HCG. Current confinement is provided by a proton-implant-defined aperture.

A cross section of the device is shown schematically in Figure 5.1. It consists of, starting from the substrate side, 45 pairs of *n*-DBR of InP/GaAlInAs, chosen because it has the highest thermal conductance [51] of all of the available material choices in the GaAlInAs/InGaAsP/InP

system. Above the DBR pairs is an InP heat sink layer, an active region with six GaAlInAs quantum wells, and a thin layer of *p*-GaAlInAs, followed by a tunnel junction. Above the tunnel junction there are two pairs of *n*-DBR, followed by a ~1.8 μm air gap and a 195 nm thick InP high contrast grating. The grating is ~12 X 12 μm^2 wide in all cases described here. Electrical confinement is provided in the structure by a proton implantation at a depth near the tunnel junction. The size of the proton implant aperture is varied from 8 to 25 μm. Contacts are deposited on the backside of the wafer and topside on a contact layer above the HCG layer and surrounding the etched HCG.

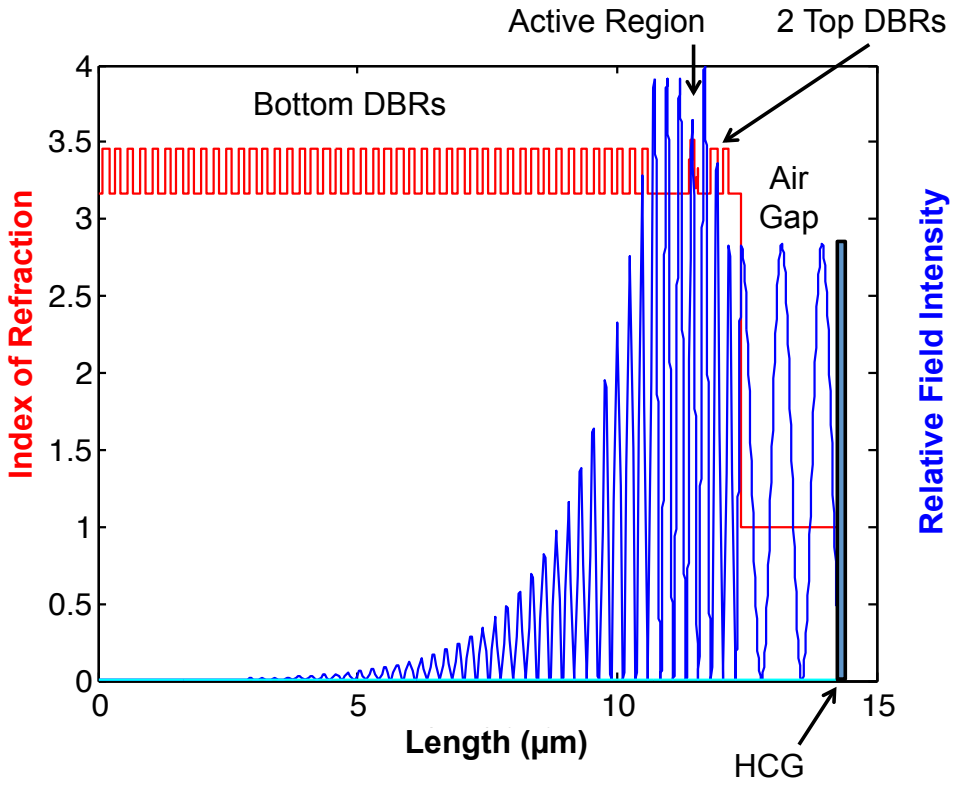

Figure 5.2 Electric field (blue) and index of refraction (red) as a function of distance inside of the structure. The overlap factor of the electric field with the active region is 1.8%.

The electric field inside of the 1550 nm VCSEL structure is simulated using transmission matrices [98]. A field is launched from one side of the structure, and recorded as it propagates through a transmission matrix that is incrementally increased in length. Figure 5.2 shows the electric field (blue) in the structure as well as the refractive index (red). The electric field is maximized across the active region to achieve as large an overlap factor as possible. An overlap factor of 1.8% is calculated by integrating the field in the active region and dividing by the integral of the field throughout the structure. At the same time, the field is minimized across the tunnel junction to minimize optical loss due to free carriers in the tunnel junction. Figure 5.3 shows the zoomed in view of the electric field (blue) and refractive index (red) across the active region and tunnel junction section.

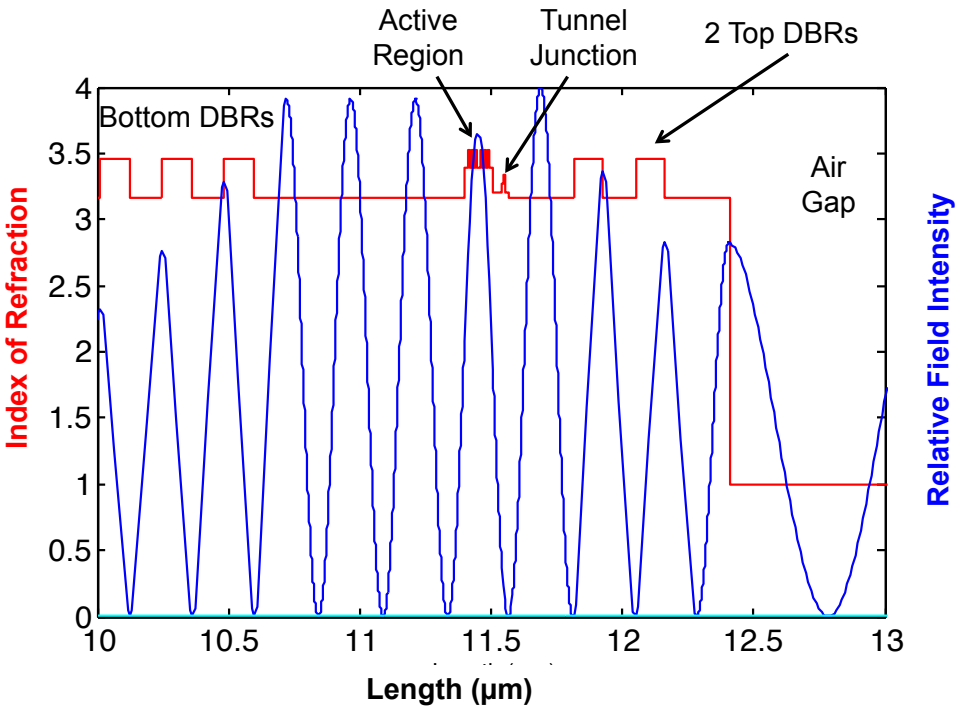

Figure 5.3 Zoomed view of the electric field (blue) and index of refraction (red) around the active region as a function of distance inside of the structure. The VCSEL is designed such that the electric field is maximized across the active region and minimized across the tunnel junction.

5.2.2 HCG Design

The HCG in this structure is ~195 nm thick and has a period of ~1070 nm and semiconductor width of ~370 nm. The grating is designed to highly reflect light with electric field polarized parallel to the direction of the grating bars (TE), but not to the orthogonal polarization (TM). The grating is optimized so that it has a wide tolerance to the air gap dimension for ease of fabrication. Figure 5.4 a) shows the simulated reflectivity of HCG as a function of wavelength and light polarization (TE light (blue) has its electric field polarized along the bar direction while TM (red) is polarized perpendicular to the grating bar direction). The simulation is performed using rigorous coupled wave analysis (RCWA) [92]. Over 99% of TE-polarized light is reflected, while only ~50% of TM-polarized light is. Figure 5.4 b) shows the reflectivity of the TE light as a function of wavelength over a smaller reflectivity interval. The TE HCG is over 99% reflective over a 150 nm range. In this simulation, parameters are fixed at: a grating thickness of 195 nm, a period of 1075 nm, and a grating duty cycle of 35% (equivalently ~370 nm of InP and ~700 nm of air per grating cycle). The HCG material is InP with a refractive index of 3.17 in all cases.

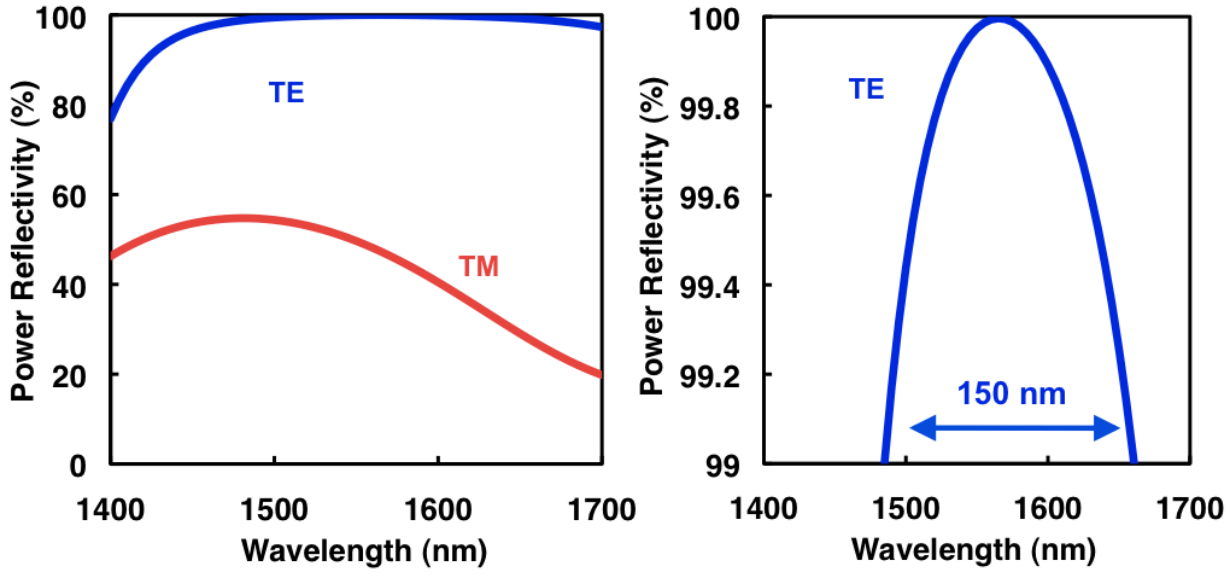

Figure 5.4 a) Reflectivity of the HCG as a function of wavelength and polarization. The grating is highly reflective for TE light (blue, light with electric field polarized along the direction of the grating), and much less so for TM light (red, light polarized perpendicular to the direction of the grating). b) Zoomed-in reflectivity of the TE polarization. The grating is over 99% reflective over a bandwidth of 150 nm.

5.2.3 Fabrication Process

Device fabrication was carried out as shown in Figure 5.4. Figure 5.4 a) shows the as grown substrate. First, a current aperture was formed by protecting the aperture area by a thick photoresist, followed by a H+ ion implantation with a dosage between 10^{14} cm^{-2} to 10^{15} cm^{-2} and energy between 250 keV to 400 keV, as shown in Figure 5.4 b). A top annular *n*-contact subsequently was fabricated through lithography, metal evaporation, and lift-off as shown in Figure 5.4 c). Next, a bottom contact is evaporated uniformly on the backside of the wafer, shown in Figure 5.4 d). A mesa was etched around the contact ring to the depth of the *n*-DBRs to electrically isolate the devices from each other. Figure 5.4 e) shows the device at this point in the process.

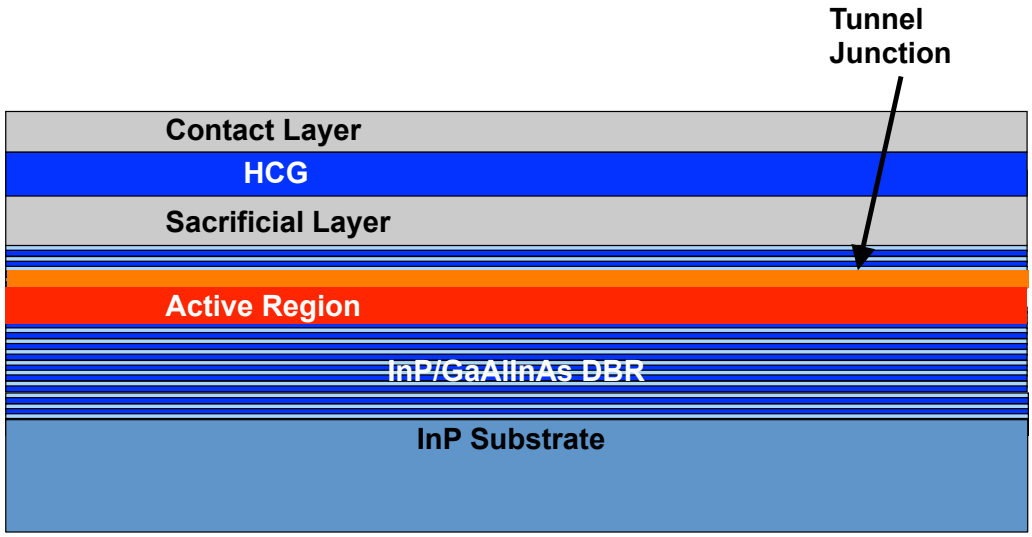
Tunnel
Junction
Contact Layer
HCG
Sacrificial Layer
Active Region
InP/GaAlInAs DBR
InP Substrate

(a)

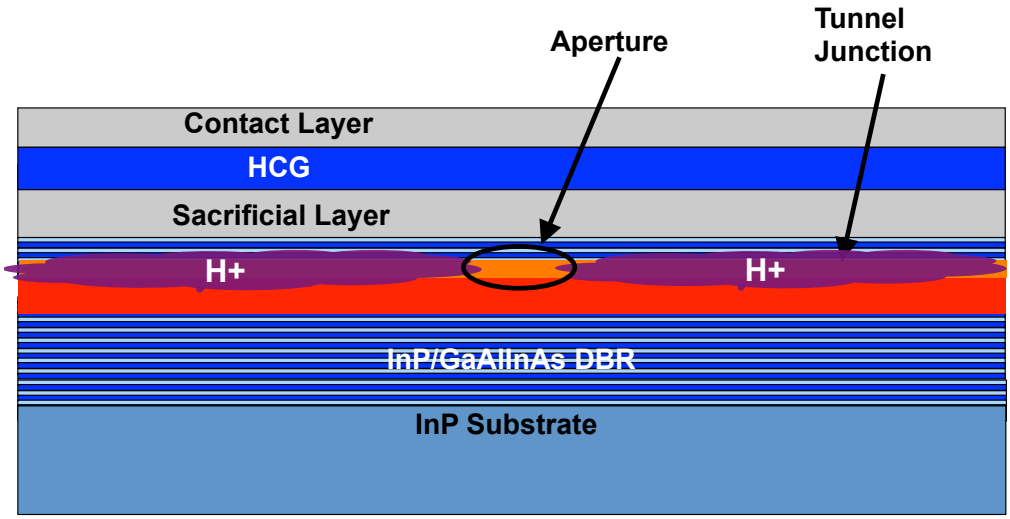
Aperture
Tunnel
Junction
Contact Layer
HCG
Sacrificial Layer
H+
H+
InP/GaAlInAs DBR
InP Substrate

(b)

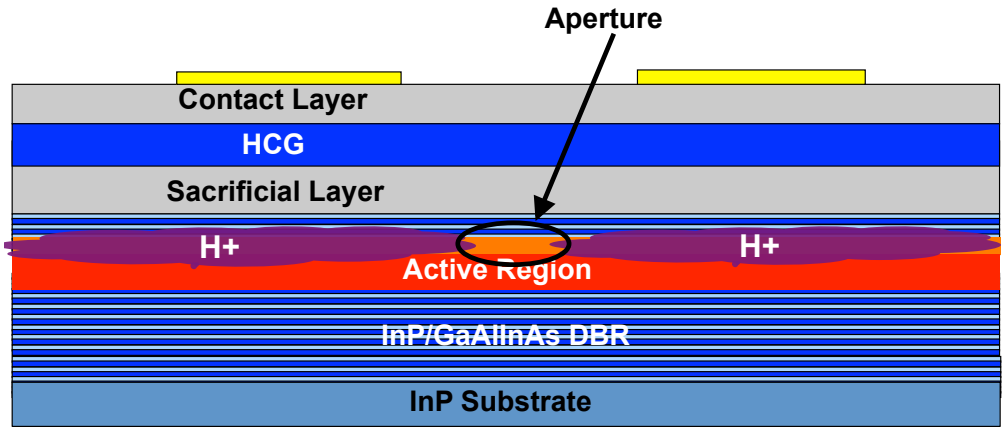
Aperture
Contact Layer
HCG
Sacrificial Layer
H+
H+
Active Region
InP/GaAlInAs DBR
InP Substrate

(c)

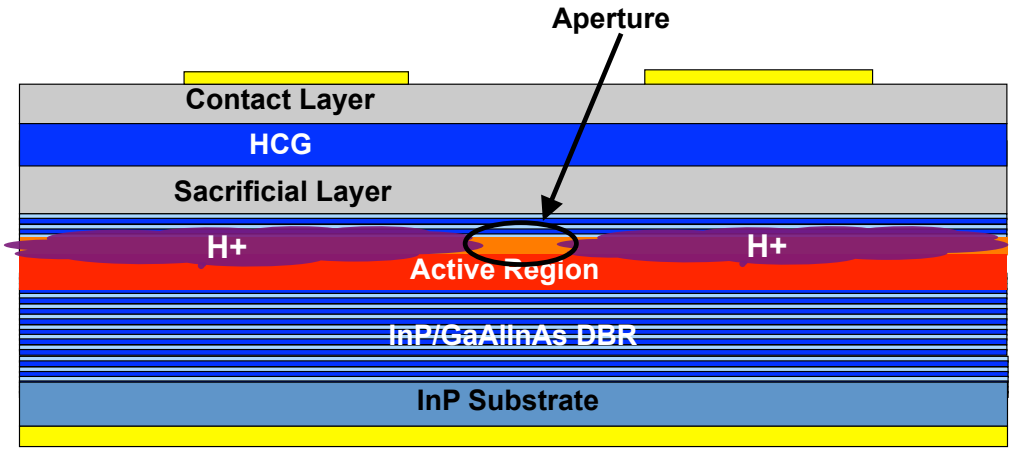
Aperture
Contact Layer
HCG
Sacrificial Layer
H+
H+
Active Region
InP/GaAlInAs DBR
InP Substrate

(d)

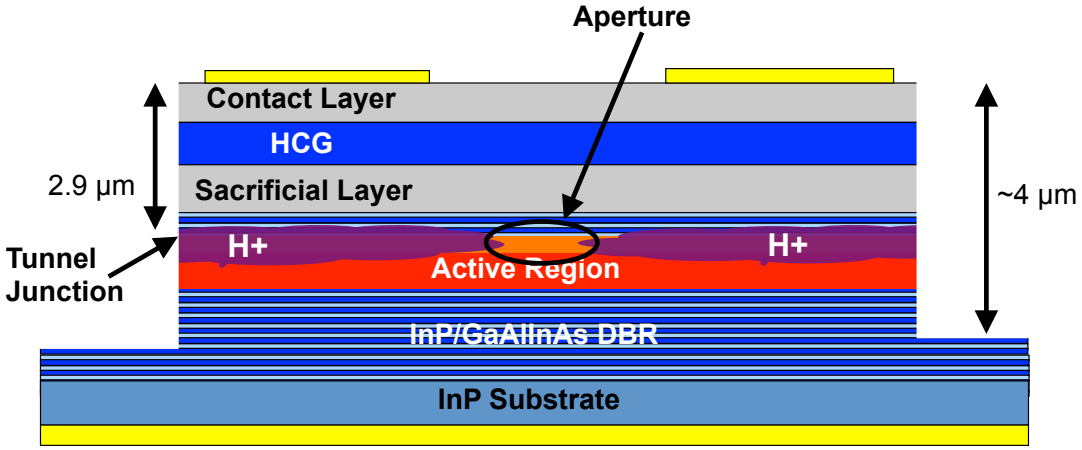
Aperture
Contact Layer
HCG
2.9 μm
Sacrificial Layer
~4 μm
Tunnel
Junction
H+
H+
Active Region
InP/GaAlInAs DBR
InP Substrate

(e)

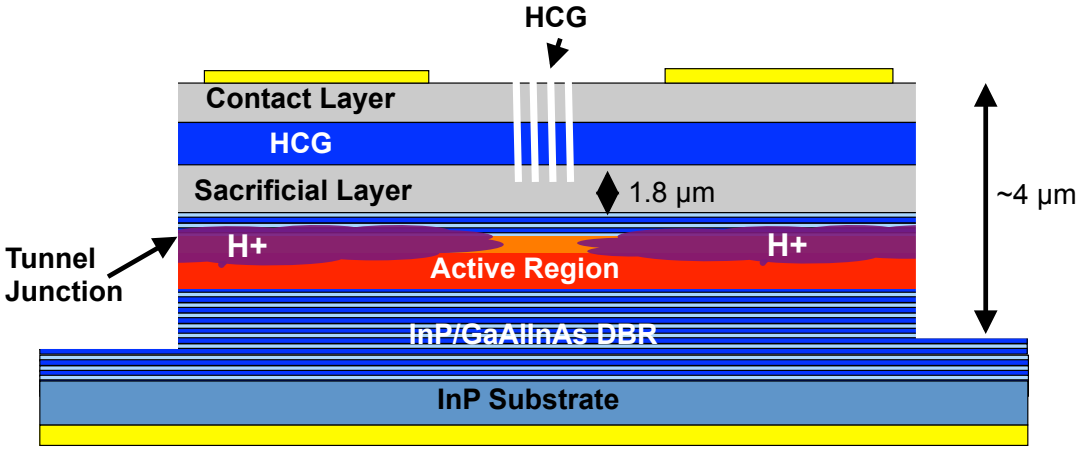
HCG
Contact Layer
HCG
Sacrificial Layer
1.8 μm
~4 μm
Tunnel
Junction
H+
H+
Active Region
InP/GaAlInAs DBR
InP Substrate

(f)

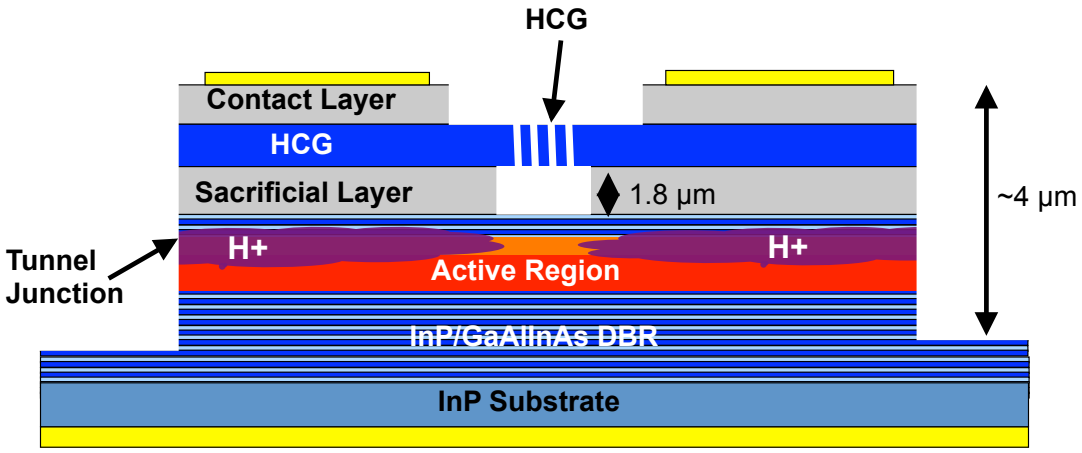

(g)

Figure 5.5 Fabrication process for the 1550 nm HCG VCSEL. a) The initial substrate. b) After ion implantation. c) top metal contact formation and d) backside contact deposition. e) A mesa etch is performed to electrically isolate devices. f) The HCG is patterned by electron beam lithography, and the pattern is transferred through a dry etch. g) High contrast grating release by wet etch. Critical point drying is used to prevent the HCG from clamping down while drying.

The HCG was defined by electron beam lithography and transferred by dry etching, as shown in Figure 5.4 f). In principle, the pattern could also be defined using a standard DUV lithography stepper. The HCG is then released by a selective etch of a sacrificial region below the HCG followed by critical point drying to prevent the structure from being damaged during the drying process. A schematic of the final fabricated structure is shown in Figure 5.4 g). A scanning electron microscope (SEM) image of a completed HCG VCSEL is shown in Figure 5.6 a). A zoomed in SEM image of the HCG is shown in Figure 5.6 b).

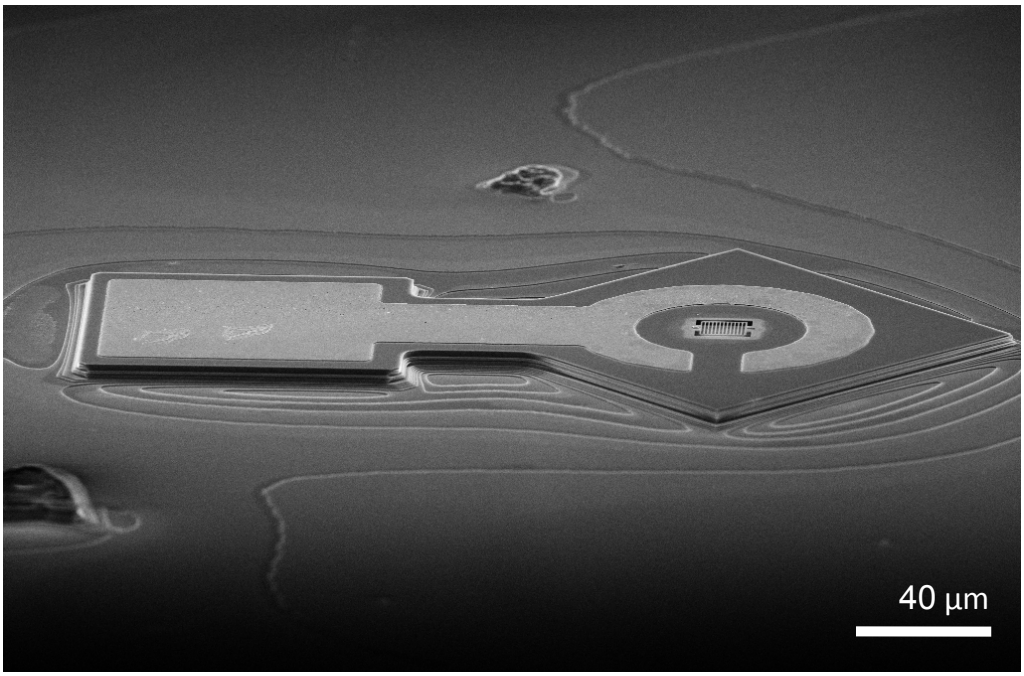

(a)

(b)

Figure 5.6 SEM images of a (a) a completed 1550 nm HCG VCSEL (b) A zoomed in image of the high contrast grating, which is just 195 nm thick.

5.3 Device Characteristics

5.3.1 Temperature Dependent Light-Current-Voltage Characteristics

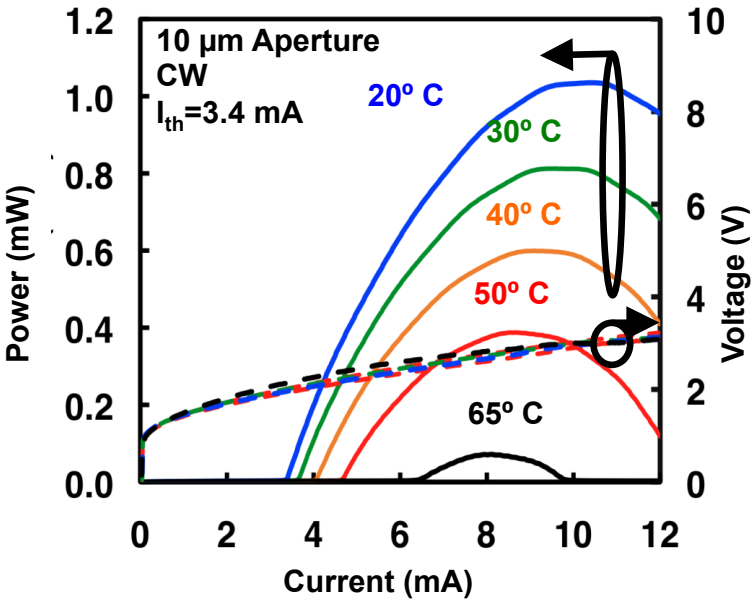

(a)

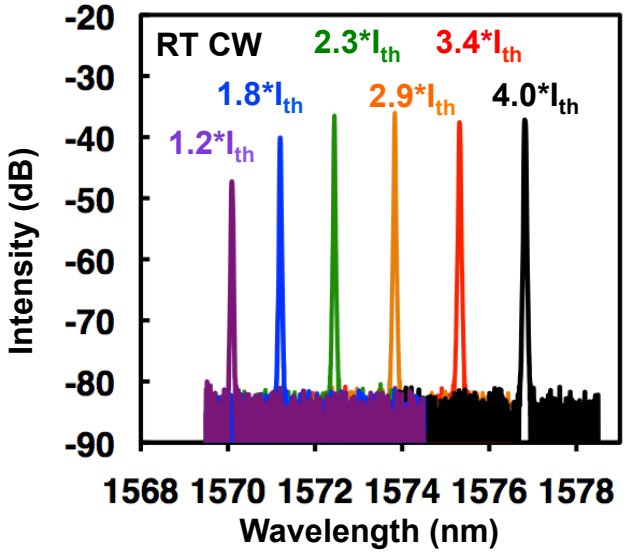

(b)

Figure 5.7 Light-current (solid lines) and voltage-current (dashed lines) characteristics of a HCG VCSEL with a 10 μm proton implant aperture at various heat sink temperatures under continuous wave operation. Devices show over 1.1 mW output power at room temperature and operate continuous wave to >60° C. b) Spectrums of the same device under various drive currents from 1.2x threshold current up to 4x under room temperature continuous wave operation. The threshold current is 3.5 mA for this device.

A series of VCSELs were fabricated with an identical HCG size of 12 X 12 μm^2 and various implant aperture sizes, ranging from 5 to 20 µm. The fabricated devices show excellent electrical and optical characteristics. Figure 5.7 a) shows the light-current (solid) and voltage-curent (dashed) characteristics of a VCSEL with a 10 µm proton implant aperture at various heat sink temperatures. The VCSELs has a threshold current of ~3.5 mA at room temperature (RT) and lase continuous wave (CW) at temperatures exceeding 60º C. The RT peak output power is ~1.1 mW with slope efficiencies greater than 0.25 mW/mA. Other devices with slightly higher thresholds showed up to 1.4 mW peak output powers at room temperature. The devices show a differential resistance of 40-100 Ω depending on aperture size. Figure 5.7 b) shows the spectrum of the same device under different bias currents, from 1.2X threshold current up to 4X, at room temperature under continuous wave operation. The device is single mode with greater than 40 dB side mode suppression ratio throughout all operating currents. A wavelength-tuning coefficient of 0.65 nm/mA was measured.

Figure 5.10 shows the optical spectrum of the same device at a constant bias current of 7.1 mA at various heat sink temperatures. A wavelength shift of 0.12 nm/K is observed. A thermal resistance of 1.55 K/mW is realized, indicating good heat transfer away from the active region. At all biases, the VCSELs emit in a single transverse mode with a side mode suppression ratio > 45 dB. Single mode emission was seen in VCSELs with proton-implant-aperture sizes up to 20 µm. It should be noted though that the HCG is only 12 X 12 μm^2, so the finite HCG size is also providing some transverse mode discrimination.

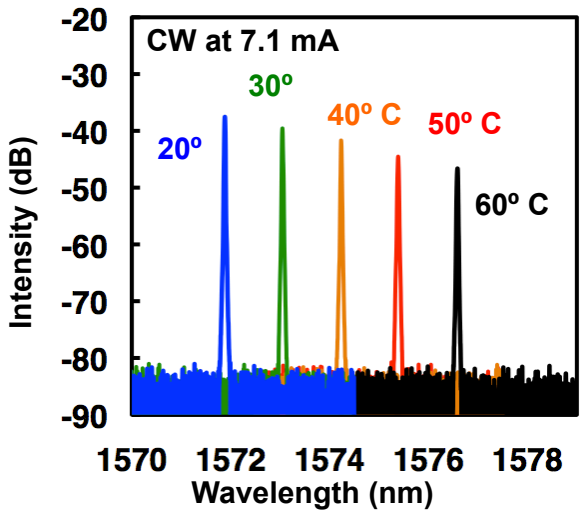

Figure 5.8 Spectrum of the same device as Figure 5.7 under various heat sink temperatures. A wavelength shift of 0.12 nm/K is extracted. A wavelength shift of 0.12 nm/K is extracted.

5.3.2 High Power 1550 nm HCG VCSEL

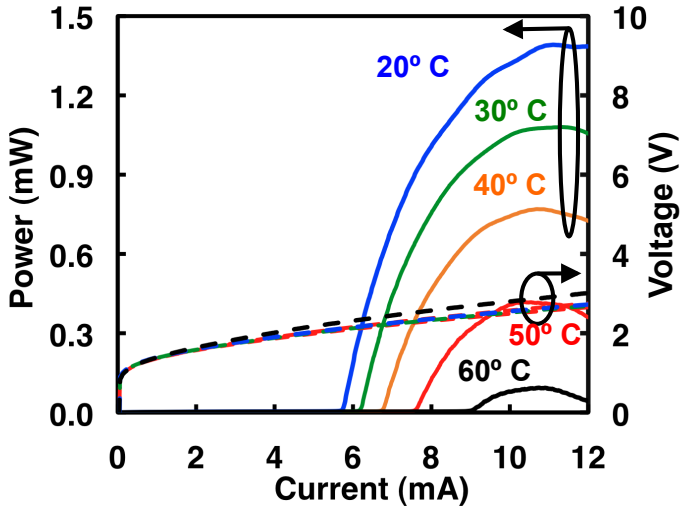

Figure 5.9 Light-current (solid lines) and voltage-current (dashed lines) characteristics of a high power HCG VCSEL with an 11 μm proton implant aperture at various heat sink temperatures. The device shows up to 1.44 mW output power at room temperature and operates continuous wave to >60° C.

Our best device was able to achieve as high as 1.45 mW output power under CW room temperature operation. The light-current (solid) and voltage-current characteristics as a function of heat sink temperature is shown in Figure 5.9. This device has a slightly higher threshold current of 5.8 mA and a differential resistance of ~95 Ω. Its slope efficiency is 0.7 mW/mA. This device had an 11 μm aperture. The spectrum of the same device biased at 10 mA at 20° C under CW operation is shown in Figure 5.10. This device lased around 1570 nm and was single mode with a side mode suppression ratio exceeding 40 dB.

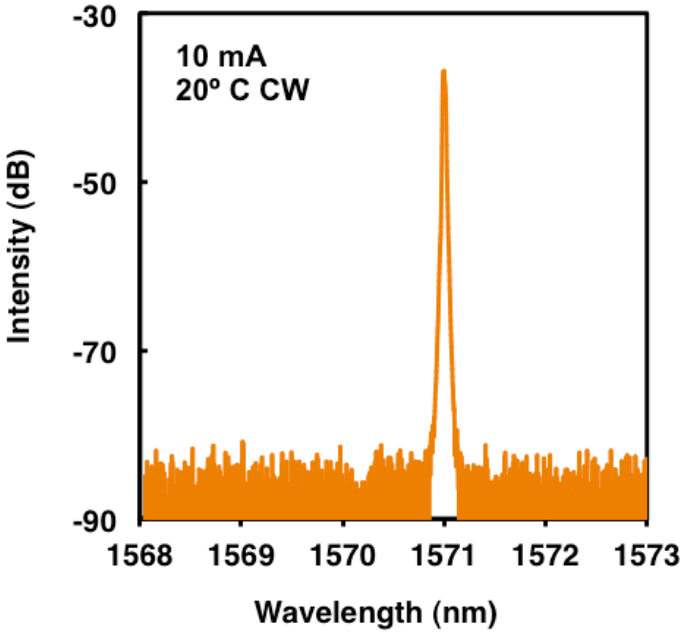

Figure 5.10 Spectrum of the same high power device as Figure 5.9 under continuous wave operation at 20º C with a bias current of 10 mA. The device is single mode with a SMSR >40 dB.

5.3.3 Aperture Dependent Characteristics

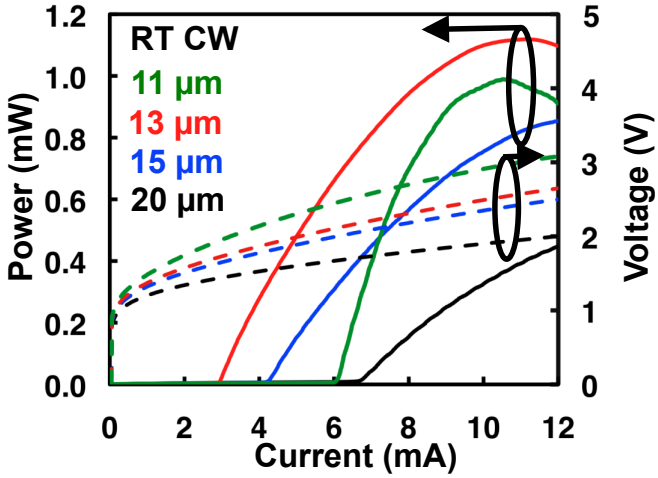

Figure 5.11 Light-current (solid lines) and voltage-current (dashed lines) characteristics of 1550 nm HCG VCSELs with different aperture sizes from 11 to 20 µm but otherwise identical structures including the HCG, which is 12 µm X 12 µm. Devices are operated CW at room temperature.

A series of VCSELs were fabricated with an identical HCG size of 12X12 μm^2 and various implant aperture sizes, ranging from 5~20 um. Besides the aperture size, the devices were basically identical. Light and voltage vs. current characteristics for VCSELs under room temperature CW operation with aperture sizes from 11 to 20 μm are shown in Figure 5.11. The lowest threshold was achieved with an aperture of 13 μm. Differential resistance of the devices rose inversely with aperture size as expected. The poorer performance of the larger aperture size devices is likely due to the VCSEL aperture being larger than the HCG size. A HCG better matched to the larger aperture sizes should perform better. However, devices work with apertures up to 20 μm diameter anyway. This indicates a large alignment tolerance of the HCG to the proton implant aperture. The optical spectrums of the same devices at twice the threshold current under room temperature continuous wave operation are shown in Figure 5.12. All devices are single mode including the 20 μm aperture. The emission wavelengths of the devices are all similar as well.

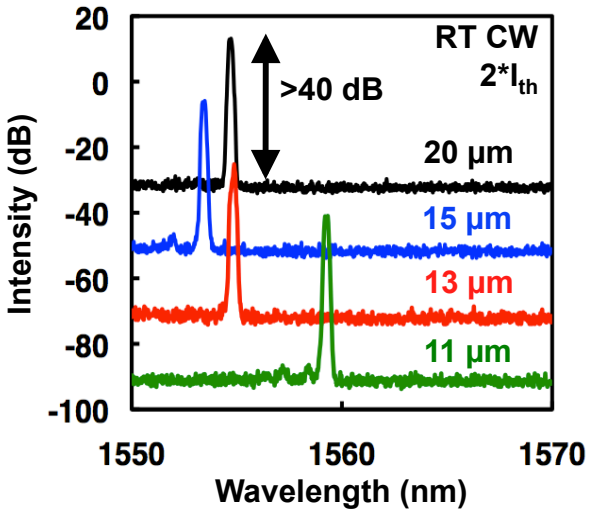

Figure 5.12 Spectrum of the same devices as Figure 5.11 under room temperature continuous wave operation under a current bias of 2 X I_{th}. All devices are single mode. Spectrums are offset by 20 dB for clarity.

5.3.4 Optical Mode Characteristics

Favorable optical mode characteristics for optical communications applications are also obtained due to the use of the HCG and a proton implant aperture. An important characteristic for VCSELs for mid- and long-reach optical communications links is polarization stability, as any polarization instability can have detrimental effects on an optical link. HCG VCSELs are polarization stable due to the high differentiation between the reflectivity in the orthogonal electric field polarizations as discussed in section 2.4. Figure 5.13 shows the polarization-resolved light-current characteristics of a device with a 15 μm proton implant aperture and 12 X 12 μm^2 HCG under room temperature continuous wave operation. The orthogonal polarization is suppressed by greater than 20 dB (limited by the polarizer in the experimental setup).

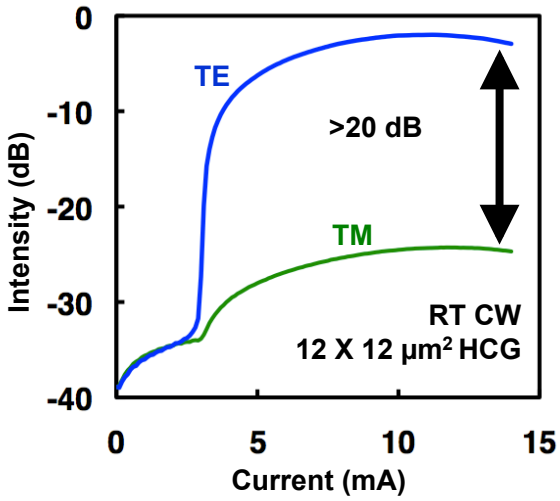

Figure 5.13 Polarization-resolved light-current characteristic of a 1550 nm HCG VCSEL. A polarization suppression ratio of >20 dB is achieved, with the measurement limited by the polarizer.

Since proton implant defined apertures provide little optical index guiding, it is possible to achieve larger size apertures while maintaining a single transverse mode emission profile than in an oxide aperture VCSEL. This makes proton implant VCSELs ideal for high coupling efficiency to a single mode fiber. The near field intensity profile of a device with a 15 μm proton implant aperture and 12 X 12 μm^2 HCG is shown in Figure 5.14. This device emits in a single fundamental transverse mode with a full width half maximum (FWHM) of ~6.5 μm. Generally, the devices have FWHMs of 40-50% of their lithographically defined aperture size. VCSELs with >20 μm proton-implant-defined apertures show no significant higher order transverse mode, since the finite area of HCG reflectivity (12X12 μm^2) also contributes to the suppression of the higher order transverse modes in the largest aperture devices.

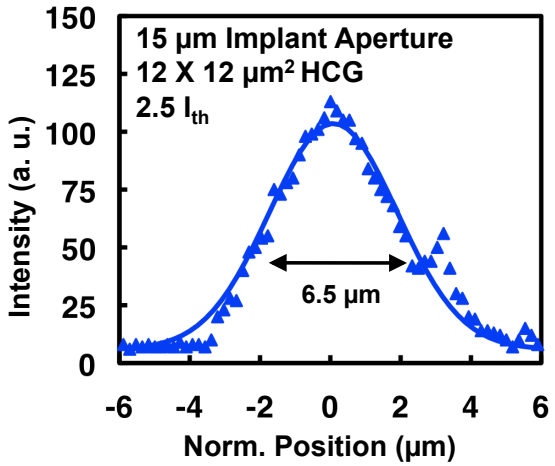

Figure 5.14 Near field intensity profile of the device at 2.5 X I_{th}. A FWHM of ~6.5 μm is obtained with a VCSEL with a proton implant aperture size of 15 μm.

5.4 Summary

In this chapter, we demonstrated an InP-based VCSEL utilizing an HCG as a top mirror and proton implantation to form an electrical aperture. These devices can be simply fabricated using a monolithic epitaxial growth without the need for additional regrowth or dielectric mirror deposition. These devices have greater than 1 mW output power at room temperature and operate continuous wave to temperatures greater than 65º C. Single mode operation is achieved with large apertures and no degenerate polarization mode. This simple VCSEL structure is promising as a manufacturable, low-cost, long wavelength VCSEL for optical communications applications.

Chapter 6 Multiwavelength Arrays of VCSELs using a High Contrast Grating

6.1 Motivation

Wavelength division multiplexing (WDM) has become the dominant method for achieving high data throughput through a single optical fiber, and has become the dominant technology in long haul optical communications links. Over shorter distances, to date, WDM has not been required, but is becoming increasingly desirable due to the advent of high definition video streaming and other high bandwidth consumer applications as well as data-heavy computations in modern data centers. Unfortunately, the current WDM technologies are not cost effective for these consumer level applications.

One highly desirable component for a low cost WDM system is a low cost array of lasers operating with each laser at a different wavelength. VCSELs would be ideal in this application. Creating arrays of VCSELs emitting at multiple wavelengths has been a subject of much research as discussed in Chapter 1. Unfortunately, an approach that offers controlled wavelength spacing and can be achieved with a scalable manufacturing approach has not been achieved to date.

High contrast gratings offer intriguing possibilities for achieving multiwavelength VCSEL arrays that could potentially be manufactured in a scalable manner. Here, we present two approaches for achieving multiwavelength arrays using a high contrast grating. The first manipulates the phase of the reflection of the HCG while leaving the rest of the VCSEL structure constant, creating a multiwavelength VCSEL array defined in a purely lithographical manner leading to a potentially very low cost multiwavelength VCSEL array. The second accesses the cavity between the HCG and the VCSEL body after epitaxial growth and creates different optical path lengths during post-growth processing, another intriguing method for creating a low cost multiwavelength VCSEL array.

6.2 Multiwavelength Array using HCG Phase Variation

6.2.1 Concept

The HCG has been shown previously to be able to maintain a high reflectivity but variable reflectivity phase purely by changing the grating period and air gap [82], [84]. This is extremely desirable, as a highly reflective mirror with a controllable reflectivity phase can then be lithographically defined on a planar structure in a simple, low cost manner.

The cavity wavelength of the VCSEL is related to the phase of the mirror by the relation:

$$2\,\pi\,\frac{2\,n\,L_{Cavity}}{\lambda} + \phi_{Mirror\,1} + \phi_{Mirror\,2} = 2\,\pi\,m \qquad (6.1)$$

where L_{cavity} is the length of the VCSEL cavity; n is the refractive index of the cavity material(s); $\phi_{Mirror\,1/2}$ is the reflectivity phase of the VCSEL's mirrors; and m is an integer. Thus if the phase of the mirror can be changed and all other things remain the same from device to device, the wavelength of the cavity can be controllably varied using only lithography.

By using HCGs with different duty cycles and periods but the same HCG thickness, an array of mirrors with different phases can be achieved monolithically using the same HCG thickness, and hence the same epitaxial wafer.

By applying this array of mirrors with different phases to an array of VCSELs, an array of VCSELs with different wavelengths dependent on the phase of the mirror can be achieved. This multiwavelength array is achieved purely through post growth patterning, a simple, low cost, manufacturable approach, especially when compared to previous approaches to achieving multiwavelength VCSEL arrays utilizing growth-based cavity variation methodologies [56]. A schematic of the proposed approach is shown in Figure 6.1

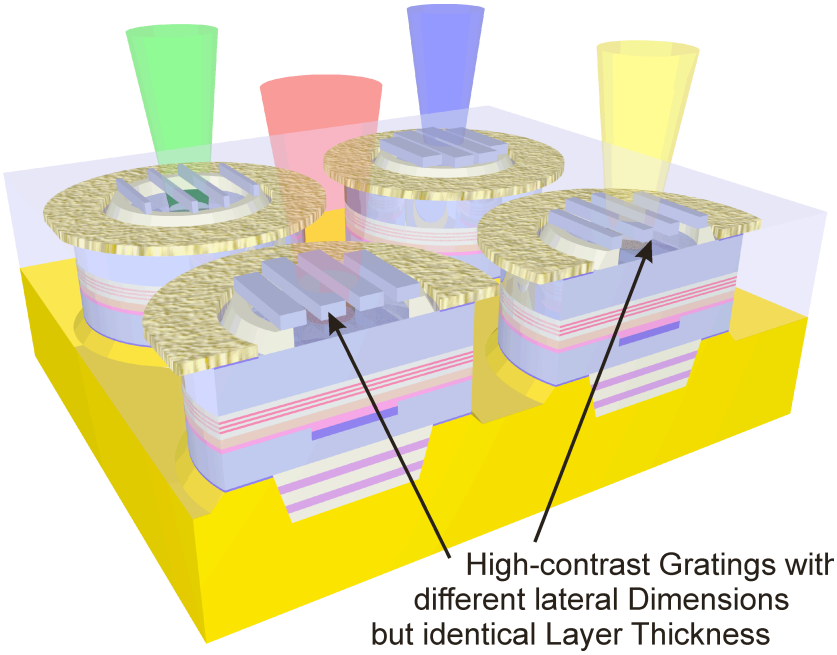

Figure 6.1 Schematic of the multiwavelength HCG VCSEL array. Multiple wavelengths are achieved by varying the period and duty cycle of the HCG, changing the phase of reflectivity from the top mirror.

6.2.2 HCG Variation Simulation

To explore the potential of the HCG multiwavelength array concept, an RCWA simulation was performed sweeping the duty cycle and period of a HCG while keeping the HCG and the rest of the structure constant. The VCSEL cavity structure used in the simulations is similar to previously demonstrated 1550 nm VCSEL designs [21].

The VCSEL structure used in this simulation is shown schematically in Figure 6.2. The VCSEL consists of, from the bottom, five pairs of dielectric DBRs. Above these DBRs is a spacer InP layer that is one lambda thick. The active region contains of five GaAlInAs QWs. Above the active region is another InP spacer layer to provide uniform current injection to the electrical aperture. The electrical aperture in this design could be defined by a buried tunnel junction [11] or proton implant [28]. Above the second InP layer is an air gap and an InP HCG. In principle, the top two layers could be designed to be SiO_2 as the low index material and Si as the HCG, so a release process could also be avoided. The HCG used in this simulation was 900 nm thick, as thicker HCG layers give larger phase changes due to dimension variation since there is there is a longer optical path in the HCG for the field to interact with.

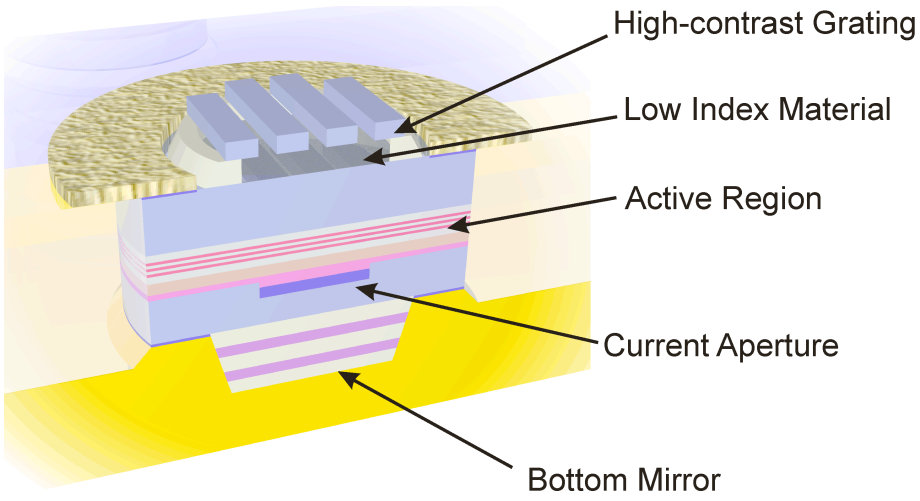

Figure 6.2 Schematic of the VCSEL structure used in the multiwavelength array design. This device consists of, starting from the substrate side, a dielectric DBR mirror, a VCSEL cavity including an active region and a current aperture, and on top of this all an air gap with an InP HCG above it.

The VCSEL's simulated cavity wavelength versus HCG semiconductor bar width (red) and period (blue) are shown in Figure 6.3. A VCSEL cavity with a suitable top mirror reflectivity (>99%) can be achieved over a 200 nm wavelength range purely by changing HCG width and period, while leaving the rest of the structure the same. To do so, the semiconductor bar width is drastically changed, ranging from ~100 nm to 700 nm. The period also changes but not nearly as significantly, varying from 1000 to 1400 nm. It should be noted that at the edge of the range, the bandwidth of the top mirror over 99% becomes small, potentially making fabrication difficult. Regardless, top mirrors of a reasonably wide bandwidth are seen through the center of the wavelength range.

One major advantage of this approach is that it can extend beyond the free spectral range of the cavity since the reflectivity bandwidth and center of the top mirror is changing as a function of the grating dimensions [84]. Though two modes may both be overlapping with the active region at the same time, only one mode will lase, as the mirror will only provide high reflectivity for one of the two longitudinal modes. Any other approach where the reflectivity band is fixed would be limited to the free spectral range of the VCSEL cavity as the lasing mode could not easily be deterministically fixed to either of the two cavity modes.

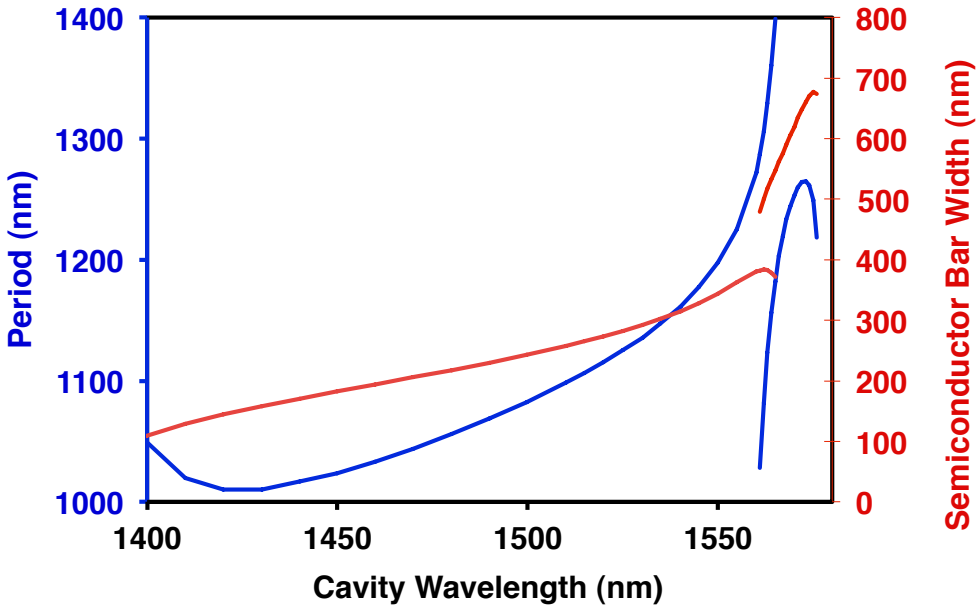

Figure 6.3 An example HCG design optimized for a 1550 nm VCSEL showing VCSEL cavity wavelength versus the HCG period (blue) and bar width (red). In principle, a 200 nm range of cavity wavelengths is possible with a single HCG design. In a practical system though, the gain bandwidth of the active region will limit the available range to a smaller range.

6.2.3 Cavity Simulation

Of course, from a practical perspective, there are other reasons that may prevent this full wavelength range from being realized. The ultimate limiting feature for the wavelength range achievable with the device is the gain bandwidth of the active region. The bottom mirror high reflectivity bandwidth can also place a limit on the achievable lasing range if a semiconductor DBR is used, as their high reflectivity bandwidths are usually on the order of 60 to 80 nm. Thus to go beyond this limitation, a dielectric DBR can be used, providing hundreds of nanometers of high reflectivity bandwidth. Another potential limiting factor of the achievable wavelength range is the overlap between the electric field and active region with the laser cavity.

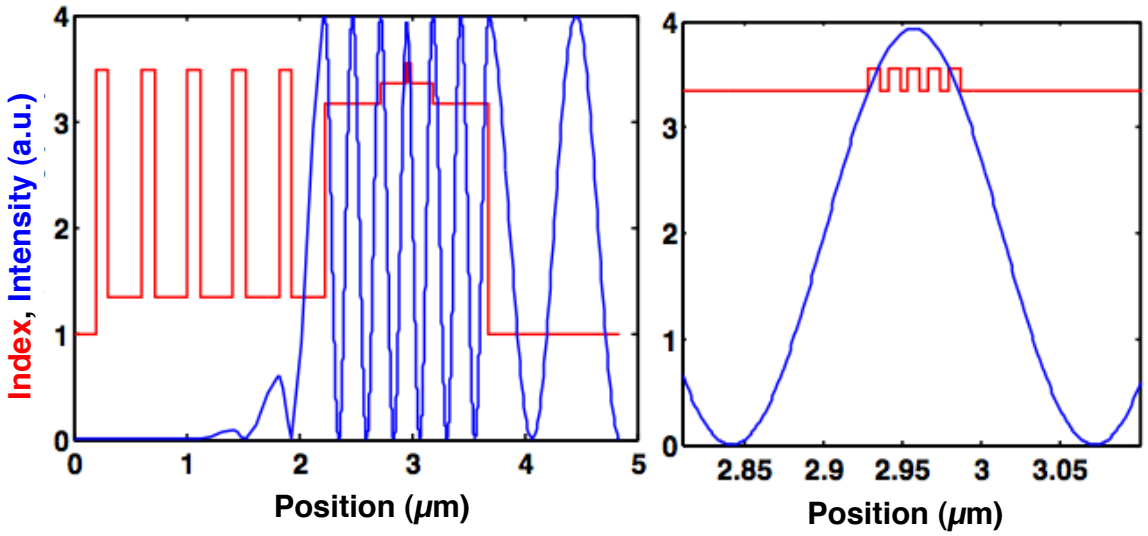

(a) (b)

Figure 6.4 (a) Field intensity profile (blue) and refractive index of the materials (red) of the cavity of a multiwavelength HCG VCSEL structure, simulated at 1570 nm. (b) The same structure zoomed in on the active region.

To see the influence of the HCG phase tuning on the standing cavity wave and the overall confinement factor of the VCSEL, transfer matrix [98] calculations were performed on the cavity at wavelengths across the tuning range. The cavity design was the same as described earlier. The standing cavity wave (blue) at 1570 nm with the index profile (red) overlaid for comparison is shown in Figure 6.4. Figure 6.4 a) shows the entire structure, and Figure 6.4 b) shows just the active region. At 1570 nm, a good overlap of the quantum wells with the field in the optical cavity is achieved.

The confinement factor was estimated for various wavelengths from 1500 to 1600 nm by integrating the field across just the active region and dividing that by the integrated field in the entire device (excluding the HCG). Here the lateral confinement is assumed to be 1. The result is shown in Figure 6.5. Across a bandwidth of 32 nm, corresponding to the bandwidth of the entire C band, the confinement factor is >90% of its peak value, so all C band wavelengths could be addressed purely by variation of lateral HCG dimensions, while at the same time having reasonably uniform device performance. Over a larger range, the HCG multiwavelength array would still work, though as the confinement factor becomes less, more variation in device performance would be expected as a function of wavelength. The devices at the edges of the range would be expected to have increased threshold currents due to their weaker confinement factor.

The ultimate limit of the wavelength range possible with this approach would likely be determined by the overlap factor in combination with the underlying gain bandwidth of the VCSEL's active region. Tunable VCSELs have a similar wavelength range limitation due to the confinement factor and gain bandwidth. The best tunable VCSEL designs to date can achieve ~76 nm [48], so a HCG multiwavelength array using HCG phase variation could be expected to achieve a similar range.

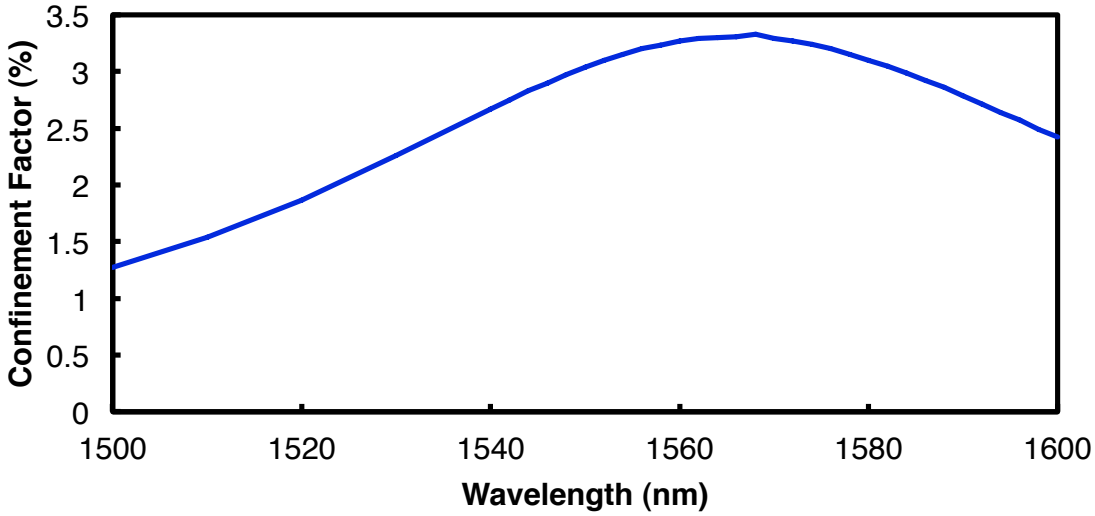

Figure 6.5 Confinement factor of a HCG VCSEL as a function of wavelength. Over the erbium window (1550-1582 nm), the confinement factor is still larger than 90% of its peak value.

Here we have shown through simulation the potential of a HCG-based VCSEL array emitting at multiple wavelengths and achieved purely by post-growth, lithographic variation in the pattern of the HCG. Varying the VCSEL cavity through HCG variation can access a range of cavity wavelengths greater than 200 nm. The overlap of the VCSEL's field with the active region and active region bandwidth will limit the range of the structure to a smaller region. A wavelength band greater than the C band is easily achievable though. This approach presents a major opportunity for the realization of low cost multiwavelength VCSEL arrays.

6.3 Multiwavelength VCSEL by Cavity Length Variation

6.3.1 Concept

Another method to create a multiwavelength array of VCSELs using a HCG is to change the cavity length itself directly. Though previously multiwavelength VCSEL arrays have been produced using this approach [56], [58], this has always been implemented using growth-based variation, which is difficult to control. An alternative approach would be to vary the cavity wavelength by removing material in the middle of the structure selectively after growth. Doing this in a controllable manner after growth could lead to a low cost, manufacturable solution to multiwavelength VCSEL arrays.

In a typical VCSEL structure with two epitaxial DBR mirrors though, this is not practical, because one of the epitaxial mirrors must be removed to access the cavity. In an HCG VCSEL however, it is possible to access the cavity post-growth [107] as the HCG is porous and etchants can go through it to etch materials inside of the cavity. By controllably etching the sacrificial layer below the HCG, various depths of air gaps can be realized as shown schematically in Figure 6.6. By not totally removing the sacrificial layer, the optical path length is increased due to the added high index material between the HCG and rest of the structure. Contrary to the

blue shift seen in a tunable VCSEL when the air gap is decreased, in this case, as the air gap is decreased, the cavity red shifts, as more high index material is added to the cavity, lengthening the optical path.

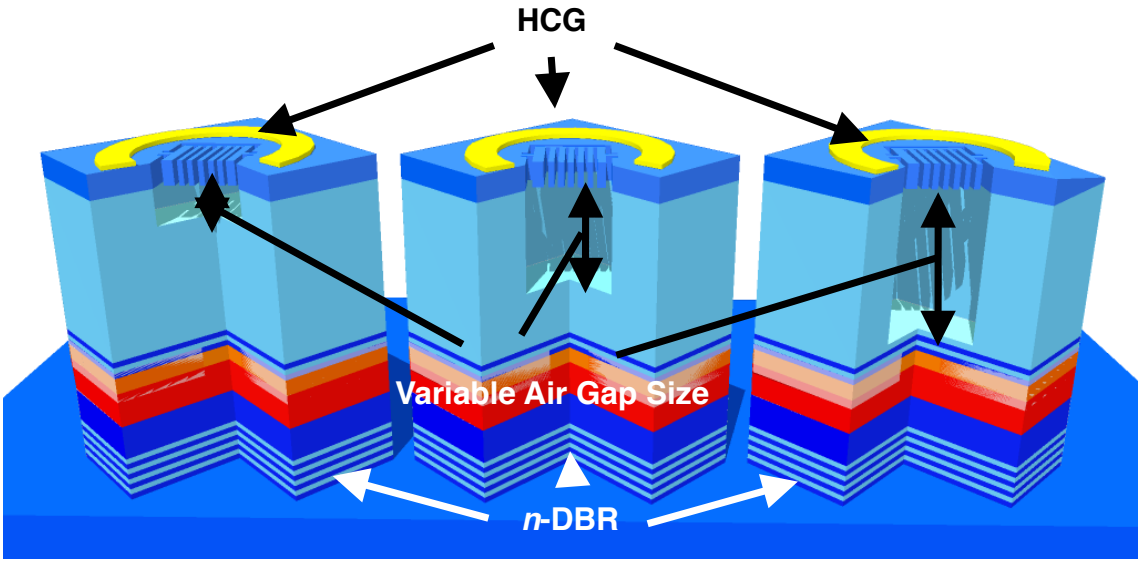

Figure 6.6 Schematic of a HCG multiwavelength array achieved by cavity length variation. Though the physical cavity length is not changed, the air gap below the HCG can be etched to various depths, changing the optical path length in the VCSEL cavity.

6.3.2 Cavity Design

This concept was explored using the same epitaxial design for a 1550 nm HCG VCSELs as was discussed in Chapter 5. The structure was simulated using RCWA with various amounts of sacrificial layer material being left in the cavity, correspondingly reducing the air gap between the HCG and the VCSEL body. The peak of the cavity was recorded as a function of the air gap. The results are shown in Figure 6.7. The cavity wavelength shifts at a rate of approximately 0.3 nm per nm that the air gap is reduced. As the air gap is reduced to about 1.7 μm, a new mode enters the area of interest around 1.55 μm as the original mode shifts out beyond 1.6 μm. The spacing between the two modes is approximately 85 nm.

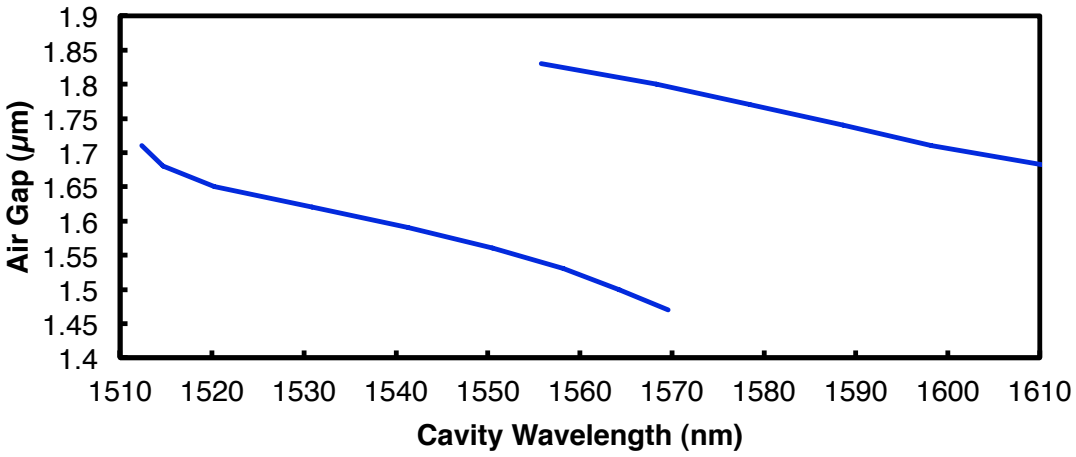

Figure 6.7 The wavelength of the VCSEL cavity as a function of the air gap depth. The cavity red-shifts redder by approximately 0.3 nm per nm less of air gap.

One limiting factor in the wavelength range of this design is the bottom DBR reflectivity bandwidth, as shown in Figure 6.8, which shows both the HCG (blue) and DBR (green) reflectivity as a function of wavelength. The DBR has enough reflectivity for the VCSEL to lase across an approximately 65 nm band. This bandwidth could be further expanded upon by either adding more pairs of DBR or by switching to a dielectric mirror, as was shown in section 6.2.2. With an optimized bottom mirror, the whole free spectral range of the cavity (approximately 85 nm) could be accessed as the HCG provides sufficient reflectivity across a wide enough range of wavelengths.

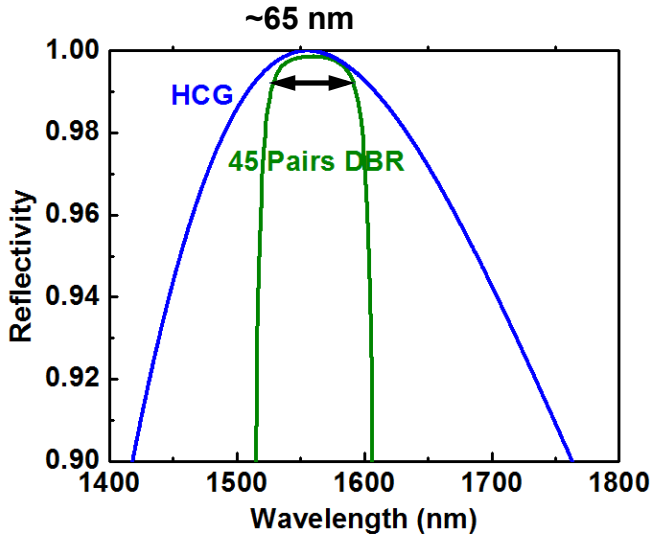

Figure 6.8 Reflectivity bandwidth of the DBR (green) and HCG (blue) used in the design. The lasing range is limited by the bandwidth of the DBR, which is only high enough for the VCSEL to lase across a ~65 nm band.

6.3.3 Experimental Realization

In order to test this concept, VCSELs were fabricated using the same wafer design as described in section 5.2.1 Chapter 5. Variable air gaps were fabricated on the same piece of wafer on VCSELs in close proximity to each other, causing wavelength change across a piece. The wavelength variation was achieved by slowly dipping the wafer into the etching solution, letting one side etch longer than the other and achieving a varying air gap size across the wafer. Wavelength differences of up to 25 nm were realized across a single piece. Across multiple pieces from the same wafer a difference of ~50 nm was achieved. It should be noted that some of the variation may be due to epitaxial variation between the pieces, but a significant portion of the wavelength variation is due to difference in air gap size as only minor variations in epitaxial thickness are expected across the full wafer.

Figure 6.9 shows the light-current-voltage characteristics and optical spectrums of various devices. The devices do not show uniform characteristics here, but with process optimization, better uniformity is expected. The devices at the edge of the range are expected to have somewhat reduced performance since the overlap factor of the cavity field with the active region is reduced at wavelengths away from the center of the range. Similarly, the gain from the active region is maximal at the center of the range, so a reduction in gain in the structure also occurs at the edges of the range. Nonetheless, devices over a 53 nm range lase using a common epitaxial structure and only variation of the air gap between the HCG and body of the VCSEL to achieve different wavelengths. Additionally, this is the first experimental demonstration that an HCG can provide a broadband high reflectivity of greater than 99% across a wavelength range of over 50 nm.

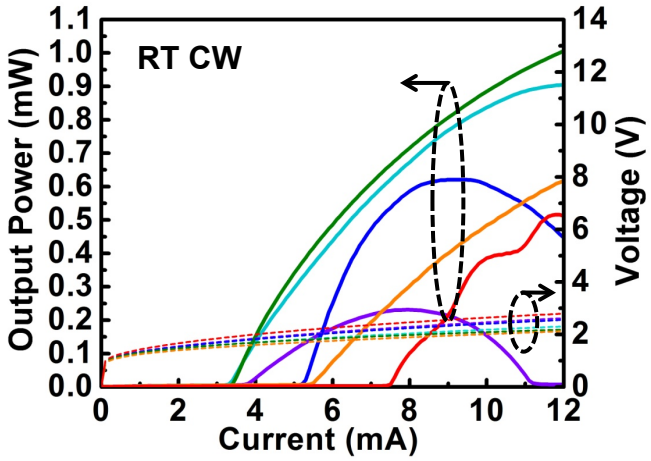

(a)

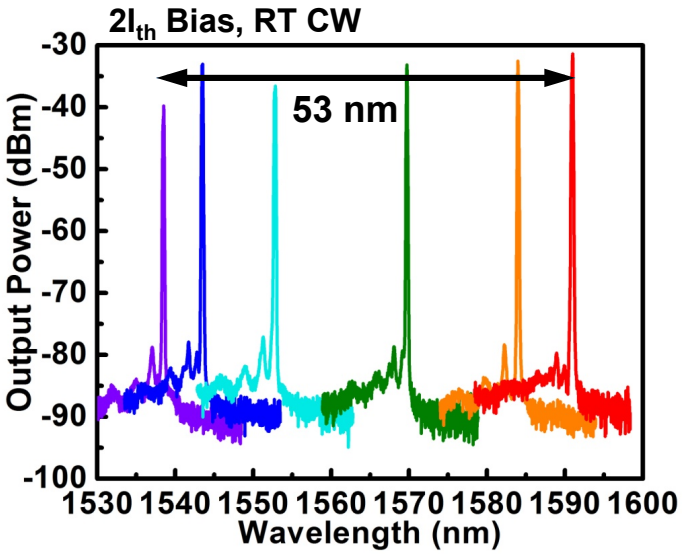

(b)

Figure 6.9 (a) Light-current-voltage characteristic of various HCG VCSELs fabricated from the same wafer but with different air gaps. (b) Optical spectrums of the same devices (The same color in part a and b indicates the same device). Devices are realized across a 53 nm wavelength range from the same base epitaxial wafer.

6.3.4 Similar Concept using Alternative Mirrors

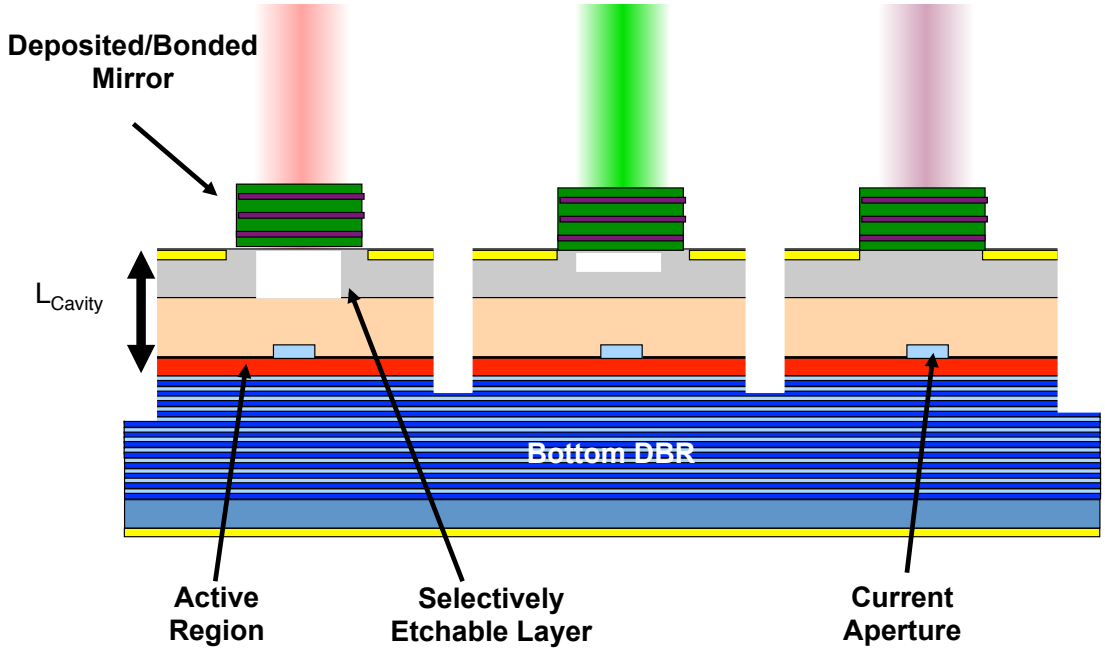

(a)

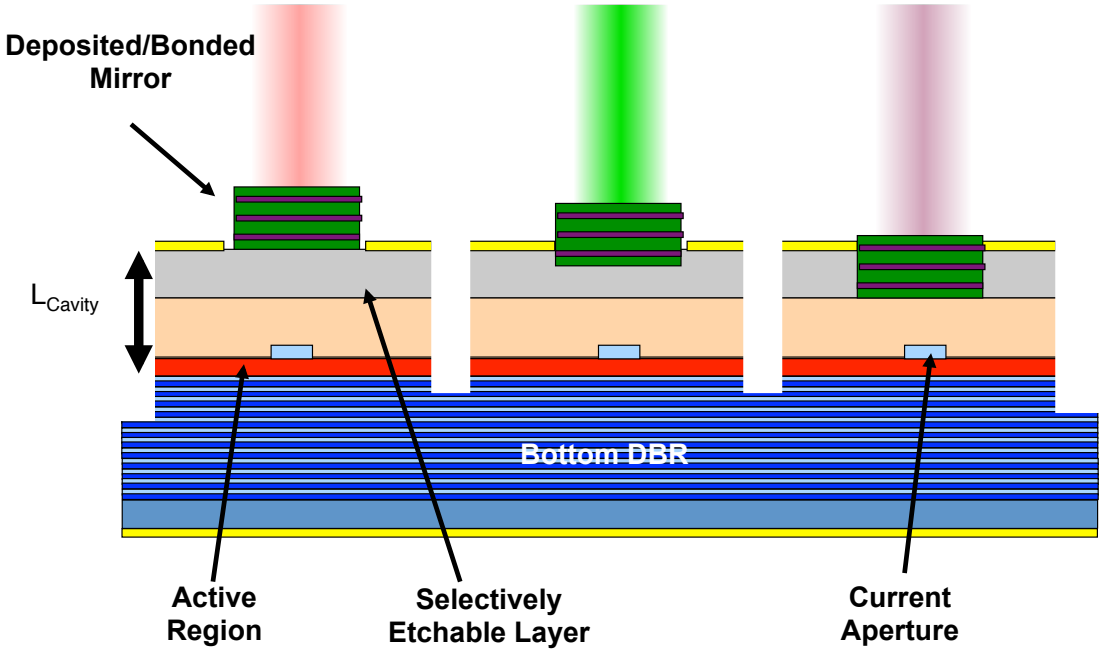

(b)

Figure 6.10 Alternative approaches for creating an array of VCSELs emitting at multiple wavelengths. a) Multiwavelength VCSEL array created by selectively forming air gaps of different thicknesses below top mirrors, which are attached post-growth. b) Multiwavelength VCSEL array created by selectively thinning the cavity before attaching top mirrors post-growth.

A similar approach could be used in any case where the mirror is attached afterwards in a VCSEL process, whether the mirror is an HCG or some other type of mirror. In the case of either a dielectric mirror [21], or bonded mirror [27] this would be possible as the mirror is attached to the rest of the structure after some processing has already occurred. Using selective etch layers on the top of an epitaxial structure, air gaps of various depths could be created. Afterwards, the mirror could be attached, leaving a structure conceptually similar to the HCG case as shown schematically in Figure 6.10 a), which would be the case for some type of bonded mirror. In the case of a top dielectric mirror, which is uniformly deposited and would fill in the air gap, a multiwavelength VCSEL array structure shown schematically in Figure 6.10 b) would be realized. These approaches could also be realized in a controllable and low cost manner similarly to the HCG case.

6.4 Summary

Multiwavelength VCSEL arrays are of great interest to the optical communications community because of the need for a low cost WDM source. To date, no product has made it to market because of the lack of a scalable, repeatable manufacturing process. High contrast gratings offer two novel approaches to achieving multiwavelength arrays, both in manners that can potentially be produced at a low cost.

The first approach is to change the phase of the HCG mirror itself by changing the period and duty cycle of the HCG, while leaving the rest of the structure constant. This phase variation of the HCG also changes the emission wavelength of the VCSEL. Thus, the multiwavelength array is produced through a single lithographic step. In simulation, the HCG phase can be adjusted so that the VCSEL cavity itself can be moved over a 200 nm range. Taking into account the overlap factor of the cavity with the active region, a smaller range on the order of 100 nm is expected to be realizable in a practical device.

The second approach is to controllably etch the sacrificial layer underneath the high contrast grating, leaving different depths of air gaps below HCGs in a controllable manner. Doing so creates different optical path lengths in different devices. Other than the different air gap depths, as with the previous approach, the rest of the structure remains the same. This approach was realized experimentally with devices spanning a 53 nm range of wavelengths, all using the same HCG and epitaxial structure. Additionally, this was the first experimental demonstration that an HCG provided greater than 99% reflectivity over a 50 nm range of wavelengths. Multiwavelength VCSEL arrays using HCGs may push the cost of WDM sources to a point where they can be implemented in consumer markets, enabling the next generation of bandwidth-hungry consumer applications.

Chapter 7 Conclusion

Utilizing a high contrast grating (HCG) on a VCSEL can solve several problems that have been holding back VCSEL performance. HCGs can improve the modal properties of VCSELs. For tunable VCSELs, they offer a much lighter mirror, resulting in faster tuning speeds. Additionally, they enable simple, potentially low cost VCSEL structures on InP, an important substrate for achieving VCSELs for mid- and long-distance optical communications applications. Finally, they can be used to create arrays of multiwavelength VCSELs. In this dissertation, we have examined many of these topics in addition to fundamental design and implementation issues of a HCG on a VCSEL.

The HCG presents several interesting questions in its design on a VCSEL. Perhaps the most interesting is the minimum size of the HCG, as the size of the HCG places a minimum on how small the VCSEL itself can be, limiting the reduction of electrical parasitics in the device. We were able to demonstrate through simulation and experiment that the HCG needs to be only as large as the VCSEL's aperture. The smallest experimentally realized HCG was 4 periods, or equivalently just 2.9 μm X 3.0 μm. In addition to size, the tolerance of the HCG to fabrication errors and the spacing between the HCG and VCSEL body were discussed.

For modal properties, the HCG improves performance on two accounts – the first is polarization stability, and the second is higher order mode suppression. Stabilizing a VCSEL along one polarization has been a topic of much research as it is important for many applications for the VCSEL to lase on only a single polarization mode. Since an HCG is subwavelength and birefringent, an HCG can be designed to have a large difference in loss between different polarization modes. We have shown VCSELs with HCG designed to suppress one polarization mode, with polarizer-limited polarization-mode-suppression ratios greater than 20 dB. Polarization-stable HCG VCSELs were discussed and demonstrated at 1310 and 1550 nm. HCGs also have a large effect on the suppression of higher order modes in VCSELs because the HCG's reflection has a much larger angular dependence than a DBR. Through simulation and experiment, this property was discussed and demonstrated.

Tunable VCSELs also see a major improvement when integrated with an HCG. The tuning speed of a tunable VCSEL is limited by the thickness of its movable mirror, so by switching out the typical DBR for a HCG, a huge performance increase in terms of wavelength tuning speed is seen. By making the HCG as small as possible in addition, an order of magnitude increase in tuning speed can be realized. The fastest tunable VCSEL with an HCG reached -3 dB points of approximately 27 MHz in mechanical response, well over an order of magnitude faster than the fastest conventional DBR-based tunable VCSEL [43].

The HCG is also advantageous on InP-based VCSELs. An HCG was integrated on a 1310 nm VCSEL design using a buried tunnel junction. The HCG on this structure consisted of a deposited SiO_2 spacer layer with an amorphous, slightly optically lossy Si HCG layer. The effect of loss in the amorphous Si HCG was studied with this design and found to have only minor effects on the HCG's reflectivity. VCSELs lased continuous wave with output powers up to 0.4 mW under slightly cooled operation. At room temperature, the devices lased pulsed with peak powers up to 4 mW. The performance was not as high as expected due to implementation issues, but these issues could be overcome with some optimization. Nonetheless, HCG VCSELs emitting at 1.32 μm on InP were demonstrated for the first time with good polarization mode suppression.

A new simpler design for InP VCSELs was also implemented, lasing at 1550 nm and enabled by the HCG. Existing commercially available InP VCSEL designs require complicated regrowth to achieve current confinement and a deposited or bonded top mirror. By using proton implantation to form a current aperture, regrowth can be avoided completely. Proton implantation can be used in this structure, only because the top mirror is much thinner, as it is an HCG instead of a thick DBR. Additionally, including an HCG as the top mirror in the epitaxial structure makes any additional bonded or deposited top mirror unnecessary. Using the HCG in combination with a proton-implant-defined aperture, high performance devices were achieved. VCSELs emitting continuous wave at 1.55 μm with output powers of 1.4 mW at room temperature and good polarization stability were demonstrated. The HCG may enable low cost InP-based long wavelength VCSELs.

Arrays of VCSELs emitting at multiple wavelengths are of high interest for next generation high bandwidth links requiring wavelength division multiplexing (WDM). The HCG enables two different concepts for such an array. By changing the HCG's reflection phase by through variation of the HCG's period and bar width, the cavity wavelength can be controllably varied. The cavity wavelength itself can be varied over a range of 200 nm while maintaining high reflectivity of the HCG at the wavelength of interest. Practical design constraints such as the gain bandwidth of the active region and overlap factor between the field in the cavity and the active region will most likely limit the range over which wavelengths can be spaced to approximately 100 nm.

The second approach to multiwavelength HCG arrays is to controllably space the wavelengths in the array by varying the depth of the sacrificial layer etch below the HCG, changing the optical, but not physical, length of the cavity. Using this approach, VCSELs were demonstrated emitting over a wavelength range of approximately 50 nm from the same epitaxial wafer. Additionally, this was the first experimental demonstration that the HCG indeed provided greater than 99% reflectivity over such a broad bandwidth. HCGs provide interesting opportunities for implementing low cost arrays of VCSELs emitting at multiple wavelengths for WDM systems.

In conclusion, VCSELs with integrated high contrast gratings offer many advantages over their DBR-based alternatives. HCG VCSELs may enable the next generation of bandwidth-hungry optical communications applications.

BIBLIOGRAPHY

[1] K. Iga, "Surface-emitting laser-its birth and generation of new optoelectronics field," *Selected Topics in Quantum Electronics, IEEE Journal of*, vol. 6, no. 6, p. 1201–1215, 2000.

[2] H. Kogelnik and C. V. Shank, "Coupled-Wave Theory of Distributed Feedback Lasers," *Journal of Applied Physics*, vol. 43, no. 5, p. 2327–2335, 1972.

[3] H. Soda, K.-ichi Iga, C. Kitahara, and Y. Suematsu, "GaInAsP/InP Surface Emitting Injection Lasers," *Japanese Journal of Applied Physics*, vol. 18, no. 12, pp. 2329-2330, Dec. 1979.

[4] F. Koyama, S. Kinoshita, and K. Iga, "Room-temperature continuous wave lasing characteristics of a GaAs vertical cavity surface-emitting laser," *Applied Physics Letters*, vol. 55, no. 3, p. 221, 1989.

[5] D. L. Huffaker, D. G. Deppe, K. Kumar, and T. J. Rogers, "Native-oxide defined ring contact for low threshold vertical-cavity lasers," *Applied Physics Letters*, vol. 65, no. 1, p. 97–99, 1994.

[6] K. L. Lear, K. D. Choquette, R. P. Schneider, S. P. Kilcoyne, and K. M. Geib, "Selectively oxidised vertical cavity surface emitting lasers with 50% power conversion efficiency," *Electronics Letters*, vol. 31, no. 3, p. 208, 1995.

[7] T. E. Sale et al., "Manufacturability of 850nm data communication VCSELs in high volume," presented at the Vertical-Cavity Surface-Emitting Lasers XIV, San Francisco, California, USA, 2010, pp. 761503-761503-10.

[8] C. J. Helms, "Reliability of oxide VCSELs at Emcore," in *Proceedings of SPIE*, San Jose, CA, USA, 2004, pp. 183-189.

[9] B. M. Hawkins, R. A. Hawthorne III, J. K. Guenter, J. A. Tatum, and J. R. Biard, "Reliability of various size oxide aperture VCSELs," in *Electronic Components and Technology Conference, 2002. Proceedings. 52nd*, 2002, p. 540–550.

[10] J. L. Jewell, J. P. Harbison, A. Scherer, Y. H. Lee, and L. T. Florez, "Vertical-cavity surface-emitting lasers: design, growth, fabrication, characterization," *Quantum Electronics, IEEE Journal of*, vol. 27, no. 6, p. 1332–1346, 1991.

[11] M. Ortsiefer, R. Shau, G. Böhm, F. Köhler, G. Abstreiter, and M.-C. Amann, "Low-resistance InGa(Al)As Tunnel Junctions for Long Wavelength Vertical-cavity Surface-emitting Lasers," *Japanese Journal of Applied Physics*, vol. 39, no. Part 1, No. 4A, pp. 1727-1729, 2000.

[12] K. D. Choquette, R. P. Schneider, M. Hagerott Crawford, K. M. Geib, and J. J. Figiel, "Continuous wave operation of 640–660 nm selectively oxidised AlGaInP vertical-cavity lasers," *Electronics Letters*, vol. 31, no. 14, p. 1145, 1995.

[13] E. Soderberg et al., "High-Temperature Dynamics, High-Speed Modulation, and Transmission Experiments Using 1.3- μm InGaAs Single-Mode VCSELs," *Journal of Lightwave Technology*, vol. 25, no. 9, pp. 2791-2798, Sep. 2007.

[14] A. Ramakrishnan, G. Steinle, D. Supper, C. Degen, and G. Ebbinghaus, "Electrically pumped 10 Gbit/s MOVPE-grown monolithic 1.3 μm VCSEL with GaInNAs active region," *Electronics Letters*, vol. 38, no. 7, pp. 322-324, 2002.

[15] T. Sarmiento, H. P. Bae, T. D. O'Sullivan, and J. S. Harris, "GaAs-based 1.53 μm GaInNAsSb vertical cavity surface emitting lasers," *Electronics Letters*, vol. 45, no. 19, pp. 978-979, 2009.

[16] S. R. Bank, H. P. Bae, H. B. Yuen, M. A. Wistey, L. L. Goddard, and J. S. Harris, "Room-temperature continuous-wave 1.55 μm GaInNAsSb laser on GaAs," *Electronics Letters*, vol. 42, no. 3, p. 156, 2006.

[17] C. E. Zah et al., "High-performance uncooled 1.3-μm AlxGayIn1-x-yAs/InP strained-layer quantum-well lasers for subscriber loop applications," *Quantum Electronics, IEEE Journal of*, vol. 30, no. 2, p. 511–523, 1994.

[18] M. Ortsiefer, R. Shau, G. Böhm, F. Köhler, and M. C. Amann, "Low-threshold index-guided 1.5 μm long-wavelength vertical-cavity surface-emitting laser with high efficiency," *Applied Physics Letters*, vol. 76, p. 2179, 2000.

[19] J. Boucart et al., "1-mW CW-RT monolithic VCSEL at 1.55 μm," *IEEE Photonics Technology Letters*, vol. 11, no. 6, pp. 629-631, Jun. 1999.

[20] M. Muller, W. Hofmann, G. Bohm, and M.-C. Amann, "Short-Cavity Long-Wavelength VCSELs With Modulation Bandwidths in Excess of 15 GHz," *IEEE Photonics Technology Letters*, vol. 21, no. 21, pp. 1615-1617, Nov. 2009.

[21] M.-C. Amann and W. Hofmann, "InP-Based Long-Wavelength VCSELs and VCSEL Arrays," *Selected Topics in Quantum Electronics, IEEE Journal of*, vol. 15, no. 3, pp. 861-868, 2009.

[22] M. Ortsiefer et al., "2.5-mW single-mode operation of 1.55-μm buried tunnel junction VCSELs," *IEEE Photonics Technology Letters*, vol. 17, no. 8, pp. 1596-1598, Aug. 2005.

[23] W. Yuen et al., "High-performance 1.6 μm single-epitaxy top-emitting VCSEL," *Electronics Letters*, vol. 36, no. 13, p. 1121–1123, 2000.

[24] S. Nakagawa et al., "88°C, continuous-wave operation of apertured, intracavity contacted, 1.55 μm vertical-cavity surface-emitting lasers," *Applied Physics Letters*, vol. 78, no. 10, p. 1337, 2001.

[25] A. Syrbu et al., "1550 nm-band VCSEL 0.76 mW singlemode output power in 20–80°C temperature range," *Electronics Letters*, vol. 40, no. 5, p. 306, 2004.

[26] N. Nishiyama et al., "Long-Wavelength Vertical-Cavity Surface-Emitting Lasers on InP With Lattice Matched AlGaInAs-InP DBR Grown by MOCVD," *IEEE Journal of Selected Topics in Quantum Electronics*, vol. 11, no. 5, pp. 990-998, Sep. 2005.

[27] A. Syrbu et al., "1.5-mW Single-Mode Operation of Wafer-Fused 1550-nm VCSELs," *IEEE Photonics Technology Letters*, vol. 16, no. 5, pp. 1230-1232, May. 2004.

[28] C. Chase, Y. Rao, W. Hofmann, and C. J. Chang-Hasnain, "1550 nm high contrast grating VCSEL," *Optics Express*, vol. 18, no. 15, p. 15461, Jul. 2010.

[29] T.-C. Lu, C.-C. Kao, H.-C. Kuo, G.-S. Huang, and S.-C. Wang, "CW lasing of current injection blue GaN-based vertical cavity surface emitting laser," *Applied Physics Letters*, vol. 92, no. 14, p. 141102, 2008.

[30] R. Chen, H. D. Sun, T. Wang, K. N. Hui, and H. W. Choi, "Optically pumped ultraviolet lasing from nitride nanopillars at room temperature," *Applied Physics Letters*, vol. 96, no. 24, p. 241101, 2010.

[31] S. Kalusniak, S. Sadofev, S. Halm, and F. Henneberger, "Vertical cavity surface emitting laser action of an all monolithic ZnO-based microcavity," *Applied Physics Letters*, vol. 98, p. 011101, 2011.

[32] M. Ortsiefer et al., "Electrically pumped room temperature CW VCSELs with 2.3 μm emission wavelength," *Electronics Letters*, vol. 42, no. 11, p. 640, 2006.

[33] A. Bachmann, T. Lim, K. Kashani-Shirazi, O. Dier, C. Lauer, and M.-C. Amann, "Continuous-wave operation of electrically pumped GaSb-based vertical cavity surface emitting laser at 2.3 μm," *Electronics Letters*, vol. 44, no. 3, p. 202, 2008.

[34] S. Arafin, A. Bachmann, K. Kashani-Shirazi, and M.-C. Amann, "Electrically pumped continuous-wave vertical-cavity surface-emitting lasers at ~2.6 μm," *Applied Physics Letters*, vol. 95, no. 13, p. 131120, 2009.

[35] A. Ducanchez, L. Cerutti, P. Grech, F. Genty, and E. Tournié, "Mid-infrared GaSb-based EP-VCSEL emitting at 2.63 [micro sign]m," *Electronics Letters*, vol. 45, no. 5, p. 265, 2009.

[36] M. S. Wu, E. C. Vail, G. S. Li, W. Yuen, and C. J. Chang-Hasnain, "Tunable micromachined vertical cavity surface emitting laser," *Electronics Letters*, vol. 31, no. 19, p. 1671–1672, 1995.

[37] M. C. Larson, A. R. Massengale, and J. J. S. Harris, "Continuously tunable micromachined vertical cavity surface emitting laser with 18 nm wavelength range," *Electronics Letters*, vol. 32, no. 4, pp. 330-332, 1996.

[38] C. J. Chang-Hasnain, "Tunable VCSEL," *IEEE J. Select. Topics Quantum Electron*, vol. 6, no. 6, p. 978–987, 2000.

[39] M. Lackner et al., "CO and CO2 spectroscopy using a 60 nm broadband tunable MEMS-VCSEL at 1.55 μm," *Optics Letters*, vol. 31, no. 21, p. 3170–3172, 2006.

[40] B. Mason, G. A. Fish, S. P. DenBaars, and L. A. Coldren, "Widely tunable sampled grating DBR laser with integrated electroabsorption modulator," *Photonics Technology Letters, IEEE*, vol. 11, no. 6, p. 638–640, 1999.

[41] K. C. Harvey and C. J. Myatt, "External-cavity diode laser using a grazing-incidence diffraction grating," *Optics Letters*, vol. 16, no. 12, p. 910–912, 1991.

[42] P. Tayebati et al., "Half-symmetric cavity tunable microelectromechanical VCSEL withsingle spatial mode," *IEEE Photonics Technology Letters*, vol. 10, no. 12, p. 1679–1681, 1998.

[43] G. D. Cole, E. Behymer, T. C. Bond, and L. L. Goddard, "Short-wavelength MEMS-tunable VCSELs," *Optics Express*, vol. 16, no. 20, p. 16093–16103, 2008.

[44] F. Riemenschneider, M. Maute, H. Halbritter, G. Boehm, M.-C. Amann, and P. Meissner, "Continuously Tunable Long-Wavelength MEMS-VCSEL With Over 40-nm Tuning Range," *IEEE Photonics Technology Letters*, vol. 16, no. 10, pp. 2212-2214, Oct. 2004.

[45] M. C. Y. Huang, K. B. Cheng, Y. Zhou, B. Pesala, C. J. Chang-Hasnain, and A. P. Pisano, "Demonstration of piezoelectric actuated GaAs-based MEMS tunable VCSEL," *IEEE Photonics Technology Letters*, vol. 18, no. 10, pp. 1197-1199, May. 2006.

[46] Y. M. Li, W. Yuen, G. S. Li, and C. J. Chang-Hasnain, "Top-emitting micromechanical VCSEL with a 31. 6-nm tuning range," *IEEE Photonics Technology Letters*, vol. 10, no. 1, p. 18–20, 1998.

[47] M. Maute, B. Kogel, G. Bohm, P. Meissner, and M.-C. Amann, "MEMS-tunable 1.55-μm VCSEL with extended tuning range incorporating a buried tunnel junction," *IEEE Photonics Technology Letters*, vol. 18, no. 5, pp. 688-690, Mar. 2006.

[48] C. Gierl et al., "Tuneable VCSEL aiming for the application in interconnects and short haul systems," presented at the Optical Metro Networks and Short-Haul Systems III, San Francisco, California, USA, 2011, pp. 795908-795908-13.

[49] C. K. Chan, K. L. Sherman, and M. Zirngibl, "A fast 100-channel wavelength-tunable transmitter for optical packet switching," *Photonics Technology Letters, IEEE*, vol. 13, no. 7, p. 729–731, 2002.

[50] D. Sun et al., "Long Wavelength-Tunable VCSELs With Optimized MEMS Bridge Tuning Structure," *IEEE Photonics Technology Letters*, vol. 16, no. 3, pp. 714-716, Mar. 2004.

[51] J. Boucart et al., "Long wavelength MEMS tunable VCSEL with InP-InAlGaAs bottom DBR," *IEEE Photonics Technology Letters*, vol. 15, no. 9, pp. 1186-1188, Sep. 2003.

[52] M. C. Y. Huang, Y. Zhou, and C. J. Chang-Hasnain, "A nanoelectromechanical tunable laser," *Nature Photonics*, vol. 2, no. 3, pp. 180-184, Mar. 2008.

[53] C. Chase, Y. Zhou, and C. J. Chang-Hasnain, "Size effect of high contrast gratings in VCSELs," *Opt. Express*, vol. 17, p. 24002–24007, 2009.

[54] T. Schrans et al., "100Gb/s 10km link performance of 10 x 10Gb/s hybrid approach with integrated WDM array of DFB lasers," in *Optical Fiber Communication-incudes post deadline papers, 2009. OFC 2009. Conference on*, 2009, p. 1–3.

[55] C. J. Chang-Hasnain, M. W. Maeda, N. G. Stoffel, J. P. Harbison, L. T. Florez, and J. Jewell, "Surface emitting laser arrays with uniformly separated wavelengths," *Electronics Letters*, vol. 26, no. 13, p. 940, 1990.

[56] C. J. Chang-Hasnain et al., "Multiple wavelength tunable surface-emitting laser arrays," *IEEE Journal of Quantum Electronics*, vol. 27, no. 6, pp. 1368-1376, Jun. 1991.

[57] L. E. Eng, K. Bacher, W. Yuen, J. S. Harris, and C. J. Chang-Hasnain, "Multiple-wavelength vertical cavity laser arrays on patterned substrates," *IEEE Journal of Selected Topics in Quantum Electronics*, vol. 1, no. 2, pp. 624-628, Jun. 1995.

[58] F. Koyama, T. Mukaihara, Y. Hayashi, N. Ohnoki, N. Hatori, and K. Iga, "Wavelength control of vertical cavity surface-emitting lasers by using nonplanar MOCVD," *IEEE Photonics Technology Letters*, vol. 7, no. 1, pp. 10-12, Jan. 1995.

[59] T. Wipiejewski, J. Ko, B. J. Thibeault, and L. A. Coldren, "Multiple wavelength vertical-cavity laser array employing molecular beam epitaxy regrowth," *Electronics Letters*, vol. 32, no. 4, pp. 340-342, 1996.

[60] K. D. Choquette, D. A. Richie, and R. E. Leibenguth, "Temperature dependence of gain-guided vertical-cavity surface emitting laser polarization," *Applied Physics Letters*, vol. 64, no. 16, p. 2062, 1994.

[61] D. V. Kuksenkov, H. Temkin, and S. Swirhun, "Polarization instability and relative intensity noise in vertical-cavity surface-emitting lasers," *Applied Physics Letters*, vol. 67, no. 15, p. 2141, 1995.

[62] S. J. Schablitsky, L. Zhuang, R. C. Shi, and S. Y. Chou, "Controlling polarization of vertical-cavity surface-emitting lasers using amorphous silicon subwavelength transmission gratings," *Applied Physics Letters*, vol. 69, p. 7, 1996.

[63] P. Debernardi, J. M. Ostermann, M. Feneberg, C. Jalics, and R. Michalzik, "Reliable polarization control of VCSELs through monolithically integrated surface gratings: a comparative theoretical and experimental study," *IEEE Journal of Selected Topics in Quantum Electronics*, vol. 11, no. 1, pp. 107-116, Jan. 2005.

[64] P. Babu Dayal, N. Kitabayashi, T. Miyamoto, F. Koyama, T. Kawashima, and S. Kawakami, "Polarization control of 1.15 μm vertical-cavity surface-emitting lasers using autocloned photonic crystal polarizer," *Applied Physics Letters*, vol. 91, no. 4, p. 041110, 2007.

[65] A. Haglund, J. S. Gustavsson, J. Bengtsson, P. Jedrasik, and A. Larsson, "Design and Evaluation of Fundamental-Mode and Polarization-Stabilized VCSELs With a Subwavelength Surface Grating," *IEEE Journal of Quantum Electronics*, vol. 42, no. 3, pp. 231-240, Mar. 2006.

[66] M. Ortsiefer et al., "Polarization Control in Buried Tunnel Junction VCSELs Using a Birefringent Semiconductor/Dielectric Subwavelength Grating," *IEEE Photonics Technology Letters*, vol. 22, no. 1, pp. 15-17, Jan. 2010.

[67] C. J. Chang-Hasnain et al., "Dynamic, polarization, and transverse mode characteristics ofvertical cavity surface emitting lasers," *IEEE Journal of Quantum Electronics*, vol. 27, no. 6, p. 1402–1409, 1991.

[68] D.-S. Song, S.-H. Kim, H.-G. Park, C.-K. Kim, and Y.-H. Lee, "Single-fundamental-mode photonic-crystal vertical-cavity surface-emitting lasers," *Applied Physics Letters*, vol. 80, no. 21, p. 3901, 2002.

[69] N. Yokouchi, A. J. Danner, and K. D. Choquette, "Two-dimensional photonic crystal confined vertical-cavity surface-emitting lasers," *IEEE Journal of Selected Topics in Quantum Electronics*, vol. 9, no. 5, pp. 1439-1445, Sep. 2003.

[70] A. Haglund, J. S. Gustavsson, J. Vukusic, P. Modh, and A. Larsson, "Single Fundamental-Mode Output Power Exceeding 6 mW From VCSELs With a Shallow Surface Relief," *IEEE Photonics Technology Letters*, vol. 16, no. 2, pp. 368-370, Feb. 2004.

[71] M. C. Y. Huang, Y. Zhou, and C. J. Chang-Hasnain, "Single mode high-contrast subwavelength grating vertical cavity surface emitting lasers," *Applied Physics Letters*, vol. 92, no. 17, p. 171108, 2008.

[72] C. Chase, Y. Zhou, and C. J. Chang-Hasnain, "Impact of high contrast grating size in tunable VCSELs," in *Lasers and Electro-Optics, 2009 and 2009 Conference on Quantum electronics and Laser Science Conference. CLEO/QELS 2009. Conference on*, 2009, p. 1–2.

[73] C. F. R. Mateus, M. C. Y. Huang, Y. Deng, A. R. Neureuther, and C. J. Chang-Hasnain, "Ultrabroadband Mirror Using Low-Index Cladded Subwavelength Grating," *IEEE Photonics Technology Letters*, vol. 16, no. 2, pp. 518-520, Feb. 2004.

[74] Y. Ding and R. Magnusson, "Resonant leaky-mode spectral-band engineering and device applications," *Optics Express*, vol. 12, no. 23, p. 5661–5674, 2004.

[75] C. F. R. Mateus, M. C. Y. Huang, L. Chen, C. J. Chang-Hasnain, and Y. Suzuki, "Broad-Band Mirror (1.12-1.62 μm) Using a Subwavelength Grating," *IEEE Photonics Technology Letters*, vol. 16, no. 7, pp. 1676-1678, Jul. 2004.

[76] M. C. Y. Huang, Y. Zhou, and C. J. Chang-Hasnain, "Nano electro-mechanical optoelectronic tunable VCSEL," *Optics Express*, vol. 15, no. 3, p. 1222–1227, 2007.

[77] M. C. Y. Huang, Y. Zhou, and C. J. Chang-Hasnain, "A surface-emitting laser incorporating a high-index-contrast subwavelength grating," *Nature Photonics*, vol. 1, no. 2, pp. 119-122, Feb. 2007.

[78] Y. Zhou, V. Karagodsky, B. Pesala, F. G. Sedgwick, and C. J. Chang-Hasnain, "A novel ultra-low loss hollow-core waveguide using subwavelength high-contrast gratings," *Optics Express*, vol. 17, no. 3, p. 1508–1517, 2009.

[79] Y. Zhou, M. Moewe, J. Kern, M. C. Huang, and C. J. Chang-Hasnain, "Surface-normal emission of a high-Q resonator using a subwavelength high-contrast grating," *Optics Express*, vol. 16, no. 22, p. 17282–17287, 2008.

[80] B. E. N. Keeler, D. W. Carr, J. P. Sullivan, T. A. Friedmann, and J. R. Wendt, "Experimental demonstration of a laterally deformable optical nanoelectromechanical system grating transducer," *Optics letters*, vol. 29, no. 11, p. 1182–1184, 2004.

[81] T. Stöferle et al., "Ultracompact Silicon/Polymer Laser with an Absorption-Insensitive Nanophotonic Resonator," *Nano Letters*, p. 1819–1821, 2010.

[82] F. Lu, F. G. Sedgwick, V. Karagodsky, C. Chase, and C. J. Chang-Hasnain, "Planar high-numerical-aperture low-loss focusing reflectors and lenses using subwavelength high contrast gratings," *Optics Express*, vol. 18, no. 12, pp. 12606-12614, 7. 2010.

[83] D. Fattal, J. Li, Z. Peng, M. Fiorentino, and R. G. Beausoleil, "Flat dielectric grating reflectors with focusing abilities," *Nature Photonics*, vol. 4, no. 7, pp. 466-470, May. 2010.

[84] V. Karagodsky, B. Pesala, C. Chase, W. Hofmann, F. Koyama, and C. J. Chang-Hasnain, "Monolithically integrated multi-wavelength VCSEL arrays using high-contrast gratings," *Opt. Express*, vol. 18, p. 694–699, 2010.

[85] J. M. Ostermann, P. Debernardi, and R. Michalzik, "Optimized integrated surface grating design for polarization-stable VCSELs," *Quantum Electronics, IEEE Journal of*, vol. 42, no. 7, pp. 690-698, 2006.

[86] Y. Zhou et al., "High-Index-Contrast Grating (HCG) and Its Applications in Optoelectronic Devices," *IEEE Journal of Selected Topics in Quantum Electronics*, vol. 15, no. 5, pp. 1485-1499, 2009.

[87] P. Gilet et al., "High-index-contrast subwavelength grating VCSEL," in *Vertical-Cavity Surface-Emitting Lasers XIV*, 2010, vol. 7615, p. 76150J.

[88] W. Hofmann et al., "Long-Wavelength High-Contrast Grating Vertical-Cavity Surface-Emitting Laser," *IEEE Photonics Journal*, vol. 2, no. 3, pp. 415-422, Jun. 2010.

[89] V. Karagodsky, F. G. Sedgwick, and C. J. Chang-Hasnain, "Theoretical analysis of subwavelength high contrast grating reflectors," *Optics Express*, vol. 18, no. 16, pp. 16973-16988, 2010.

[90] R. Magnusson and M. Shokooh-Saremi, "Physical basis for wideband resonant reflectors," *Optics Express*, vol. 16, no. 5, p. 3456–3462, 2008.

[91] A. Ahmed, M. Liscidini, and R. Gordon, "Design and Analysis of High-Index-Contrast Gratings Using Coupled Mode Theory," *Photonics Journal, IEEE*, vol. 2, no. 6, p. 884–893, 2010.

[92] M. G. Moharam and T. K. Gaylord, "Rigorous coupled-wave analysis of planar-grating diffraction," *J. Opt. Soc. Am.*, vol. 71, no. 7, p. 811–818, 1981.

[93] Y. Zhou, M. C. Y. Huang, and C. J. Chang-Hasnain, "Large Fabrication Tolerance for VCSELs Using High-Contrast Grating," *IEEE Photonics Technology Letters*, vol. 20, no. 6, pp. 434-436, Mar. 2008.

[94] T. H. P. Chang, "Proximity effect in electron‐beam lithography," *Journal of Vacuum Science and Technology*, 1975. .

[95] S. Boutami, B. Benbakir, J.-L. Leclercq, and P. Viktorovitch, "Compact and polarization controlled 1.55 μm vertical-cavity surface-emitting laser using single-layer photonic crystal mirror," *Applied Physics Letters*, vol. 91, no. 7, p. 071105, 2007.

[96] Y. Zhou, M. C. Huang, and C. J. Chang-Hasnain, "Tunable VCSEL with ultra-thin high contrast grating for high-speed tuning," *Optics Express*, vol. 16, no. 18, p. 14221–14226, 2008.

[97] S. Senturia, *Microsystem design*. Boston: Kluwer Academic Publishers, 2001.

[98] L. Coldren and S. Corzine, *Diode Lasers and Photonic Integrated Circuits*. New York: Wiley, 1995.

[99] J. P. Kim and A. M. Sarangan, "Temperature-dependent Sellmeier equation for the refractive index of $Al_x Ga_{1-x} As$," *Optics Letters*, vol. 32, no. 5, p. 536, 2007.

[100] C. Chang-Hasnain, Y. Zhou, M. Huang, and C. Chase, "High-Contrast Grating VCSELs," *IEEE J. Sel. Top. Quantum Electron*, vol. 15, p. 869–878, 2009.

[101] G. Agrawal, *Fiber-Optic Communication Systems*, 3rd ed. John Wiley & Sons, Inc., 2002.

[102] M. C. Larson et al., "GaInNAs-GaAs long-wavelength vertical-cavity surface-emitting laser diodes," *Photonics Technology Letters, IEEE*, vol. 10, no. 2, pp. 188-190, 1998.

[103] A. Mereuta, G. Suruceanu, A. Caliman, V. Iacovlev, A. Sirbu, and E. Kapon, "10-Gb/s and 10-km error-free transmission up to 100° C with 1.3-μm wavelength wafer-fused VCSELs," *Optics Express*, vol. 17, no. 15, p. 12981–12986, 2009.

[104] W. Hofmann et al., “22-Gb/s Long Wavelength VCSELs,” *Optics Express*, vol. 17, no. 20, p. 17547–17554, 2009.

[105] K. Tai, R. J. Fischer, K. W. Wang, S. N. G. Chu, and A. Y. Cho, “Use of implant isolation for fabrication of vertical cavity surface-emitting laser diodes,” *Electronics Letters*, vol. 25, no. 24, pp. 1644-1645, 1989.

[106] J. K. Guenter, R. A. Hawthorne III, D. Granville, M. Hibbs-Brenner, and R. Morgan, “Reliability of proton-implanted VCSELs for data communications,” in *Proceedings of SPIE*, San Jose, CA, USA, 1996, pp. 102-113.

[107] Y. Rao, C. Chase, and C. J. Chang-Hasnain, “Multiwavelength HCG-VCSEL array,” in *22nd IEEE International Semiconductor Laser Conference*, Kyoto, Japan, 2010, pp. 11-12.